ADVANCED SYNTHESIS OF ULTRA-HIGH TEMPERATURE CERAMICS (UHTCs) AND HIGH TEMPERATURE ELECTRON EMITTING MATERIALS

by

Santanu Mondal

Dissertation submitted to the faculty of the Virginia Polytechnic Institute and State University in partial fulfillment of the requirements for the degree of

Doctor of Philosophy

In

Materials Science and Engineering

Dwight D. Viehland, Chair

Jiefang Li

Guo-Quan Lu

Alex O. Aning

December 5th, 2023
Blacksburg, Virginia

Keywords: bulk ceramic processing, thin films, reaction synthesis, ultra-fast high temperature sintering, work function engineering, electron transpiration cooling, crystal structure and microstructural analysis, oxidation and mechanical property, and Kelvin probe force microscopy.

ADVANCED SYNTHESIS OF ULTRA-HIGH TEMPERATURE CERAMICS (UHTCs) AND HIGH TEMPERATURE ELECTRON EMITTING MATERIALS

Santanu Mondal

Technical Abstract

From space exploration and advanced aircraft to next generation weapons, achieving hypersonic speed is becoming increasingly important across a range of research domains. The immense challenge associated with this goal involves the development of suitable materials and systems for the different components of a hypersonic vehicle, each of which must have the inherent capability to resist extreme temperatures, high thermal shock due to high heat flux, and high oxidation and ablation.

First, the ultra-high temperature ceramic (UHTC) zirconium diboride or ZrB_2 was sintered by ultra-fast high temperature sintering (UHS). The UHS process was optimized and the sintering parameters for ZrB_2 and other UHTCs were studied. ZrB_2 is an ultra-high temperature ceramic (UHTC) with a very high melting point; thus, its densification is difficult, energy intensive, and time-consuming. Commercial ZrB_2 powders were rapidly densified via UHS to >90% relative density within 60 second in vacuum without pressure. The effect of sintering time on densification and final grain size were studied. An innovative process for manufacturing bulk UHTC materials was studied and is detailed herein.

Second, the work function (W_f) of electron emitting materials was reduced to improved performance. A reduction of W_f in multicomponent hexaborides was achieved by doping with highly electropositive Ba, which enhances electron emission. Single-phase bulk multicomponent

polycrystalline hexaborides of $La_{0.5}Ba_{0.5}B_6$, $Ce_{0.5}Ba_{0.5}B_6$, and BaB_6 powders were first synthesized and then densified by UHS sintering. W_f measurements were obtained by Kelvin probe force microscopy. Ba-substitution was found to lower W_f (~25%) in synthesized multicomponent hexaborides. The specific techniques required to engineer the W_f of these materials are also provided herein.

Finally, combining low W_f materials with UHTCs was explored for thin film systems for the exterior surface of hypersonic vehicles. The thin films of CeB_6, a low W_f material, was deposited on sintered ZrB_2 by RF-sputtering and single crystalline $SrTiO_3$ (STO) substrates. Epitaxial thin films of $SrHfO_3$ (SHO) were also deposited on (100), (110) and (111) STO substrates at 600°C. X-ray diffraction (XRD) results confirmed the formation of epitaxial layer, and reciprocal space mapping (RSM) was used to characterize film's mosaicity / texture on different substrates. XRD and RSM data demonstrated that the most favorable film growth direction was (110). As detailed herein, an inexpensive thin film production process, RF-sputtering, was exploited to manufacture various epitaxial and non-epitaxial layers of low W_f materials on UHTC and single-crystal substrates for hypersonic vehicles.

To summarize, a range of bulk UHTCs and low W_f materials were prepared by UHS, and various thin films of low W_f material were produced on UHTC. Thereafter, the properties of synthesized materials were studied to develop new material systems for hypersonic applications. The findings from this research shed light on the development of suitable materials for implementation of electron transpiration cooling for hypersonic vehicle development.

ADVANCED SYNTHESIS OF ULTRA-HIGH TEMPERATURE CERAMICS (UHTCs) AND HIGH TEMPERATURE ELECTRON EMITTING MATERIALS

Santanu Mondal

General Audience Abstract

Rapid sintering of ultra-high temperature ceramics (UHTCs) and synthesis of low work-function electron emitting materials have been performed by ultra-fast high temperature sintering technique (UHS). Sintering of UHTCs is a difficult process, due to their high melting temperature, presence of covalent bond, and slower diffusion coefficient. A long sintering duration is used to achieve a high relative density along with adding sintering aid, using fine powder (produced by milling), and utilizing pressure (such as field assisted sintering and hot-pressing technology) during sintering. Synthesis and densification of multicomponent hexaboride is difficult, involves multi-steps and complicated processes. These long and complicated processes not only prolong development of new materials but also cause chemical wastes. To overcome all the aforementioned processing issues, an advanced processing technique, UHS, is used and densified pure and commercially available UHTCs to >90% within 60 second without applying sintering aid, powder milling, and pressure. The outcome of this research demonstrates the potential for a simple, cost-effective, fast, and adjustable processes, UHS, to develop a wide range of bulk UHTCs and other technical ceramics, and it gives new insight into the mechanisms of rapid sintering of UHTCs by rapid heating.

The first detailed studies (experimental report) on rapid sintering of ZrB_2 (and other UHTCs) by UHS technique and a through characterizations of the UHS sintered sample were performed to understand rapid sintering mechanism and how the processing effects the microstructure and properties of UHS ZrB_2. The rapid microstructural evolution during the UHS sintering is investigated at 10, 30, and 60 second sintering interval. The UHS technique enables a heating rate of 10^3 - 10^4 °C/min and reaches a sintering

temperature of 2600 °C in 30 seconds. Microstructural analysis was conducted on polished sample surfaces by using ImageJ software (National Institutes of Health, version 1.53e), measuring the grain size perpendicular to two diagonals of each grain. A comparison of grain size from sample center and periphery showed a homogeneous microstructure after sintering. Furthermore, the rapid sintering did not change/effect crystallinity, boron to metal stoichiometry, and grain boundary elemental composition as observed by XRD and EDS analysis. Additional characterization of the UHS sintered ZrB_2 shows a hardness and elastic modulus of 30 GPa and 412 GPa respectively by nanoindentation method. Finally, the oxidation test at 1100 °C in isothermal condition showed a weight gain of 1.4% in air.

The low work-function (W_f) materials are famous for electron emitting applications like electron guns for scanning electron microscopy. DFT simulation predicts the W_f of the widely used electron emitters (such as LaB_6 and CeB_6) can be reduced by changing their compositions, which increase electron generation efficiency of those materials. Previously, those materials were synthesized by long processes that involved multiple processing steps, which required expensive starting materials and yielded chemical wastes. The advantages of rapid sintering technique, UHS, had been exploited to synthesize low work function electron emitting materials. Single-phase bulk polycrystalline hexaborides were produced by using electrically powered UHS technique using a vacuum atmosphere. A reaction synthesis route: B_4C reduction technique was first used to form pure phase hexaboride. Then, the synthesized compositions were densified to ~90% theoretical density in 180 seconds by UHS densification. After UHS sintering, XRD analysis confirmed the presence of a phase pure cubic BaB_6, $La_{0.5}Ba_{0.5}B_6$, and $Ce_{0.5}Ba_{0.5}B_6$. Additional analyses were conducted to determine an optimum reaction temperature 1500 and 2100 °C for the formation BaB_6 and multi-component hexaborides. Microstructural analyses were conducted to observe both reaction-synthesized and densified products. EDS compositional analysis and elemental mapping revealed a stoichiometric reaction product with homogeneous metal cation and boron distributions. The W_f of BaB_6, $La_{0.5}Ba_{0.5}B_6$, and $Ce_{0.5}Ba_{0.5}B_6$ was determined to be 1.95 ± 0.1, 2.05 ± 0.1 and 2.0 ± 0.1 eV, respectively. The addition of BaB_6 in $La_{0.5}Ba_{0.5}B_6$, and $Ce_{0.5}Ba_{0.5}B_6$ resulted in a 25% decrease in W_f for LaB_6 from 2.7 ± 0.1 to 2.00 ± 0.1 eV

and a 23% decrease in W_f for CeB_6 from 2.68 ± 0.08 to 2.05 ± 0.1 eV. Ba substitution is shown to be a general method for lowering W_f in a variety of multicomponent hexaborides.

Finally, the polycrystalline thin films of CeB_6, a low W_f material, was deposited on sintered ZrB_2 by RF-sputtering technique. Additionally, epitaxial thin films of $SrHfO_3$ (SHO) were also deposited on (100), (110) and (111) STO single crystalline substrates. Both types of thin films were deposited at 600 °C temperature and at a vacuum pressure of 10^{-3} Torr. After deposition of the SHO films, X-ray diffraction (XRD) was conducted to confirm the formation of epitaxial layer, and reciprocal space mapping (RSM) was used to characterize film's mosaicity / texture on different substrates. XRD and RSM data demonstrated that the most favorable film growth direction was (110). The XRD of the CeB_6 film showed highly crystalline film was formed. For both the films, a detailed microstructural analysis was performed by scanning electron microscopy and film smoothness was characterized by atomic force microscopy method. As detailed herein, an inexpensive thin film production process, RF-sputtering, was exploited to manufacture various epitaxial and non-epitaxial layers of low W_f materials on UHTC and single-crystal substrates for hypersonic vehicles applications.

ACKNOWLEDGEMENTS

First, I am incredibly grateful to my professor, Dr. Dwight D. Viehland. Without his forbearance and persistent support, I would not be writing this dissertation. I have always been enormously motivated by his expertise, and enthusiasm for research during my tenure as his PhD student. His word, "I want you to grow," served as ongoing inspiration during my time at Virginia Tech. His unceasingly support and encouragement through handwritten corrections of my manuscript and other documents, regular research discussions, and insightful feedback on my presentations substantially helped in my progress. My gratitude for his enormous assistance in transforming me into a self-assured scientist is truly immeasurable.

Furthermore, I would like to profoundly thank to Professor Jiefang Li for her innumerable support and incisive advice. When I was having problems in the lab, she was the first person to offer guidance. I could never have accomplished my research goals without her extensive competence with different experimental approaches.

I would like to thank Dr. Alex O. Aning and Dr. Guo-Quan Lu for serving as my committee members, and for their conducive feedback on all aspects of my work. I would like to thank Drs. Kathy Lu and Dr. Carolina Tallon for their assistance with measurements and Dr. William Reynold's valuable for their insightful counsel on various circumstances.

I would like to acknowledge kind help and support from all the faculty and staff in the MSE department for. Specifically, I would like to thank to Mrs. Kim Grandstaff, Mrs. Cindy Perdue, Mrs. Amy Hill, and Mrs. Susan Fleming-Cook at MSE Department for always helping me with different situations during my time at Virginia Tech.

I also extend my thanks to my fellow students at Virginia Tech: Shuvodip Bhattacharya, Advaith Rau, Donnie Erb, and Jonathan Charleston, for their shared skills and valuable remarks on my research.

For assistance with numerous measurements, I must acknowledge the contributions of Dr. Rituraj Borgohain and Mr. Patrick Finley at the Institute for Critical Technology and Applied Science (ICTAS) at VT, Dr. Carlos Suchicital, Dr. Tom Staley, and Dr. Hesham Elmkharram (MSE, Virginia Tech) at MSE Department lab, and Mr. Stephen McCartney at the Nanoscale Characterization and Fabrication Laboratory (NCFL) for his support. His extraordinary expertise with the SEM is remarkable.

Finally, I would like to express my earnest appreciation to my parents, Jhumni Mondal and Satyajit Mondal, my wife, Riya Ghosh, and my best friend, Somnath Mandal, for their constant trust and encouragement. I will be endlessly indebted for their unreserved love and care.

I would also like to reproduce the Acknowledgement statement from my published papers.

"I acknowledge support from the Army Research Office (Grant Number W911NF-20-1-0012). The U.S. Government is authorized to reproduce and distribute reprints for Government purposes notwithstanding any copyright notation herein. The views and conclusions contained in this document are those of the authors and should not be interpreted as representing the official policies, either expressed or implied, of the Army Research Office or the U.S. Government."

TABLE OF CONTENTS

List of Tables

List of Figures

CHAPTER i: INTRODUCTION

The need for new materials for high-temperature structural and functional applications is increasing. These high-temperature structural materials are commonly referred to as ultra-high temperature ceramics (UHTCs). UHTCs include a wide range of boride and carbide materials that can tolerate extreme operational conditions, including those that would be required in aerothermal applications—for instance in the nose cones of hypersonic vehicles. As such, more efficient methods for fabricating these materials to higher densities could be important. The highest melting point of UHTC materials is still limited to temperatures somewhat above 3000 °C, which is extremely high, but not sufficiently robust to meet the demanding needs of hypersonic applications.

Numerous efforts have been undertaken recently to advance transpiration cooling as a strategy for enabling UHTC-type materials to better survive extreme conditions. In particular, transpiration cooling has been studied by vaporization and emission of a high heat capacity fluid, phase transforming coolants, and a previously proposed electron transpiration method for novel cooling by the emission of electrons from the surface and subsequent reattachment on a different part of the platform.

This dissertation details a materials science-focused study of materials for the future of aerothermal applications. Specifically, it focuses on the rapid processing of dense UHTC and electron emitting materials as ceramic bodies, and the subsequent fabrication of hybrid materials by thin film deposition on a substrate.

1.1. Ultra-High Temperature Ceramics (UHTCs)

Ultra-high temperature ceramics (UHTCs) are special types of materials that can tolerate temperatures well above 2000°C without deteriorating; typically, UHTCs have melting temperature above 3000°C. Because of their remarkable mechanical and thermal resilience, they are well-suited for usage in harsh conditions. Generally, UHTCs are binary compounds of early transition metals and carbon, boron, and nitrogen. Because they are covalent bonded compounds, UHTCs possess important structural advantages, notably high melting point, high mechanical strength (hardness), high thermal shock resistance, and good oxidation resistance [1]. As such, these materials represent suitable candidates for use in structural components of hypersonic vehicles that are likely to be exposed to adverse conditions. Table 1.1 provides a summary of important UHTC materials and their properties.

Table 1.1. List of some UHTC materials and their properties [2-5]

Materials	Melting point (T_m) (°C)	Thermal conductivity (W/mK)	Density (gm/cc)	Work function (eV)	Hardness (GPa)	Elastic modulus (GPa)
HfB_2	3380	104	11.212	3.85	28	480
TiB_2	3225	96	4.5	4.2	25-35	560
TaB_2	3037	86	12.5	3.8	25	550
ZrB_2	3247	60	6.119	3.6	20-25	489
ZrC	3445	35	6.73	3.53	24	402
HfC	3928	25	12.2	3.58	25	428
TiC	3067	6	4.93	3.8	31	489
TaC	3997	22.1	14.3	4.2	14	431
ZrN	3250	6.4	7.09	4.6-4.7	15-23	450

Amongst the UHTCs, ZrB_2 is attractive due to its low theoretical density, high melting temperature, excellent mechanical properties, high thermal conductivity, good oxidation resistance, and low cost [2,5,6]. The ZrB_2 have a primitive hexagonal (AlB_2-type, P6/*mmm* space group) crystal structure as illustrated in Figure 1.1 [5].

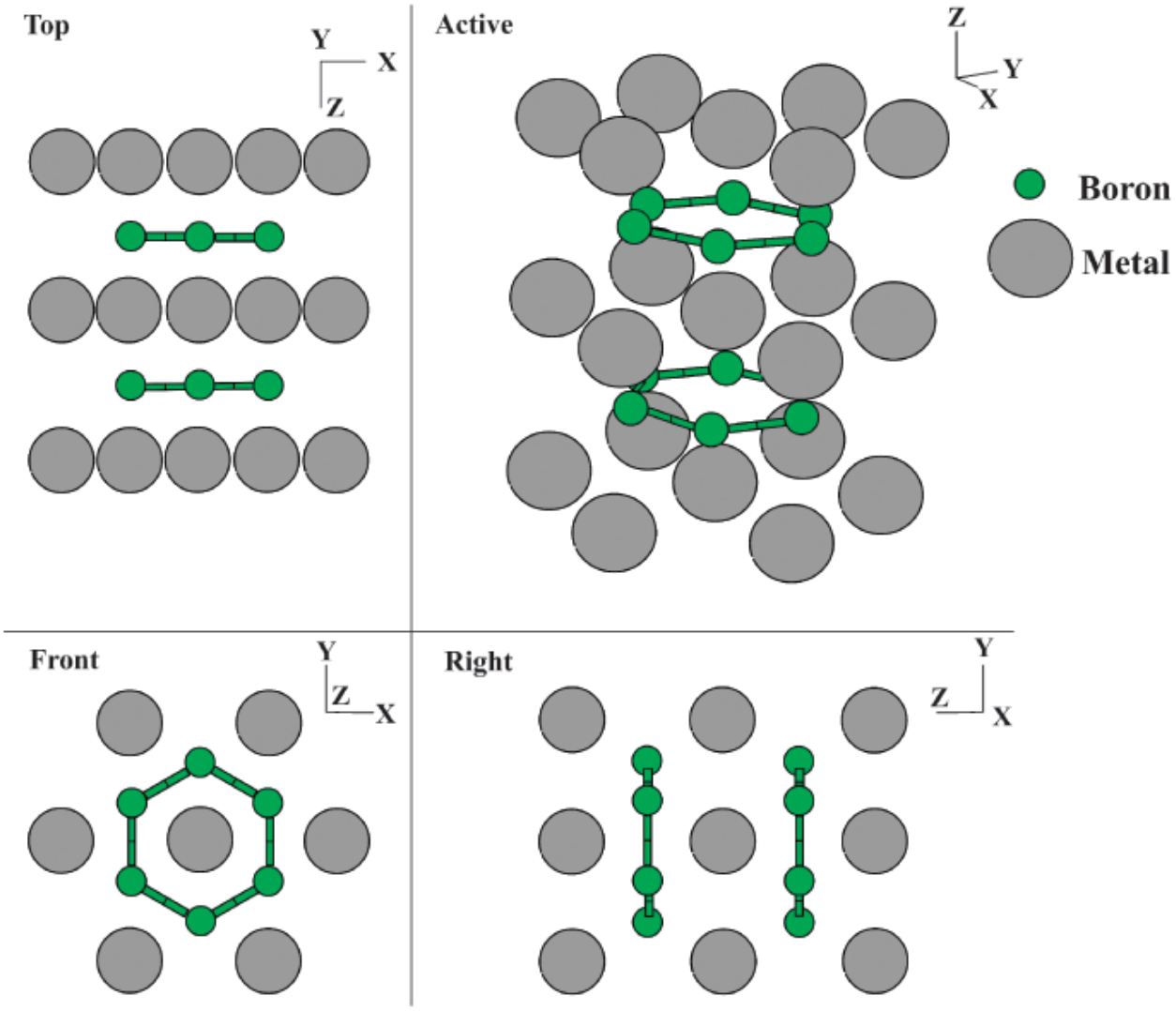

Figure 1.1. Illustrating the crystal structure of ZrB_2 [5].

1.2. Low work function (W_f) materials

The smallest amount of energy needed to extract an electron from a solid and transfer it to vacuum location is termed as the work function or W_f. This factor represents a material's intrinsic characteristic and is commonly expressed in electron volts (eV). However, depending on the material and its surface characteristics, the W_f may change. For instance, surfaces inhomogeneity and the nature of the bulk material on the interior will exert a range of performance functions depending on availability of free electron, defects, and dangling bonds [7]. Furthermore, impurities on the surface and solid solution of electropositive materials will cause weekly bonded electrons on the material's surface to alter the materials W_f [8].

In the case of low W_f materials, electrons can easily overcome the surface potential energy with increasing temperature. Materials with low work functions have been used as thermionic electron emitters in plasma production [9]. Published studies have also described their use as field emission electron cathodes in electron microscopes [10], in applications related to photo-induced electron emission [11], and in solar energy applications [12]. The emitted electron current density can be estimated by the Richardson- Dushman formula,

$$J = AT^2 exp^{(-W_f/kT)} ; \quad (1)$$

where J is the emission current density (Amp $*$ cm^{-2}), T is the temperature, k is the Boltzmann constant, and A is Richardson's constant. If the value of W_f is low, the emission current density will be high at lower temperatures. Bulk and thin-films of LaB_6 and CeB_6 have been well studied for thermionic emitters due to their low W_f, high melting temperature, high thermal and electrical conductivity, moderate hardness and good oxidation resistance [13,14]. Recently, interest has been growing in developing materials with additional reduction in W_f for further improvements in thermionic emitters.

Seven specific low W_f materials are listed in Table 1.2. Among these materials, LaB_6 has a high melting temperature (Tm) of 2715 °C [15] and a W_f range of 2.6-2.7 eV [16]. CeB_6 features a W_f range of 2.5–2.6 eV [17], with Tm = 2550 °C [18,19]. LaB_6 has a W_f =2.6-2.7 eV [16] and a high melting temperature of T_m = 2715°C [15]. Therefore, LaB_6 has been widely utilized in applications as thermionic emitters. CeB_6 has a W_f = 2.5–2.6 eV [17], T_m =2550°C [20,21], good chemical resistance, and low volatility, as well as long lifetime as a thermionic electron emitter [19,22]. Since CeB_6 has a slightly lower W_f (2.5 eV) than LaB_6 (2.6 eV), the thermionic emission current of CeB_6 is predicted to be higher [18,19]. An alkaline earth metal hexaboride, such as barium hexaboride (BaB_6), features an even lower W_f of 2.1 eV [23,24].

Table 1.2. List of some low $\boldsymbol{W_f}$ materials and their properties [25,26]

Materials	Melting point (Tm/ °C)	Thermal conductivity (W/mK)	Density (gm/cc)	Work function (eV)
BaB_6	2270	-	4.3	2.1
CeB_6	2550	5	4.75	2.6
LaB_6	2715	14	4.78	2.7
ThB_6	2195	40	6.4	2.92
CeO_2	2400	7	7.215	2.8-3.2
ThO_2	3390	5.1	10	1.66-3.06
$SrHfO_3$	2927	5.2	7.34	3.56-6

Rare-earth hexaborides (lanthanum hexaboride (LaB_6) and cerium hexaboride (CeB_6)) have a cubic crystal structure, which is isomorphous with CaB_6 belonging to the space group $Pm\bar{3}m$. The crystal structure of these materials is shown in Figure 1.2. The lattice has a metal atom surrounded by eight borons in an octahedra. Each of the octahedral boron atoms has a coordination number of five, as well as covalent bonds with four adjacent boron atoms in the same octahedra

and another one in a different octahedra. The strong covalent bonds give rise to a high hardness and relatively inert chemical properties [27].

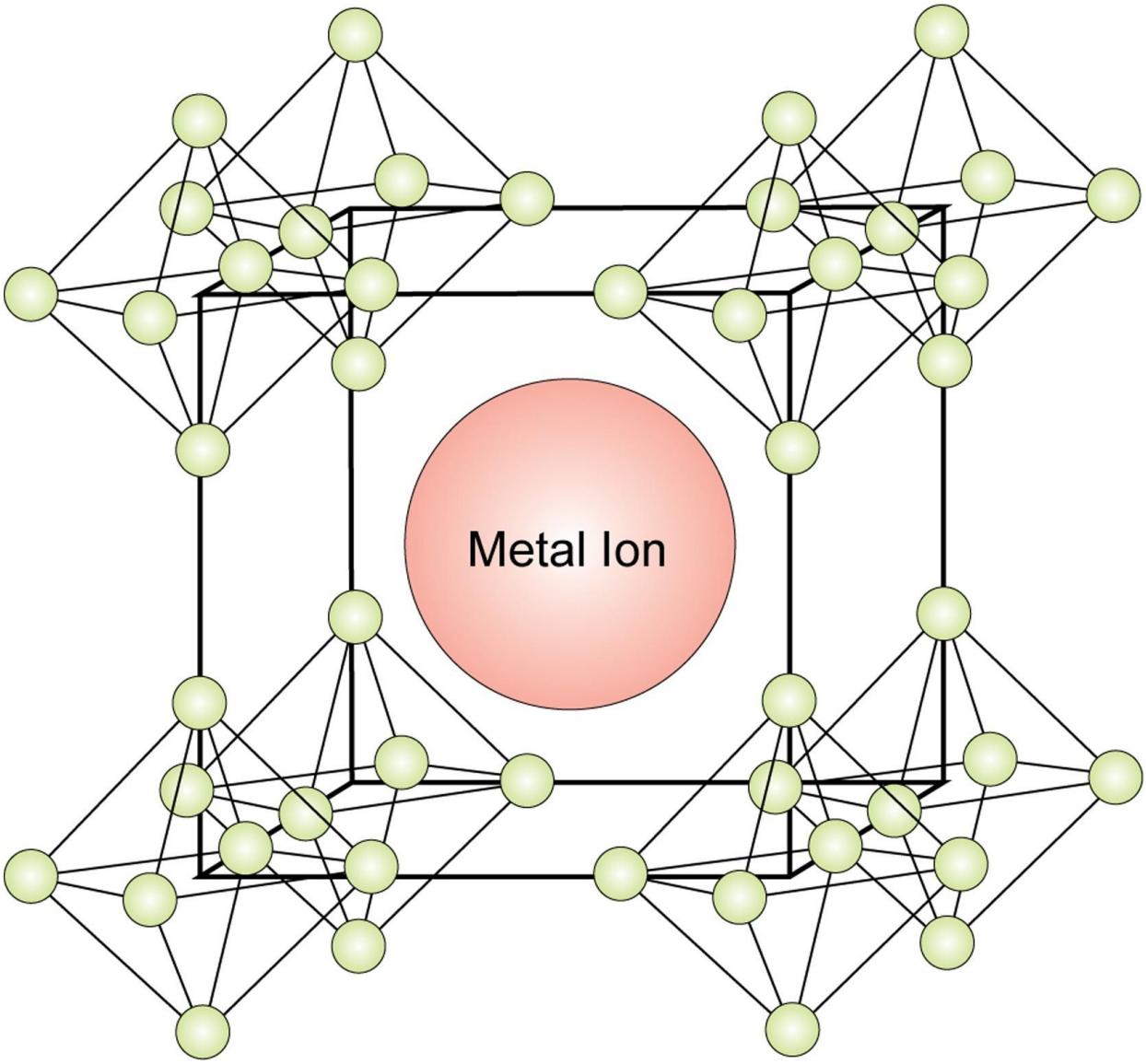

Figure 1.2. Illustrating crystal structure of CeB_6, LaB_6, and CaB_6 [28].

Prior experimental studies have documented that a reduction of W_f in LaB_6-based thermionic emitters can be achieved by adding BaB_6, resulting in an enhanced thermionic current

[23,29,30]. Barium has high electropositivity (low electronegativity), which binds electrons weakly to its surface, substituting Ba into LaB_6 reduces its W_f [23,31]. The $La_{(1-X)}Ba_XB_6$ system forms a complete solid solution due to similar lattice parameters of the hexaboride compounds [28] in different molar proportion of BaB_6:LaB_6 [29]. Similarly, solid solution $Ce_{(1-X)}Ba_XB_6$ can be expected to have a reduced W_f, in addition to other essential properties, such as low vapor pressure and high T_m. However, there have been no prior reports of the fabrication of $Ce_{(1-X)}Ba_XB_6$.

1.3. Stages of sintering

Sintering is a densification process [32]. Essentially, fine particles of a loosely bonded sample are consolidated/densified via high temperature atomic diffusion to form a dense body. The driving force behind this sintering mechanism is the reduction of surface energies of the fine particles and temperature. Because surface energy is proportional to particle size, sintering directly depends on particle size and temperature.

Sintering includes various diffusion mechanisms (e.g., surface diffusion, grain boundary diffusion, and bulk diffusion) and mass transport properties (e.g., surface transport and bulk transport), which occur at different stages of sintering [33]. During surface transport (ST), materials/mass are transported to the neck region from the initial particle surface, while bulk transport (BT) carries mass/atoms from the grain boundary/grain interior to the neck region. Neck growth is primarily favored via ST through surface diffusion and evaporation, without shrinkage and consolidation. Conversely, BT promotes shrinkage and densification by carrying mass/atoms from the grain interior to pore/neck areas through bulk diffusion, volume diffusion, grain boundary diffusion, and plastic flow.

In the first stage of sintering, interparticle necks form through surface diffusion, vapor transport, and plastic flow. After neck formation, substantial concave areas of the neck region will

fill up rapidly with mass from convex areas; this process will continue until the radius of the neck reaches 0.4–0.5 times the initial particle radius. The principal microstructural features that develop during this phase are interconnected pores and particles connected with the neck. Note that all these processes are accompanied by a linear shrinkage of 3 to 5%, with density reaching 65% of the theoretical density.

During the intermediate stage, density reaches ~ 90% and the pores become rounder in shape. Most of the sintering process typically occurs during the intermediate stage, which is largely governed by volume and grain boundary diffusion. The microstructure consists of tube shape pores at the grain edge, circular pore cross-sections, and larger grains. During this stage, vacancies migrate to the grain boundary from the pore areas, while volume changes (through grain growth and grain rotation) occur due to vacancy annihilation.

During the final stage of sintering, one can observe mostly isolated, spherically shaped pores with large grain size. Generally, close pores tend to be located within the grain and near the grain edges. During this stage, it is the BT mechanism that dominates at higher temperatures and helps to remove any entrapped pores by grain coarsening. Research shows that density can reach to more than 90-92% theoretical density and ~8% porosity [33].

During sintering, mass transfer occurs through the bulk and/or across grain boundaries to the pores [32]. Densification is hindered if a concurrent surface diffusion process dominates over bulk diffusion. Surface diffusion causes grain coarsening and reduces the driving force of densification [34]. Slow heating rates are favorable for surface diffusion, as the mechanism has a lower activation energy than bulk diffusion—thus favoring particle coarsening at lower temperature at the expense of making densification more difficult at high temperatures. Accordingly, extreme heating rates are beneficial to avoid the initial and intermediate stages of

sintering [35-37]. Numerical models and experimental results have shown a direct correlation between heating rate, diffusion coefficient, and densification [36,37]. In the final stage, the sintering rate can be modeled as follows [37-39]:

$$\frac{d\,\rho}{dt} = \frac{C\gamma_S D N_g}{G^n} \quad (1)$$

where ρ is density, γ_s is the solid/gas surface energy, *D* is the bulk diffusion coefficient, N_g is the number of boundary pores per grain, *G* is the grain size, and C a constant. The diffusion constant is thermally activated. Thus, the densification rate is directly proportional to the diffusion coefficient.

From a modified Arrhenius equation, the temperature, diffusion coefficient (D), and heating rate for sintering are related (assuming others processing parameters are constant) [35] and can be given as,

$$D(t) = D_0\left(e^{-\frac{Q}{RT(t)}}\right) \quad (2)$$

Where, D_0 is a material constant, Q the activation energy, R Boltzmann constant, and T(t) = T_0 + αt, where T_0 = 298 K and α is heating rate. For higher heating rates (α), lattice diffusion D(t) is accelerated, favoring densification at shorter times. It should be noted, however, that some studies have contradicted prior explanations [40,41].

1.4. Sintering of UHTCs

Due to its very high melting point, ZrB2 displays strong covalent bonding and low self-diffusion coefficients. Thus, the fabrication of fully dense ZrB_2 samples requires a high sintering temperature (<1900^{o}C), as well as a lengthy sintering time and/or the application of high-pressure during sintering [41,42]. One approach to lowering the sintering temperature of ZrB_2 is to use sintering additives [42,43]; nonetheless, the sintering temperature and time remain extreme.

Densification is thus energy consuming, and the sintering additives that lower this temperature are known to deteriorate the essential mechanical strength of sintered bodies for use in high temperature structural components [44].

Another approach for resolving the limitations associated with conventionally sintered UHTCs is to use field-assisted sintering techniques. The methods studied to date involve spark plasma sintering (SPS), hot pressing (HP), and flash sintering (FS) [5,45-49]. However, these field-assisted sintering methods have limitations. The HP and SPS techniques reduce long sintering times. Long sintering times are often a hindrance for the development of the new (materials) compositions, as it prolongs development, increases energy consumption and costs. These techniques normally also require special dies to press samples, restricting the shape and size, which will prevent the fabrication of complex shaped structures. Furthermore, some of these techniques require fine powders and sintering additives. The downside of the former is that fine powder produced by milling can introduce impurities from the milling media. Moreover, sintering additives lower the melting temperature of UHTC materials and facilitate densification by a liquid phase, degrading the high temperature properties of UHTCs [5]. Finally, the FS technique requires (partially)/pre-sintered samples and a conductive ink to connect an electrode-sample junction, complicating the sintering process, as thermal 'hot-spots' often occur due to preferential current paths [50], resulting in the non-uniformity of the sintered bodies.

UHTCs with very high melting temperatures, strong covalent bonding, and low self-diffusion coefficients, achieving fully dense samples is difficult and requires a high sintering temperature (<1900 ^{o}C), long sintering time, and/or application of high-pressure during sintering [41,42]. The principal sintering routes are discussed here. First, in order for conventional pressureless sintering to overcome the requirement of high sintering temperature, different

sintering additives are used to reduce sintering temperature [42,43]. However, the sintering additives that lower sintering temperature have the unwanted side effect of deteriorating the mechanical strength of sintered bodies (e.g., for use in high-temperature structural components) by incorporating low-temperature phases [44]. Second, resolving the issues associated with the conventional sintering of UHTCs is achieved through field-assisted sintering techniques, hot-pressing techniques (HP), and flash sintering (FS) [5,45-49]. The HP and SPS techniques reduce long sintering times and sintering temperature through the use of pressure. The long sintering times create a deterrent for the development of the new (materials) compositions, as it prolongs development and increases energy consumption and costs. However, the main disadvantages are that these pressure-assisted techniques normally require special dies to press samples, restrict the shape and size and the sintered shape shrinks (net shape sample), which prevents the fabrication of complex shaped structures. Third, these techniques often require fine powders (nano to submicron sized) and sintering additives. As noted, fine powders produced by milling introduces impurities from the milling media and surface oxidation. Sintering additives lower the melting temperature of UHTC materials and facilitate densification by a liquid phase, degrading the high-temperature properties of UHTCs [5]. Finally, the FS technique requires (partially)/pre-sintered samples and a conductive ink to connect an electrode-sample junction, complicating the sintering process, as thermal 'hot-spots' often occur due to preferential current paths [50], resulting in the non-uniformity of the sintered bodies. A fast, energy-efficient, and pressureless sintering technique is needed to sinter pure (no additive) UHTCs with complex shaped bodies.

A summary of previous sintering studies concerning the densification of ZrB_2 is provided in Table 1.3. The sintering dwell time to reach high density by a pressureless method was about 60 – 540 min (total cycle time ~550-1000 min), and pressure-assisted sintering (SPS and HP) times

varied between 15 to 120 min (total cycle time ~30-1100 min). Furthermore, some of these sintering cycles included multiple stages prior to achieving the desired (maximum) sintering temperature to facilitate intermediate reactions. A variable heating rate and soaking time were often maintained at each intermediate stage before the desired (maximum) sintering temperature was reached. The soak time for sintering was shorter than the total sintering cycle time, which includes the intermediate sintering stages, the sintering dwelling stage, and the cool down stage. Typically, literature reports indicate that the minimum sintering cycle time is about 33 min for ZrB_2 (relative density 98%) in the absence of sintering additives.

Table 1.3: A summary of previous literature on UHTC ZrB_2 processing parameters, including heating rate, total sintering cycle time, initial particle size, final grain size, final density. Abbreviation used as, spark plasma sintering-(SPS), hot pressing-(HP), pressureless sintering-(PS), attrition milled-(AM), Ball milled-(BM), and high-energy ball milled-(HEBM).

Material, Process, Reference	Temperature, soaking, pressure	Total sintering cycle time (min)	Initial particle size (µm)	Final grain size (µm)	Relative density (%)
ZrB_2 (PS) [51]	15°C/min to 1000°C, 120 min dwell at 1000°C, 15 °C/min to 1450ºC, 120 min dwell at 1000 ºC, 15ºC/min to 1650ºC, 60 min dwell at 1650ºC, 20°C/min to sintering temperature (1900, 2000, 2100, 2150ºC), 180 min dwell at sintering temperature. 360-540 min dwell at 2150ºC, 30ºC/min to room temperature.	~1046	2 µm powder was AM for 2 h at 600 rpm.	9.1 ± 5.6 µm with a maximum grain size of ~30 µm	98
ZrB_2-SiC (PS) [52]	20–30°C/min to 2050 °C, 1 h dwell time at 2050°C	~142 + cooling time	14.2 µm powder was BM for 6 h to make 1.5 µm.	16	93
ZrB_2 (PS) [53]	5°C/min to 400ºC, dwell 2 h isothermally at 400ºC, 5°C/min to 2100°C, 60 min dwell, cooled down at 5°C/min to 1500ºC, cooled down at 10°C/min to room temperature.	~750	2.3 µm powder was BM at 250 rpm for 7 h.	12.4±3.4	92.4
ZrB_2 (PS) [53]	5°C/min to 400ºC, dwell 2 h isothermally at 400°C, 20°C/min to 1900°C, 60 min dwell, cooled down at 5°C/min to 1500°C, cooled down at 10°C/min to room temperature.	~565	2.3 µm powder was BM at 250 rpm for 7 h.	8.1 ± 2.8	91
ZrB_2 (SPS) [54,55]	100°C/min up to 1625°C, 15 min dwell, under 75 MPa, rapid cooling in 1-2 min.	~33	10 nm (2 µm particle was HEBM for 180 min)	~1.5	98
ZrB_2 (SPS) [54]	100°C/min up to 1500°C, 10 min dwell, pressure 20 MPa during heating, 100°C/min up to 1625 °C, 15 min dwell and pressure 75 MPa during dwell, rapid cooling in 1-2 min.	~42	10 nm	~3	100
ZrB_2 (SPS) [54]	100 °C/min up to 2000°C, 15 min dwell, under 75 MPa, rapid cooling in 1-2 min.	~37	500 nm	~30	95
ZrB_2 (SPS) [54,55]	100 °C/min up to 16250 °C, 15 min dwell, pressure 20 MPa during heating, pressure 75 MPa during dwell, , rapid cooling in 1-2 min.	~33	10 nm	~1.5	97
ZrB_2–SiC (SPS) [56]	1900°C for 7 min, under 40 MPa load	7 min + heating and cooling time	<1 µm powder was smiting by an agate mortar.	5.2	99.9
ZrB_2 (HP) [57]	~5 °C/min to 1650 °C under vacuum ~130 mtorr, dwell 1 h at 1650°C, argon fill, ~17 °C/min to 1900°C, dwell 45 min at 1900°C under a uniaxial load of 32 MPa.	450 + cooling duration.	2 µm powder was AM for 2 h at 600 rpm.	6 µm	99.9

ZrB_2 (HP) [58]	20 °C/min to 1450°C under vacuum ~15 Pa, dwell 2 h at 1450°C, 20°C/min to 1650°C, helium fill, dwell 1 h at 1650°C under vacuum 32 MPa, ~50°C/ min to 2100, 2150, or 2200°C, dwell 30, 60, or 120 min, cooled at ~40°C/min.	1101 (18.35 h)	48 h BM of 2 µm powder.	52.1 ± 26.9	97.81 (2150°C for 120 min)

1.5. Synthesis and densification of low W_f materials

Generally, low W_f materials (such as single and multicomponent polycrystalline hexaborides: BaB_6, CeB_6, and LaB_6) were synthesized by (i) direct combustion of boron (B) and metals (such as Ba, Ce, La) [59-61], and (ii) solid state reactions including carbothermal reduction [62], borothermal reduction [63], boron carbide solid-state reduction [62], and metal hydride reaction [30]. The majority of the publications in this area describe the synthesis of mono-component hexaboride powders, which is energy-intensive and necessitates lengthy and high-temperature reaction times [30,59,64]. Due to the necessity of several processing steps involved in some of the hexaborides (powder) production methods, such as vacuum drying and acid washing [65,66], there is a significant amount of resulting chemical waste [17]. Additionally, for thermionic emitter applications, dense mono or multicomponent hexaboride ceramics are required, which can be used as a target for thin film deposition. It is thus important to have a method for preparing a dense, multicomponent hexaboride with pre-selected compositions.

Several bulk sintering methods have previously been used to prepare dense hexaborides, as reported by Zhou et al [30]. For instance, $La_{0.6}Ba_{0.4}B_6$ has been fabricated from mixed powders of B, LaH_2, and BaH_2 by spark plasma (SPS) sintering at 1400 °C for 5 min. Hasan et al. [29] synthesized $(La_xBa_{1-x})B_6$ solid-solutions via a boron carbide solid-state reduction method at 1900 °C in 1 hour. In these sintering routes, the total densification time was long (>15 min to 1 day) and required multiple complicated steps [29], such as numerous long-duration, high-energy milling and multiple sintering schedules [29]. Instead, a rapid, energy-efficient, and straightforward

processing route for highly dense mono- and multi-component hexaborides with no post-processing steps is needed.

However, synthesizing $La_{(1-X)}Ba_XB_6$ is difficult due to the relatively high volatility of Ba, which unfortunately to date requires long sintering times [29,30]. In contrast, ultra-fast high temperature sintering (UHS) is a rapid sintering method [67] with much potential. This approach was recently studied by Wang et al. to sinter different green ceramics via Joule heating by placing them within a sandwiched carbon felt. Heating rates of 10^3-10^4 °C/min were achieved from room temperature to desired sintering temperatures in the range of 1500-2000 °C. The researchers were able to sinter several different oxide ceramics in 10 sec using this UHS method. Different ceramics, such as fine grain Al_2O_3 [68,69], ZrO_2 [70], $BaTiO_3$ [71], high entropy carbides [72], MgO, $La_2Zr_2O_7$, $(La_{0.2}Nd_{0.2}Sm_{0.2}Eu_{0.2}Gd_{0.2})_2Zr_2O_7$, $SrTiO_3$ [73], Si_3N_4 [74], and various metals [75] have since been sintered with this technique.

Here, to address the aforementioned limitations of different sintering/synthesis techniques for UHTCs and low W_f materials, an alternative technique was investigated: an ultra-fast high temperature sintering (UHS) technique, which is similar to the rapid sintering method that was recently reported [67]. Wang et al. directly sintered different green pressed ceramic pellets by this Joule-heating process. A full discussion of this technique/method is available in the experimental section in Chapter 2.

1.6. Thin film of low work function material on UHTCs

Distribution of grains and crystallographic orientations in the polycrystalline materials is termed as Texture (textured materials). The textured materials have some degree of preferred crystallographic orientation and the polycrystalline materials do not have any specific orientation. During thin film deposition, if substrate's crystalline orientation can be imposed in thin film, the

thin film can be termed as epitaxial thin film. In homoepitaxy, the substrate and the thin film are of different material. Presence of particular crystalline orientation in epitaxial thin film causes anisotropic property, which varies from polycrystalline thin film.

Thin films of LaB_6 and CeB_6 have previously been synthesized in numerous ways on various substrates. For example, Craciun et al. deposited LaB_6 thin films on silicon substrates using Pulsed Laser Deposition (PLD) [76]. Late et al. studied PLD deposited LaB_6 thin films on different metal substrates such as tungsten [77]. Mezzi et al. synthesized LaB_6 and CeB_6 thin film by PLD on SiO_2 and SiO_2/Si substrates [78]. DC sputtered deposited LaB_6 and CeB_6 films were reported on tungsten and molybdenum substrate by Waldhauser et al. [79]. Those previous films are deposited on either metal or textured substrates by different sophisticated physical vapor deposition techniques.

However, these prior studies of hexaboride films have focused on using (100) and (111) Si single crystalline substrates, which cannot withstand the ultra-high temperature range of UHTCs [80,81], given that its melting temperature is 1414 °C. Note that it is important to deposit these high temperature hexaboride thin films on UHTCs and study their characteristics. Alternatively, one can consider $SrTiO_3$ (STO) or $SrZrO_3$ (SRO), which have melting points of 2100 ^oC and 2600 ^oC, respectively. The melting temperature range of SRO is close to that of the electron-emitting material, LaB_6, which features the highest melting point temperature of the hexaborides. Since STO is commonly available—and its isomorphous and crystal structure are chemically similar to SRO—STO would make a good candidate substrate.

As an alternative, films incorporating the dielectric material $SrHfO_3$ (SHO) have the potential to emit ballistic electrons with energy greater than the W_f. This is because the bandgap E_g of SHO is high, but its work function W_f relatively low. Furthermore, SHO has a melting point

of 2900 °C and it is isostructural with STO. Therefore, heterostructures of SHO/STO offer a potential model system for the study of epitaxial single crystals and anisotropy.

Various perovskite materials (with the general formula, ABX_3, where A and B are cations, and X is the anion usually oxygen or halogen [82]) are attractive candidates based on their unique features, including their as piezoelectric, ferroelectric, optical, dielectric, magnetic, and photoelectric properties [83-90]. Figure 1.3 illustrates the crystal structure of perovskite materials [96]. Amongst the different perovskites, strontium hafnium oxide or $SrHfO_3$ (SHO) has attracted a lot of attention for its potentially advantageous electrical properties like high-permittivity (κ= 21 - 25 [84,86]) and large bandgap (E_g = 6.1 - 6.5 eV [84,91]) at high temperatures [85,86,92,93]. These physical properties impart SHO films with the potential for use in integrated semiconductor applications, such as next-generation high-K gate dielectrics for transistors and metal-oxide–semiconductor (CMOS and MOSFET) [91,94]. Notably, SHO features a high melting temperature, low thermal expansion coefficient, and moderate elastic stiffness [95].

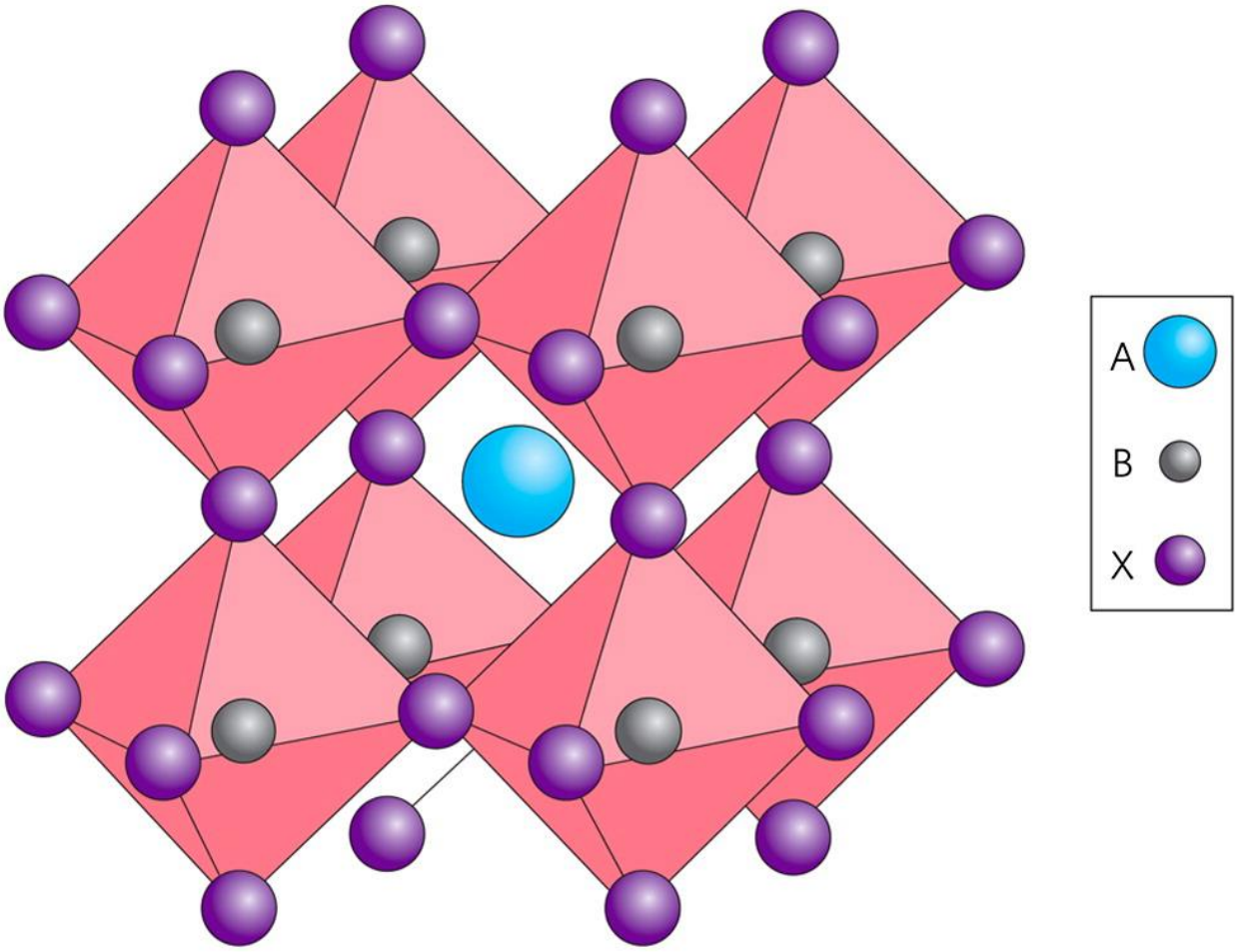

Figure 1.3. Illustrating crystal structure of perovskite materials like $SrHfO_3$ [96].

Like other ABX_3-type perovskites, SHO undergoes a number of phase/structural transformations at different temperatures [97,98]. Kennedy et al. [98] studied the phase transformational sequence of SHO with temperature by powder neutron diffraction. Between 300 and 673 K, SHO has an orthorhombic type structure (*Pbnm;* α_o= b5.752 Å, b_o= 5.764 Å, and c_o= 8.134 Å). A phase group transition occurs between two orthorhombic structures *Pbnm* to *Cmcm* (8.174 Å, 8.197 Å, and 8.179 Å) at 673 K. The high temperature orthorhombic (*Cmcm)* structure then transforms → a tetragonal one (*I4/mcm*; α_t= 5.790 Å, and c_t= 8.212 Å) at 1023 K, which is stable until 1353 K. Finally, a tetragonal (T) → a cubic (C) ($Pm\bar{3}m$; α_c= 4.1131 Å) occurs at 1403

K. Singh et al. [99] studied this high-temperature transformation by Raman spectroscopy and found the presence of two soft phonon modes. They noted that SHO is not ferroelectric below 1023 K, and that the *I4/mcm* → *Cmcm* transition at 1023 K is displacive and nearly second order.

Researchers have detailed several approaches for depositing epitaxial SHO thin films: by molecular beam epitaxy (MBE) [84,94], by atomic layer deposition (ALD) [85], by plasma-assisted atomic layer deposition (PA-ALD) [86], and by pulse laser deposition (PLD) [92]. It must be noted, however, that these approaches tend to be expensive and slow. In contrast, this study describes the deposition of epitaxial SHO thin films using RF sputtering, which is better at growing smooth films with a stable stoichiometry at faster growth rates [100].

RF-sputtering is a physical vapor deposition (PVD) method, which is widely used to deposit oxide and non-oxide single and poly-crystalline thin films on substrates. During sputtering, an electrically excited gas plasma of Ar^+ ions with high acceleration energy bombards the target (i.e., cathode) inside a sputtering gun, forming a plume of atoms evaporated by the target. Argon gas is most often used in the processes to avoid any chemical reaction and phase alteration of the target and substrate materials. RF sputtering, which can be used for both conductive and non-conductive targets, is well known to produce thin films of high chemical homogeneity and phase uniformity, and displaying good adhesion on substrates. Furthermore, this method offers high deposition rate and easy control of film thickness [101,102].

Prior studies have focused on the deposition of epitaxial/ textured SHO films by MBE on (001) oriented Si[84,94] and TiN/Si(100) [93], by ALD on Ge(001) [85], by P-ALD on Si(100) [86], and by PLD on STO(001) [92] substrates. However, the dependence of growth rate on structure-property relationships has not been studied for different substrate orientations; indeed, the structure-property relationships for these films remain poorly understood. We do know that the

complex sequence of phase transitions has the potential to be altered by epitaxial constraint and mismatch, such as offered by growth on different substrate orientations. This factor offers a potential way to engineer its structural property relationship. Thus, for this study, epitaxial SHO thin films were synthesized by RF sputtering on (100), (110) and (111) STO. This is the first report of the effect of orientation on the growth rate and structure properties of epitaxial SHO thin films on STO (100), (110) and (111) substrate via RF stuttering.

1.7. Objectives and significance of the study

This study was designed to develop ultra-fast high temperature sintering (UHS) systems capable of producing various dense UHTCs (such as ZrB_2, HfB_2 and TiB_2) and low work function materials (such as LaB_6 and CeB_6). An important component of this study involved developing a process to lower the W_f of low W_f materials and measure the W_f of different materials by Kelvin probe force microscopy (KPFM). Finally, this study also details the synthesis of epitaxial and non-epitaxial thin films of low work function materials and their characterization.

The main investigation goals are listed below:

(1) Produce highly dense ZrB_2 by UHS technique using commercial ZrB_2 powder and its characterization.

(2) Synthesize and densification of low W_f materials (such as BaB_6, $Ba_{0.5}La_{0.5}B_6$ and $Ce_{0.5}Ba_{0.5}B_6$) via the UHS method and determine work function measurements using the KPFM method.

(3) Deposit epitaxial $SrHfO_3$ on (100), (110), (111) $SrTiO_3$ samples by RF sputtering and determine their characterization.

(4) Deposit CeB_6 thin films by RF sputtering on ZrB_2 and conduct thin film characterization.

CHAPTER ii. EXPERIMENTAL PROCEDURES

2.1. Sample preparation

In the present research, powders and bulk samples were synthesized and sintered via ultra-fast high temperature sintering (UHS), after which thin film samples were deposited by RF-sputtering. In this section, an explanation of both these processes, as well as a discussion of other commonly used characterization techniques, are provided.

2.1.1. Ultra-fast high temperature sintering (UHS)

UHS is a Joule heating or resistive heating technique powered by electricity. Recently, Wang et al. demonstrated a novel technique similar to UHS by directly densifying a green pressed ceramic pellet between sandwiched carbon felt. An extremely fast heating rate (10^3-10^4 ^{o}C/min) can be achieved with this technique, which enables the sample to reach 1500 - 2000 °C from room temperature in 30 sec through thermal conduction [67]; the authors demonstrated success in sintering a wide variety of oxide ceramics in 10 sec using this rapid sintering technique. Following a similar approach, different ceramics such as fine grain Al_2O_3 [68,69], ZrO_2 [70], silicon nitride [74], MgO, $La_2Zr_2O_7$, $(La_{0.2}Nd_{0.2}Sm_{0.2}Eu_{0.2}Gd_{0.2})_2Zr_2O_7$ and various metals [75] were sintered for this investigation. At the time this research was initiated, the UHS technique had not yet been implemented in the synthesis and densification of pure and commercial UHTC powders and low W_f materials.

As shown in Figure 2.1, an experimental laboratory USH setup was installed. The main assembly (Figure 2.2 a-c), which included the carbon felt, a tungsten electrode, and the sample, were maintained within a steel chamber to protect it from oxidation. To regulate the sintering atmosphere, a vacuum pump and argon gas were attached to the chamber (see Figure 2.1 a-b).

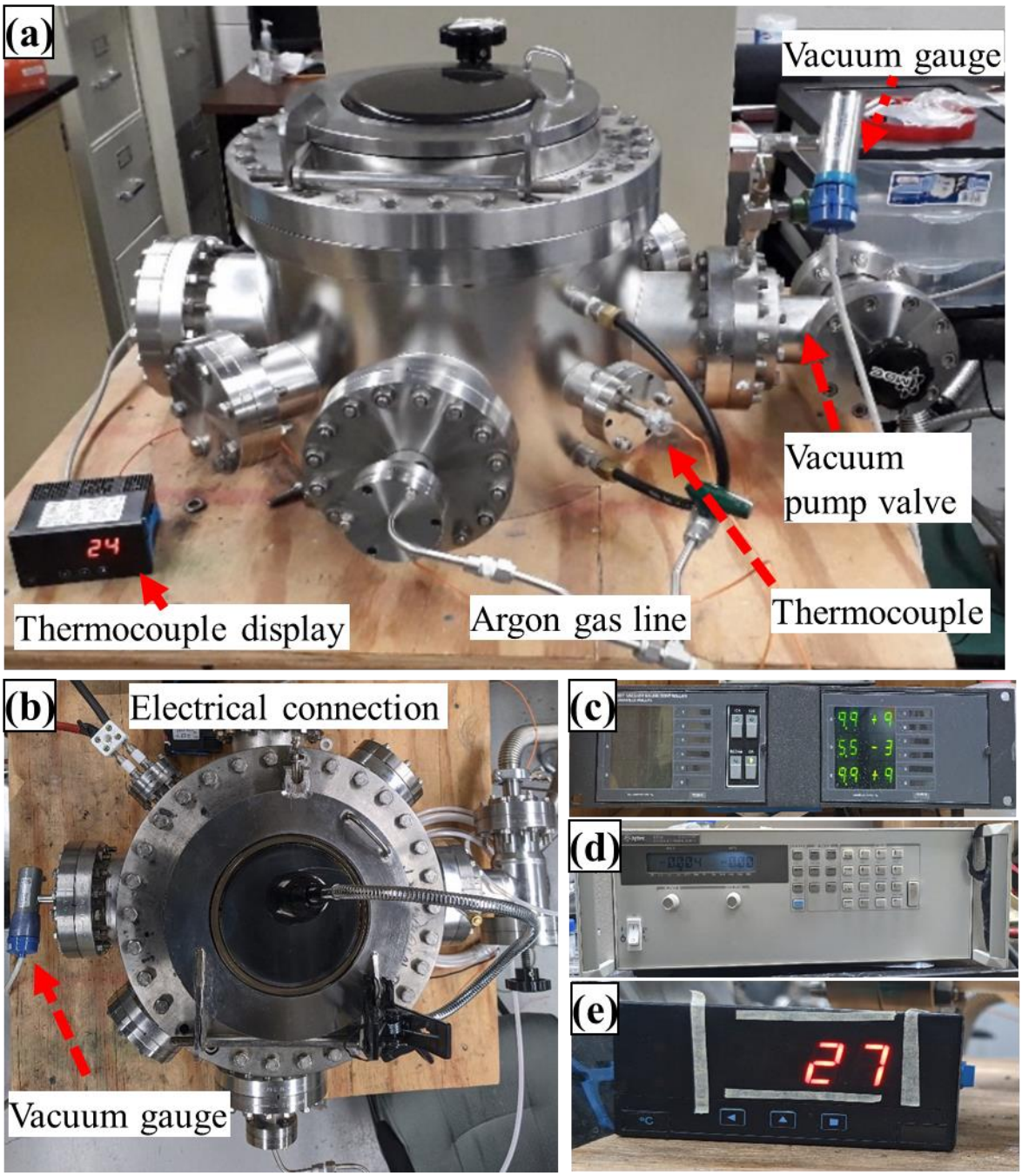

Figure 2.1. Experimental UHS setup: (a) Front view of UHS chamber and positions of different inlet channels for Ar line, vacuum gauge, vacuum pump connection, thermocouple, and thermocouple display; (b) Top view of UHS chamber shows the positions of different inlet channels for Ar line, vacuum gauge, vacuum pump connection, and electrical connection; (c) vacuum gauge monitor; (d) Agilent power source for UHS sintering; (e) thermocouple display.

Prior to sintering, the pressed green pellets were sandwiched between the carbon felt that served as a resistive heating source (i.e., a cavity was created on the side of the carbon felt so that the green pellets could be inserted for sintering). The UHTC samples were placed in the center of the carbon felt, which had been cut to dimensions of ~25 x 7 x 5 mm^3 to ensure that resistive heating was concentrated on the center area where the temperature was monitored. Pressed pellets (5mm diameter, 1-2mm thick) were placed close to the carbon felt to ensure even heating and to reduce any thermal gradients between the felt and sample. To ensure good electrical contact with an electrical power source, the felt was bolted with two tungsten electrode rods, and the rods were attached to a copper wire and subsequently to the power source. The felt-sample setup was placed inside a stainless-steel chamber that was first evacuated to a vacuum of ~~ 3.33 Pa (2.5 x 10^{-2} Torr), followed by flushing with Ar gas, after which the chamber was kept at a constant vacuum of ~2.5*10^{-2} Torr during sintering. We studied the sintering process in vacuum and in an Ar gas atmosphere, but subsequently selected vacuum because it reduced thermal losses from the carbon felt.

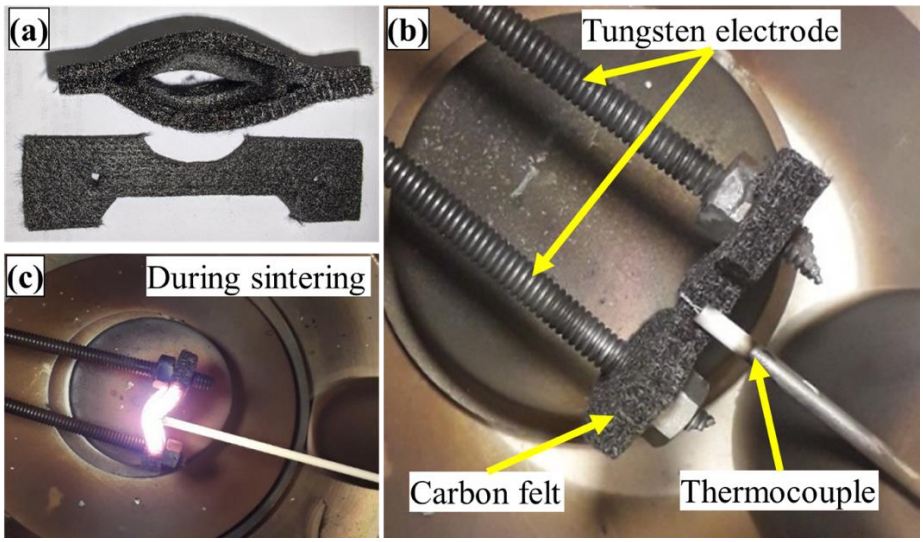

Figure 2.2. The main assembly: (a) carbon felt; (b) carbon felt attached with tungsten metal rod before UHS; (c) carbon felt attached with tungsten metal rod during UHS.

A large percentage of the heat generated in the carbon felt during UHS sintering was wasted by radiation toward the surroundings and not utilized, as shown in Figure 2.2c. As a result, the entire sintering process became less energy efficient. Some previously reported studies involving UHS and other sintering techniques have also described a similar issue, which can be mitigated by utilizing appropriate thermal insulation [70,103]. In this study, a second set of similar carbon felting used as thermal insulation was placed on the center portion of the main heating carbon felt and sample assembly (see Figure 2.3a-c).

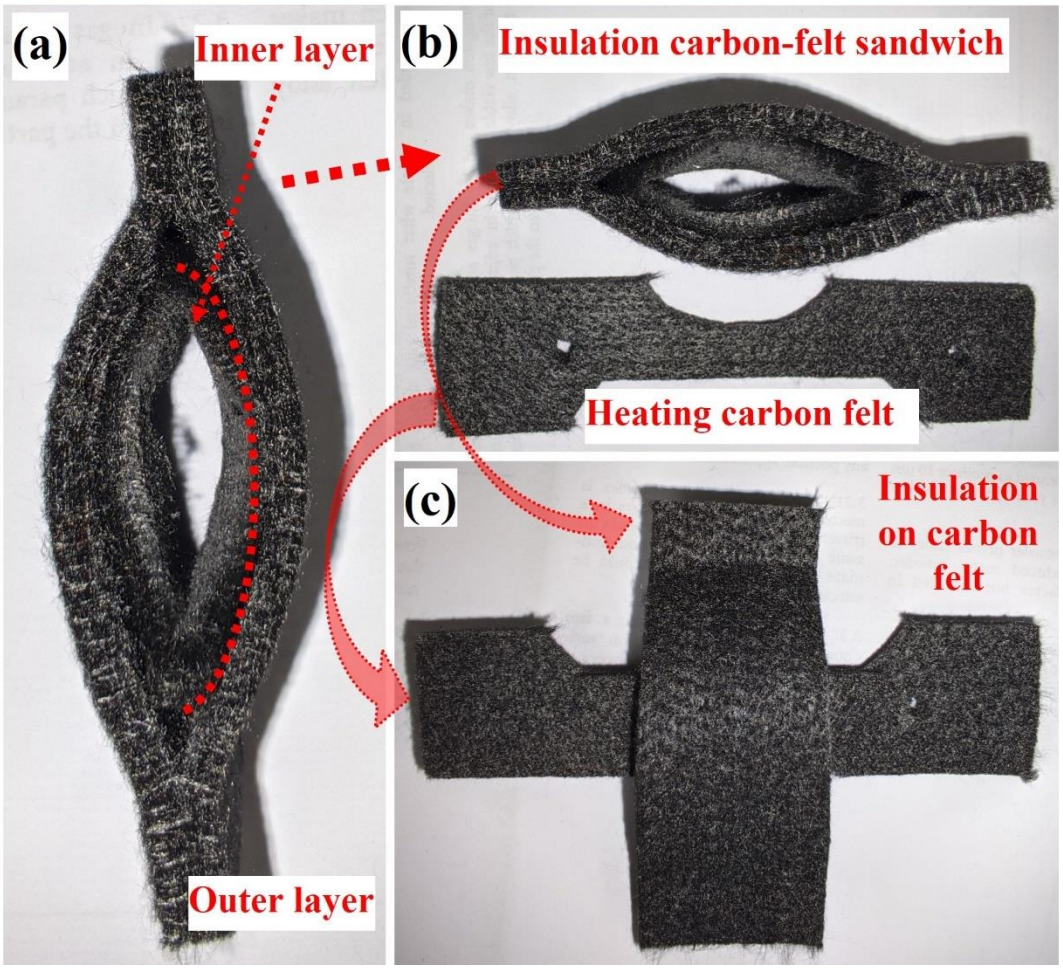

Figure 2.3. UHS system used (a-c) UHS setup, carbon felt insulation layer of carbon felt sandwich assemble.

Using a programmable DC electrical power supply (shown in Figure 2.1d), a ramp-up current was used to heat the carbon-felt to the reaction and sintering temperature range of 1300 to 2600 °C (0 - 35V, 0 - 61 A, Agilent 6673). After reaching the desired temperature, the current was regulated to maintain a stable temperature throughout the heat-treatment process. After sintering, the power was turned off, and the temperature dropped within 15 - 30 seconds. The temperature was measured by placing a C-type thermocouple (Tungsten-Iridium, Evolution Sensors and Controls.llc, Nj, USA) near the sample inside the carbon felt below 2200 °C, as shown in Figure 2.2b-c. Finite element modeling (FEM) using COMSOL-5.3a was performed to calculate the sample temperature and its distribution. Due to heat dissipation at the surface of the carbon felt, a difference of about 50 -100 ^{o}C was found near the sample surface compared to the measured temperature. The FEM method has previously been used to estimate sintering temperatures in both flash-sintering and ultra-fast high temperature sintering (UHS) [45,69,104]. For the present work, different UHTCs (HfB_2, TiB_2, and ZrB_2) and hexaborides (BaB_6, LaB_6, CeB_6, $Ce_{0.5}Ba_{0.5}B_6$, $Ba_{0.5}La_{0.5}B_6$) underwent UHS sintering; those sintered samples were used in subsequent phases of this investigation.

2.1.2. RF sputtering

Sputtering is a thin film deposition technique, whereby higher energy ions are used to physically eject the solid surface atom of a target material by transferring its energy (momentum). The ejected atoms are then accelerated by an electromagnetic field to be deposited on the substrate. In practice, sputtering techniques are widely used in industrial processes because high quality films can be obtained at low temperature. Various types of sputtering techniques such as DC, RF, magnetron, and ion beam sputtering are available. Among them, RF-sputtering is designed for insulating/dielectric target materials. Specifically, RF-sputtering is a physical vapor thin film

deposition (PVD) method that is widely used to deposit various oxide, non-oxide, and metal single and poly-crystalline thin films on substrates.

Our RF-sputtering system (see Figure 2.4a) is composed of two electrodes: one acts as the cathode and other serves as the anode. In general, the target (material) used to conceal the cathode and the substrates is positioned on the anode side. In an RF-system, a RF-voltage is applied on the target, which prevents surface charge buildup on the insulating target (cathode) [105,106]. The sputtering system (main chamber) is filled with a low-pressure gas mixture/argon. When biased voltage occurs between the electrodes, the low-pressure gas creates a glow discharge/plasma, which is attributed to the fact that the Ar gas breaks down into Ar^+ and e^-. Due to this discharge, insulating Ar transform into electrically conductive media. As this discharge process continues, additional Ar^+ and e^- forms, after which this newly generated ionic species collides with neutral Ar and forms additional Ar^+ and e^-. This process then results in a glowing discharge (see Figure 2.3b).

Once Ar^+ and e^- ions are formed, they accelerate toward the anode and cathode, opposite charges, respectively. In the magnetron sputtering system, an applied electromagnetic field accelerates the ions generated in the glow discharge to heat the cathode and sputter the cathode target to create an ejected atom cloud. These ejected atoms are then deposited on the substrate placed at the anode side. A schematic of the RF-sputtering chamber is shown in Figure 2.3d. Argon gas is most often used in this process to avoid any chemical reaction and phase alteration of the target and substrate materials. RF sputtering can be used for both conductive and non-conductive targets. The RF sputtering technique is well known to produce thin films of high chemical homogeneity and phase uniformity that demonstrate good adhesion on substrates. Furthermore, this method offers high deposition rate and easy control of film thickness [101,102].

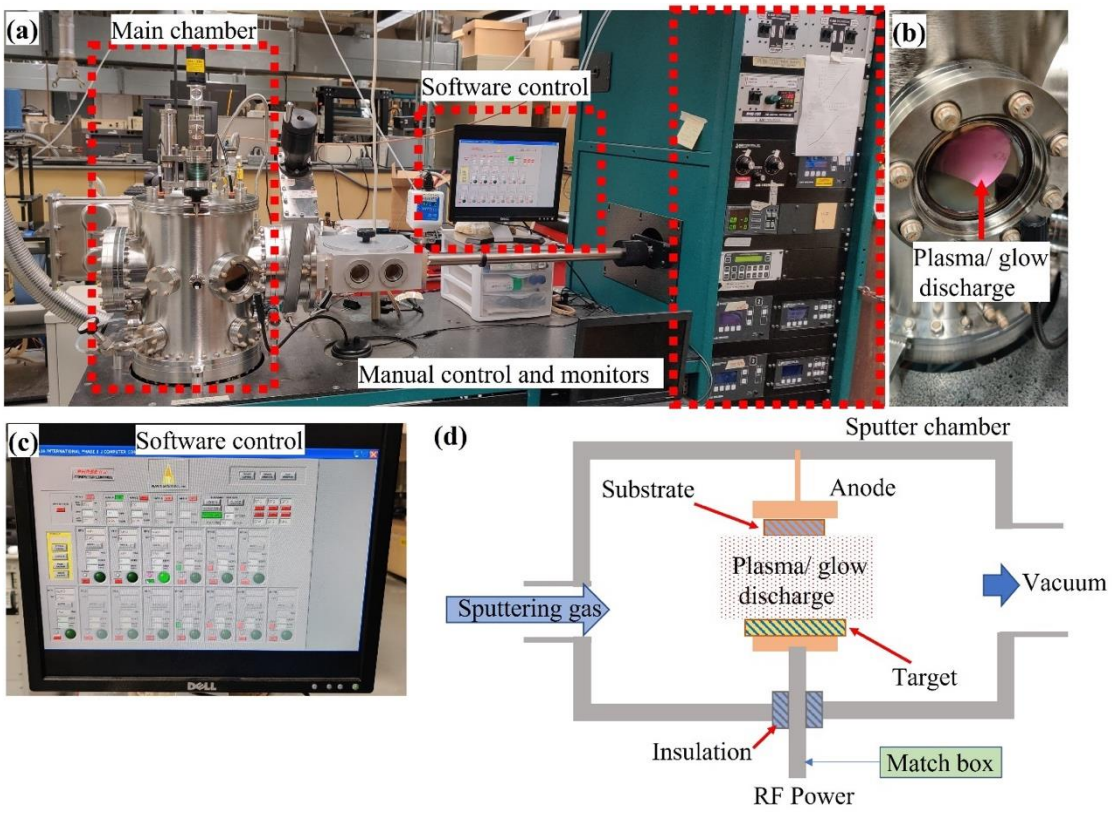

Figure 2.4. RF Sputtering Unit

(a) Front view of RF Sputtering system and positions of different parts such as main chamber, software control, and manual control interface; (b) Peephole shows plasma glow during sputtering; (c) Software control monitor; (d) Schematic diagram of RF plasma working principle.

For this investigation, various single crystal and bulk UHS sintered substrates were used for preparing different thin films of low work function (CeB_6) and high temperature dielectric ($SrHfO_3$) materials. We used an RF-sputtering unit (ACT Orion, A300 series, A3CV & CTM magnetron sputtering, AJA International, Inc, Massachusetts, USA), as shown in Figure 2.3a. Prior to deposition, all substrates were cleaned twice by sonication in ethanol for 10 minutes to remove

dirt and oil. The cleaned and dried substrates were then attached to the substrate holder with the help of silver/high temperature carbon paste. During sputtering, either pure Ar (10 standard cubic centimeter per minute or sccm) or a gaseous mixture of Ar (8 sccm) and O_2 (2 sccm) at different pressure levels (15-30 mTorr) was used. The deposition temperature of 600 ° C was maintained during sputtering for all films; additionally, each substrate was held for 30 min in Ar gas at 600 ^oC before / after the deposition process for uniformity, and subsequently cooled to room temperature at a rate of 10 °C/ min. A total deposition duration of 3 - 6 hour (h) was maintained for all experiments. The distance between the target and substrate was about 10 cm, and films were deposited using a RF power of 100 W.

2.2. Characterization methods

After completing the UHS sintering of bulk samples and the sputtered thin film samples were processed, they were then characterized to determine various properties such as density, phase and crystal structure, microstructure and elemental analysis, epitaxial/textural quality, work function, and surface morphology; electron transpiration cooling was also monitored. The specific experimental approaches for characterizing the thin film samples are provided in the following sections.

2.2.1. Density

A standard Archimede's method was used to determine the densities of the UHS sintered samples [33] using water as measuring fluid, and soaking/boiling each sample prior to measurement following standard procedures. Prior to obtaining the Archimedes density measurements, the sintered samples were also cleaned with a 60 grid SiC grinding paper to eliminate any carbon on the sample surface from the carbon felt. The following method was used

to obtain these measurements (with the assistance of Drs. Carolina Tallon and Kathy Lu at Virginia Tech):

W_1= dry weight of the sample (after dried at 110 ^oC)

W_2= The samples were boiled in isopropanol/water for 2 hr and immersed in isopropanol/water for 12 hr. Then, the sample weights were obtained when the samples were immersed in an isopropanol/water mixture, which is known as the suspended weight.

W_3= The wet samples were blotted on both sides with a moistened cotton cloth to remove all water droplets from the surface. The resulting weight measurement is known as the soaked or saturated measurement.

Calculation bulk density (BD)= $W_1 \times \emptyset/(W_3 - W_2)$, where $\emptyset$ =density of isopropanol/water at room temperature. The relative densities were calculated using the theoretical density of of the material (for example for ZrB_2, theoretical density is 6.09g/cm^3 [107]).

2.2.2. X-ray diffraction technique and reciprocal space mapping

After UHS sintering and thin film deposition, the samples were tested under X-ray diffraction (XRD) for phase and crystal structure analysis. Sample surfaces were polished prior to XRD to remove any contamination from the carbon felt, and the samples were rotated to ensure that diffraction occurred over a wide area surface. Line scans were collected from 2θ =20 to 80°, at an angular increment of 2° min^{-1} using CuK_α radiation operated at 40 kV and 40 mA. XRD of initial powders was done using a wide-angle X-Ray Diffraction (Bruker D8). The sintered samples were then ground with a 60 grit SiC paper to remove any carbon deposits on the sample surface from the carbon felt before testing. To calculate the lattice parameter, Bragg's law was used as given in the equation and schematically illustrated in Figure 2.5.

$$n\lambda = 2d\ sin\ \theta$$

Where, n is an integer, λ is wavelength of the incident X-ray from $CuK_{\alpha 1}$ (1.5459 Å), d is distance between two atomic planes, θ is angle between incident X-ray and sample surface.

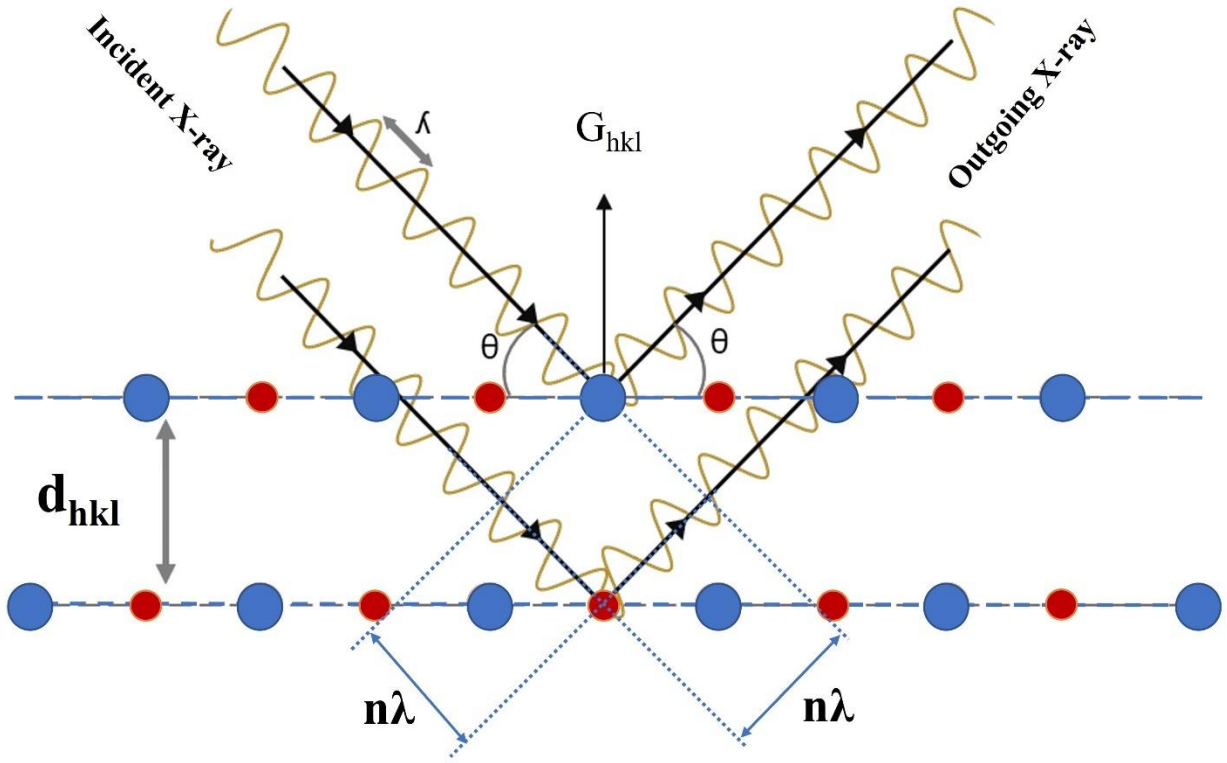

Figure 2.5. A schematic of Bragg's law to visualize interaction of X-ray beam with crystal plane.

When parallel X-ray beams interact with the atomic planes of a crystalline material, constructive interference occurs, while the additional path travelled by the ray is equal to an integer number (n) of wavelength of the X-ray. For textured and single crystalline materials, it is important to consider a scattering vector, G_{hkl}, which can be defined as the incoming X-rays that must be aligned with the normal vector of the atomic plane to be measured.

XRD reciprocal space mapping (RSM) was performed (PANalytical X'Pert MRD Pro) to evaluate the epitaxial / textural characteristics of the thin films. RSM scans were obtained with a

CuK_α radiation (λ = 0.1542 nm, operated at 45 kV and 40 mA). Each scan was performed using an approximate substrate main 2θ peak at a 2θ increment of 0.02 °. For example, the SHO/STO(110) film was scanned between 2θ = 29.071 to 34.071 °, likewise, SHO/STO(100) and (111) were scanned between 2θ = 42.582 to 47.582 ° and 37.431 to 42.431 °, respectively.

2.2.3. Scanning electron microscopy and energy-dispersive X-ray spectroscopy

In this work, SEM imaging analysis was also conducted on both the polished and fractured sample surfaces of UHS sintered and thin film samples. Microstructures were examined by field emission electron microscopy (JSM IT-500HR, JEOL). Elemental distribution, phase homogeneity, grain boundary chemistry, and elemental homogeneity at grain boundaries were analyzed by energy dispersive X-ray spectroscopy (EDS, Oxford Instruments) and an AZtecLive automated microanalysis system (Oxford Instruments). For calibration of the EDS analysis data, a standard sample, stainless steel (PELCO XCS-5, Calibration stub#5) was used as shown in Figure-2.6; a deviation of 5-10 % was observed from measured and standard samples as shown in Table-2.1. The ImageJ software (version 1.53e) was used to measuring the grain size of the SEM images. To achieve a good statistical estimation, 300-500 grains were assessed for each sample.

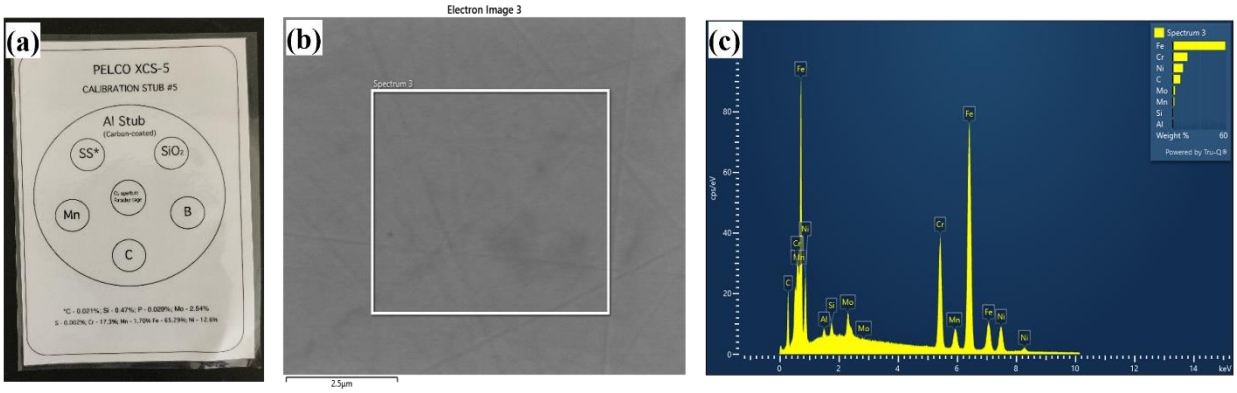

Figure-2.6: (a) A schematic of the stabs and composition; (b) Secondary electron image of the stainless steel as mentioned in the schematic; (c) EDS analysis spectrum of the selected area on the secondary electron image.

Table-2.1: This table contains recipe of standard samples, EDS measured data, deviation and difference.

Element	Standard sample (wt %)	EDS measured data (wt %)	Deviation (%)	Difference
Fe	65.29	58.77±0.18	9.98	6.52
Cr	17.30	16.36±0.10	5.43	0.94
Ni	12.6	11.44±0.14	9.20	1.16
Mn	1.70	1.75±0.08	-2.94	-0.05
Mo	2.54	2.43±0.08	4.33	0.11
Al	-	0.34±0.03	-	-0.34
Si	0.47	0.49±0.03	-4.25	-0.02
C	0.021	8.41±0.13	400 times	-8.39

2.2.4. Kelvin probe force microscopy

After polishing each sintered sample's surface, Kelvin probe force microscopy (KPFM) was performed to measure the work function of the material. We used atomic force microscopy (AFM) (Oxford Jupiter XR AFM) and Asylum software with a Ti / Ir-coated silicon AFM probe (ASYELEC-01-R2) in KPFM mode. The KPFM measurement consisted of two separate scans of the specimen surface. The first pass scanned the topography, where the probe was mechanically driven in a tapping mode. The second pass scanned the surface potential while maintaining a constant distance $\Delta H = \pm 10$ nm between the probe and sample. Contact potential difference (CPD) between the sample and the AFM tip was balanced by an applied DC voltage between the tip/sample. The voltage was thus equal to the potential difference between sample and probe. An average of four scans were obtained to reduce experimental errors.

The scan of W_f was calibrated against a reference sputtered sample of gold (Au) having a known W_f. However, Au has been reported to have a significant range of W_f values between 4.68 eV [108] to as high as 5.3 eV [108,109], which may be due to surface contamination and testing conditions. The scatter in the W_f values of Au, therefore, introduced some uncertainty in the W_f

calibration. Thus, additional calibration measurements against LaB_6 and CeB_6 with known W_f materials were also performed. We stress that careful sample surface preparation was conducted prior to the AFM probe calibration for the KPFM scan. Contaminants such as O, C, and H-containing compounds on the sample's surface can notably change the measured value of W_f. Thus, surface cleaning of a sample prior to calibration and testing by KPFM is crucial.

2.2.5. Oxidation testing

Oxidation tests were performed in a TG furnace (TGA 5500, TA Instruments) at 1100 °C for 60 min in 100ml/min air flow on the UHS samples that had been sintered for 60 sec. After the specimens were loaded in the furnace, the samples were heated at 10 ^{o}C/ min to reach the target temperature, held at that temperature for 60 min, and then cooled. Data was collected after mass and flow stability. The post-oxidation samples were then characterized by XRD for phase identification, as well as by FESEM to detect any microstructural changes due to surface oxidation.

2.2.6. Nanoindentation

Nanoindentation experiments were performed utilizing a commercial nanoindenter (NanoTest Vantage, Micro Materials Ltd, UK) with a diamond Berkovich indenter on the polished sample surface. The indenter was continuously loaded to a peak load (load control) and then unloaded after a 10 sec holding time at the maximum load. Two peak loads of 20 and 200 mN were used. The hardness (H) and Young's modulus (E) were calculated according to the data acquisition and analysis software based on the model of Oliver and Pharr [110]. The software for the nanoindenter considers different factors during analysis: the machine compliance, thermal drift, and an ideality function for a Berkovich indenter (24.5) between the raw loading–unloading conditions. The area function of the indenter was calibrated using a standard fused silica specimen.

2.2.7. Atomic force microscopy

After deposition, the surface morphology and topography of the thin films were characterized by atomic force microscopy (AFM) (Dimension 3100, Vecco) in a tapping mode. Figure 2.7 provides a schematic of the AFM configuration. To understand AFM's working principle, it is important to know (a) the interaction forces between the AFM tip and the sample, and (b) the AFM tip and photo detector loop. With respect to the first factor (interaction forces between the AFM tip and the sample), there are three considerations: (I) When the sample surface and tip distance is far, force is negligible; (II) An attractive force acts between the tip and the sample when their distance is closer due to Van der Waals force; and (III) A strong repulsive force acts between tip and sample when the distances are very small due to electrostatic repulsive forces. Regarding the second factor ((b) AFM tip and photo detector loop), when an AFM tip and the cantilever is programmed to oscillate up and down over the sample surface at its resonance frequency, based on the sample and AFM tip distance (height/Z), the interaction force between tip and sample changes; and that change in interaction force results in bending the cantilever up or down. A laser beam was applied to the apparatus, and then reflected by the shiny cantilever to a sensitive photo-detector, which was able to determine the cantilever deflection and record the surface topography of a sample.

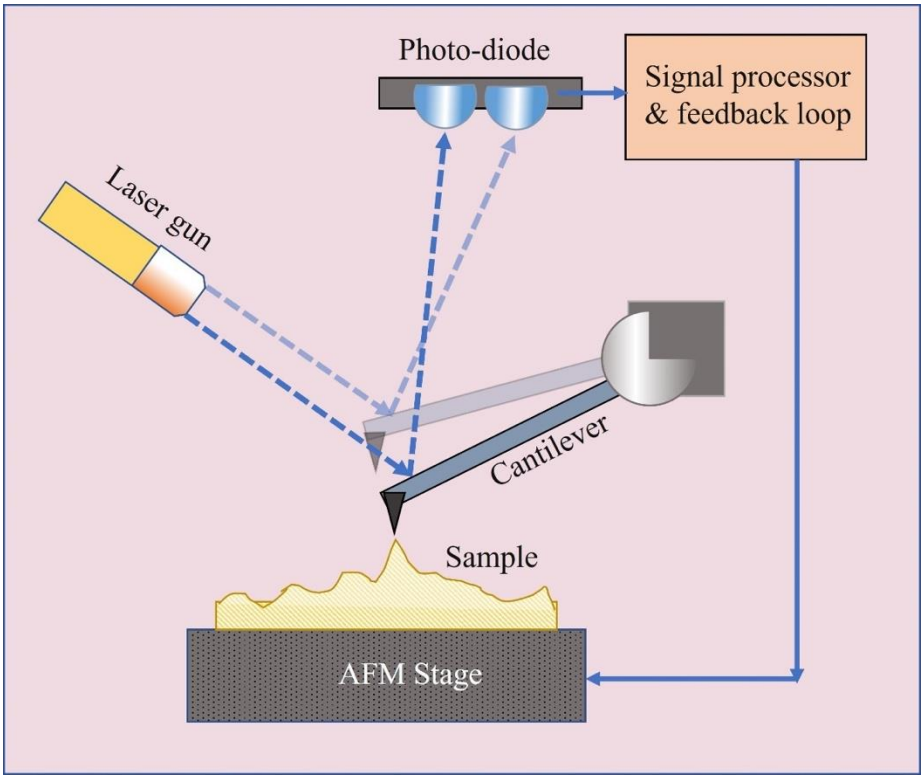

Figure 2.7. A schematic of AFM working principle

CHAPTER iii. ULTRA-FAST HIGH TEMPERATURE SINTERING OF ZrB_2

Part of the research was published in the Journal of the American Ceramic Society in 2023. Reference: Santanu Mondal, Juan Diego Shiraishi Lombard, Sreenivasulu Gollapudi, Carolina Tallon, Jie-Fang Li, Dwight Viehland. (2023). "Ultrafast high-temperature sintering of ZrB_2." Journal of the American Ceramic Society. https://doi.org/10.1111/jace.19445.

Zirconium diboride (ZrB_2) is an ultra-high temperature ceramic (UHTC) with a very high melting point. Thus, its densification is difficult, energy intensive, and time-consuming. Here, we have used ultra-fast high temperature sintering (UHS), which is a joule heating method with an extremely high heating rate, to sinter ZrB_2 in seconds in an energy-efficient way. Commercial ZrB_2 powders were rapidly densified by UHS to >90% relative density within 60 second in vacuum without pressure. This is the fastest sintering and densification time reported to date for a pure UHTC.

The effect of sintering time on densification and final grain size were studied at sintering temperature. Bulk density improved from 75 to 93% of relative density by increasing the sintering duration from 10 to 60 seconds. The final grain size increased from 2.7 ± 1.1 μm to 19.0 ± 8.4 μm when the sintering time was increased from 10 to 60 seconds. X-ray diffraction and energy dispersive analysis by X-ray were conducted to determine crystalline phase, compositional heterogeneity, and grain boundary compositional uniformity. Density, grain size, phase stability, and grain boundary composition were studied. Nanoindentation confirmed that UHS ZrB_2 displayed an average hardness of ~19 GPa and an elastic modulus of ~373 MPa at 200 mN load; moreover, thermogravimetric analysis testing at 1100 $^{\circ}$C in air revealed high oxidation resistance. These findings were compared to other sintering techniques.

3.1. Experimental

Powders of ZrB_2 (grade B, purity ≥99% (metals basis), D50 = 2.3 um) were procured from H. C. Starck (Karlsruhe, Germany). The grain size is listed in Table 3.1 -below. A powder X-ray diffraction line scan (XRD) and a scanning electron microscopy (SEM) image are shown in Figure 3.1a and b. The as-received powders were uniaxially pressed in a cylindrical shaped stainless-steel die (Precision Elements Ltd, Michigan, USA) using a pressure of 125 MPa pressure. The disk-shaped pellets had a diameter of 5 mm and a thickness of 1 ± 0.1 mm. All the pellets were pressed without a binder and dried to 100 ^oC (to remove any absorbed moisture). The initial green densities were determined to be approximately 57 - 60% of theoretical from the weight and dimensions of the pellets. The dried pellets were sintered inside a carbon-felt by joule heating.

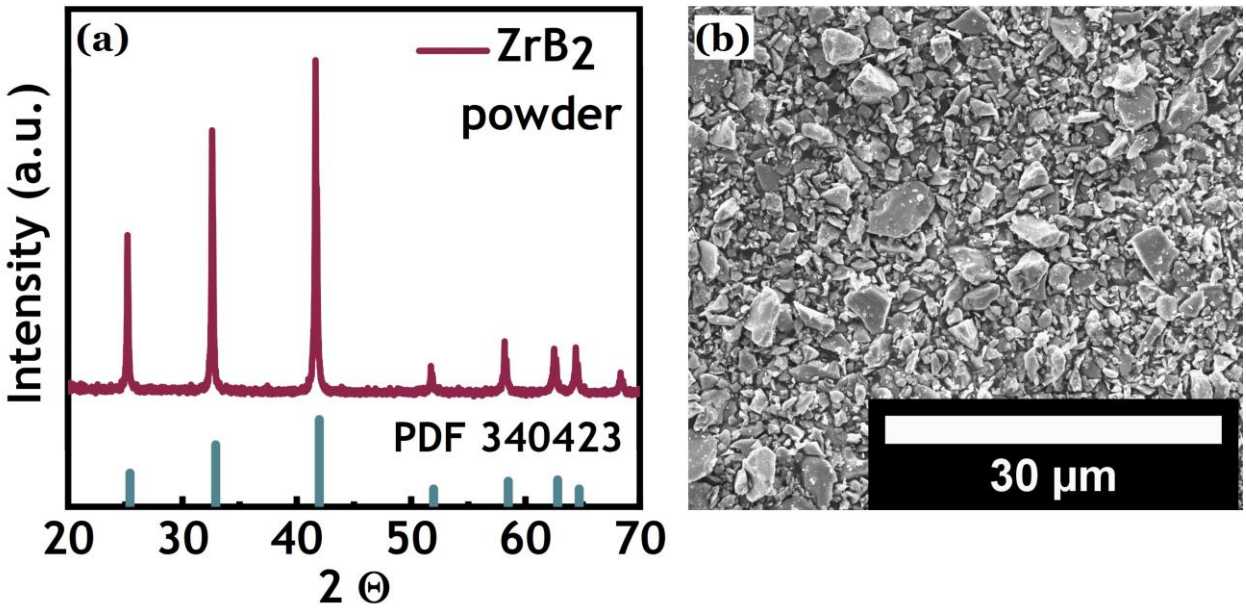

Figure 3.1: (a) SEM image and (b) XRD plot of ingredient ZrB_2 powder.

3.1.1. Ultra-fast high temperature sintering set-up

I used an ultra-fast high temperature sintering (UHS) technique, which is similar to a rapid sintering method that was recently reported[67]. Wang et al. directly sintered green pressed

ceramic pellets by placing them between a sandwiched carbon felt via Joule-heating. Samples were heated inside two thin carbon-felts. A sintering time of 30 sec (seconds) resulted in very high density on heating from room temperature to desired temperatures (1500 - 2000 °C). Heating rates as high as 10^3-10^4 °C/min[67] were achieved. Wang et al. were able to sinter a wide variety of oxide ceramics in 10 sec by this UHS method. Different ceramics, such as fine grain Al_2O_3[68,69], ZrO_2[70], silicon nitride[74], MgO, $La_2Zr_2O_7$, $(La_{0.2}Nd_{0.2}Sm_{0.2}Eu_{0.2}Gd_{0.2})_2Zr_2O_7$, $SrTiO_3$[73], $BaTiO_3$[71], high entropy carbide[72], and various metals[75] have been sintered by this technique.

Our experimental UHS set-up is shown in Figure 3.2 a and discussed in Chapter-2.1.1. Table 3.1 summarizes both the measured and FEM simulated temperatures for the various the sintering cycles. In my sintering process of UHTC ZrB_2, an ultra-high heating rate of ~10^3 –10^4 ^oC/min was used. Sintering times of 10, 30 and 60 sec were selected. The densification and microstructural evolution were studied for these various sintering times. We believe that an ultra-high heating rate should suppress low-temperature grain coarsening and facilitate densification by lattice diffusion. We presume that an ultra-fast heating rate would mitigate grain boundary diffusion and grain growth, and enhance lattice diffusion and densification[111-113]. The power source was then switched off, and the samples cooled down within ~15 sec. The sintering profile is given in Figure c.

Table 3.1: UHS experiment sintering time, density, average particle/grain size, thermocouple temperature and FEM sintering temperature of all the sintering cycle.

Composition	Sintering time (sec)	Relative density (%)	Average particle/ grain size (μm)	Thermocouple temperature (^{o}C)	FEM temperature (^{o}C)
ZrB_2 powder	-	-	2.3 ± 1.3	-	-
UHS-ZrB_2	10	75%	2.7 ± 1.1	~2200	2600 ± 100 ^{o}C
	30	85%	6.8 ± 2.2		
	60	~90-93%	19.0 ± 8.4		

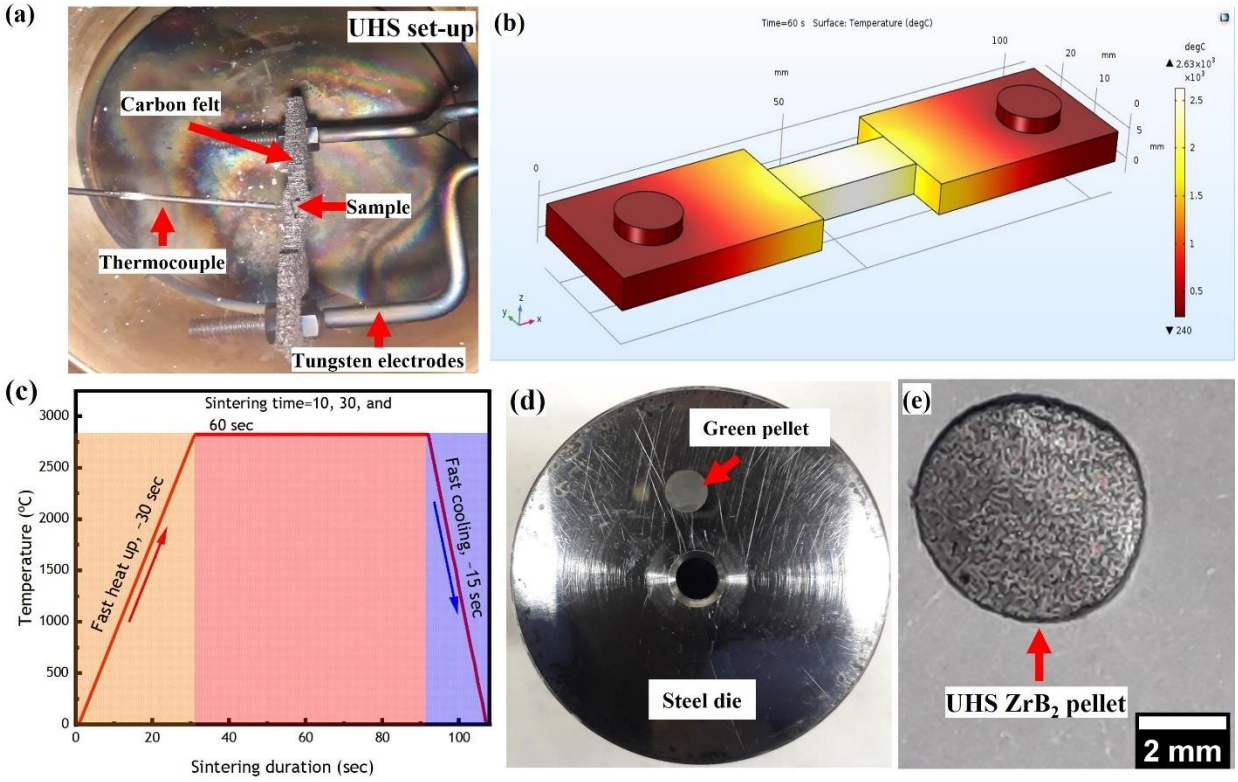

Figure 3.2: UHS system used: (a) UHS setup, carbon felt, and thermocouple; (b) Simulation of heat distribution in carbon felt; (c) Typical UHS sintering cycle; (d) Pressed green pellet and steel die; and (e) UHS sintered ZrB_2 pellet.

3.1.2. Finite element modeling and simulation

To determine the sintering temperature and the temperature distribution in the samples during UHS, an electromagnetic-joule heating model was built in the Finite Element Method (FEM) software COMSOL-5.3a. Figure b shows the simulated temperature profile after a 30 V DC voltage and a 50 Amp current were applied for 60 sec. The profile includes the tungsten electrodes, the carbon felt, and the ZrB_2 sample as shown in Figure a. The maximum temperature at the center was ~2630 °C. The simulation parameter for carbon felt was taken from the supplier website.

3.2. Results and Discussion

3.2.1. Density

The relative density results obtained from Archimedes testing are summarized in Table 3.1. The initial green densities were determined to be approximately 57 - 60% of theoretical values from the weight and dimensions of the pellets. The 60 second (sec) sintered samples (see Figure 3.2e) reached a high density of 90 - 93%, compared to 83% and 75% for 30 sec and 10 sec, respectively (see Figure 3.4 a-b). These density values are equal to or slightly lower than previously reported literature values for pure ZrB_2 under pressureless conditions with no sintering aids [51,53].

UHTC diborides of transition metals are often difficult to densify because of their strong covalent bond, high melting temperature, slow self-diffusion coefficient, and the presence of oxide impurities. Accordingly, sintering these borides requires a high sintering temperature, long dwell time for a pressureless method, and high pressure during pressure-assisted sintering. We sintered commercial ZrB_2 powders without milling (as received). Most previous studies using commercial ZrB_2 powders were refined (in ball, high-energy ball, shaker and attrition mills) to reduce the grain size and increase the surface area, both with/without sintering agents prior to densification [51-

58]. Milling impurities and smaller grain sizes can have an impact on diffusion kinetics, sintering temperature, and time. In the literature, the grain / particle size after milling has not always been reported. Therefore, a direct comparison of sintering time, sintering duration, final density, and final grain size of our UHS sintered ZrB_2 with previous reports was challenging.

For this investigation, we achieved a sintering cycle time of about 1 min and 45 sec for ZrB_2 to a relative density of 93%. This sintering cycle time is shorter than any prior reports, which can be seen by comparing our findings to prior sintering studies summarized in Table 1.3 of Chapter 1.

3.2.2. Structural studies

X-ray diffraction analysis of UHS ZrB_2 samples revealed a single-phase hexagonal crystal structure (see Figure 3.3) whose 2θ peaks matched with pure ZrB_2 (COD-1510856). The sharp peak and single-phase formation support the conclusion that a highly crystalline single-phase structure persists after UHS. Small peaks consistent with zirconium carbide (ZrC (COD-1011322)) and potential carbon-based or non-stoichiometric oxycarbide ZrC_xO_y phases—for example, supercubane, (COD-9012241) and ($Zr_6C_{136}O_{32}$ (COD-4329554), respectively, although the peaks at 2θ= ~29 ^{o} and ~38^o were too small to establish which—were also observed in the XRD peak of 60sec ZrB_2. These impurity phases might have been introduced from the carbon felt or the grinding process to remove the felt after sintering. Similar impurities have been reported in the literature when spark plasma sintering was used [114]. Ultra-fast sintering and subsequent cool down to room temperature did not affect the crystallinity or alter phase stability. The lattice parameters of the ZrB_2 sintered samples were reported to be ($a_{H,}$ c_H)$_=$ (3.136, c:3.470 Å), which are in good agreement with the expected values for pure ZrB_2 ($a_{H,}$ c_H)$_=$ (3.168, c:3.530 Å).

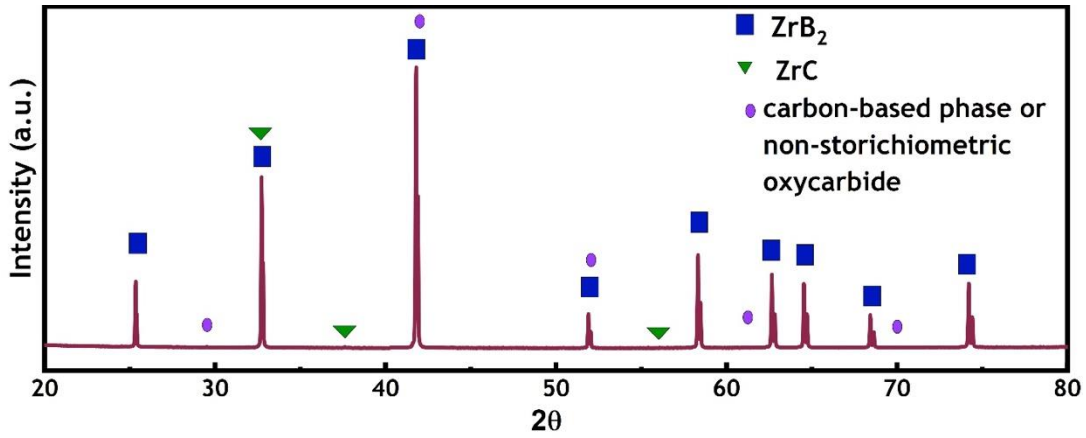

Figure 3.3: (a) XRD of UHS sintered ZrB_2 with the PDF card (COD-1510856).

3.2.3. Microstructure

Figure 3.4a-f shows the polished surfaces of ZrB_2 sintered for 10, 30 and 60 sec. The 10 sec sintered sample (Figure 3.4a, and d) retained what might appear to be an interconnected pore structure between round-shaped grains. The magnified image (Figure 3.4d) illustrates that the particles are sintered together at their contact points and some grain boundaries are well-formed, which signifies that the compact appears to have entered the intermediate stage of sintering. Image analysis revealed an average grain size of 2.7 µm ± 1.1 µm at 10 sec, which is close to the average particle size (2.3 µm ± 1.3 µm) for the starting powders. The results indicate that neck formation had begun between neighboring grains, but time was insufficient for grain boundary diffusion to reach higher degrees of densification.

After UHS sintering for 30 sec (see Figure 3.4b, and e), well-faceted grains were identified, and a relative density of 85% was measured for that sample. This resulted in a notable reduction in the residual porosity to 15 % from 25% (10 sec). Image analysis revealed an average grain size of 6.8 µm ± 2.2 µm. A longer densification time of 30 sec allowed diffusion to occur for extended duration, resulting in an increase of interparticle junction areas, as well as the beginning of pore elimination and grain growth. A higher magnification image (Figure 3.4e) revealed some

intergranular pores of about 2-3 μm in size. Some pore entrapments may have begun to occur, accompanying the grain coarsening process from 2.7 μm (10 sec) to 6.8 μm (30 sec).

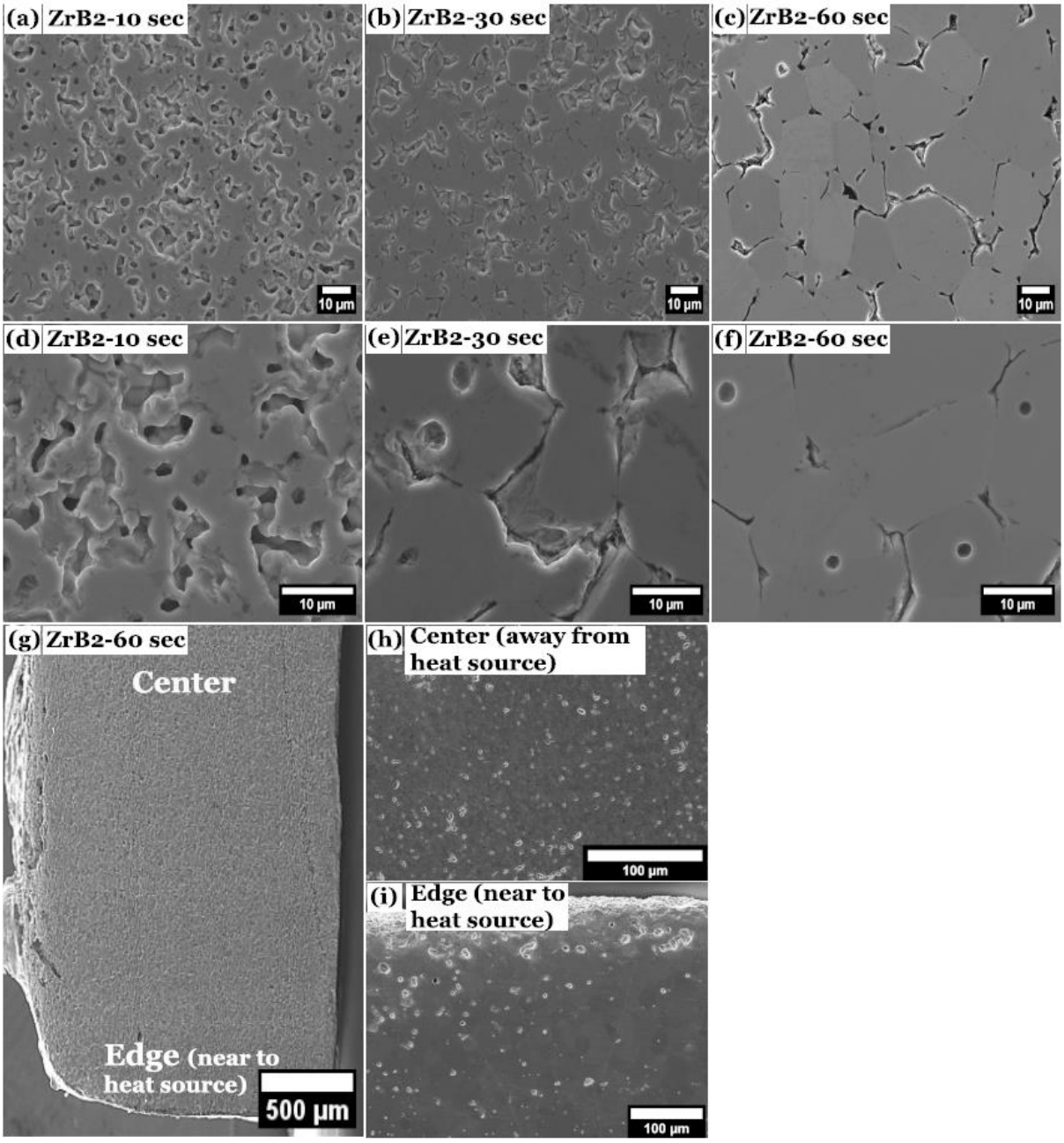

Figure 3.4: SEM image of polished surfaces at several magnifications of ZrB_2 samples sintered at 10 sec (a, d), 30 sec (b, e) and 60 sec (c, f). (g) Image of cross-section of UHS sintered ZrB_2,

showing areas (h) in the center of the samples, away from the heating source and (i) areas located at the edge portion of the sample, near the heat source.

After UHS sintering for 60 sec (see Figure 3.4c and f), much higher densities (93% relative density), larger grains, intergranular gap along grain boundary and few intergranular pores were found. In this image, well faceted rectangular-shaped grains of ~20-30 μm in sized are clearly evident. Grains appeared to be well-sintered to neighboring ones, and a denser microstructure with a substantial reduction of total porosity to 7% (from 15%) was observed. Image analysis revealed an average grain size of 19 μm ± 8.4 μm. A higher resolution magnified image (Figure 3.4f) shows large grains in the polished surface, with a few small pores (~1 μm) trapped within the grain and some space along the boundary and at the grain boundary triple point regions. The increase in UHS sintering time to 60 sec seems to have allowed for the final stage of densification to be reached, with only a small fraction of closed porosity remaining. These results are in good agreement with reported results in the literature for other sintering processes, such as pressureless sintering and spark plasma sintering [51,52,57].

Figure 3.4g-i indicate wider areas of the microstructures of the sintered ZrB_2 prepared with 60 sec sintering time, showing regions at the center of the sample away from the heat source (h), and at the edge of the sample close to the heat source (i). These images all exhibit a relatively homogeneous microstructure, indicating that there were no significant hot spots during the experiments across the sample throughout the lengths of roughly 1 mm, with just a few examples of porosity consistent with the density measured by Archimedes and some grain pullout from polishing.

During sintering, surface diffusion and grain boundary/ lattice diffusion occur concurrently. Densification is slowed by surface diffusion, which causes grain coarsening and reduces the

driving force of densification [34]. At higher temperatures above 2100 ^{o}C, Lonergan et al. showed that densification of ZrB_2 was accelerated, requiring less time to achieve the desired densities [35]. Here, UHS sintering at ~2600 ^{o}C facilitated mitigation of surface diffusion, and the production of highly dense ZrB_2 samples from a powder compact within a very short sintering time of 60 sec.

Next, we compared our final grain sizes for sintered ZrB_2 (summarized in Table 1.3) with prior published findings. We sintered commercial ZrB_2 powders in the as-received condition without any further milling. Note that prior studies of commercial ZrB_2 powders were given additional milling steps to reduce the particle size before sintering [51-58], both with and without sintering additives. Additional milling processes can impart inclusions in pure ZrB_2 powders that can affect densification kinetics, grain growth, and sintering temperature. Furthermore, the grain size after milling was not always reported in those prior investigations. Thus, we must use caution in comparing our initial-to-final grain size (coarsening) and densification changes to those of these prior studies.

A concise summary of prior common sintering techniques of ZrB_2 powders was provided in Table 1.3 in Chapter 1. Since the particle size after milling was not always available, we listed the initial particle size of the as-received powders, unless specifically stated. Chamberlain et al. [51] densified ZrB_2 to 98% density via pressure-less sintering at a temperature of 2150 °C for 9 hours. The average grain size increased from 2 μm to 9.1 μm ± 5.6 μm, with some exaggerated grain growth to a maximum grain size of about 30μm. Coarsening resulted in an increase in the average grain size by a factor of about 4.5x. Rocha et al. [52] densified ZrB_2-SiC composites to ~93% density by pressure-less sintering at 2050 °C for 1 hour. The powders were first milled to about 1.5 μm in size, and the final grain size was 16μm. Sintering resulted in a 10x increase in particle size. Similarly, Leo et al. [53] reported an increase from 12.4 μm+3.4 μm from 2.3 μm,

using pressure-less sintering on milled ZrB_2 sintered at 2100 °C for 1 hour. Spark plasma sintering (SPS) was reported by Zamora et al. [54] to result in a dramatic increase in grain size by 100x, beginning with 10 nm powders and ending with a final particle size of 1.5 µm. The small particle size allowed for lower sintering temperatures of 1600-2000 °C, yielding densities of 96-98.5%. Other researchers have reported achieving densities of 99.9% by SPS densification of ZrB2-25 mol% SiC at 1900 °C for 7 minutes, with final grain sizes of 5.2 µm beginning from <1 µm. Hot-pressed ZrB_2 was studied by Chamberlain et al. [57] under a load of 32 MPa at a temperature of 1900 °C for 45min. A final density of 99.9% was achieved with an average grain size of 6 µm, starting with an initial size of 2 µm.

In all these prior investigations, the total sintering time was significantly longer than that for our UHS technique. Additionally, an additional milling step was not required in our process. Furthermore, UHS sintering did not result in as large percentage of particle coarsening compared to other prior studies. The rapid heating rate and short sixty second isothermal soak offers a unique approach to an energy efficient and cost-effective method by which to fabricate technical grade ZrB_2.

3.2.4. Elemental analysis

Elemental analysis of fracture surface SEM images for UHS ZrB_2 sintered for 60 sec are provided in Figure a-c. The EDS data demonstrate a homogeneous distribution of Zr and B elements, without any notable phase segregation or compositional nonuniformity. These results clearly dispel any concerns about elemental clustering / segregation.

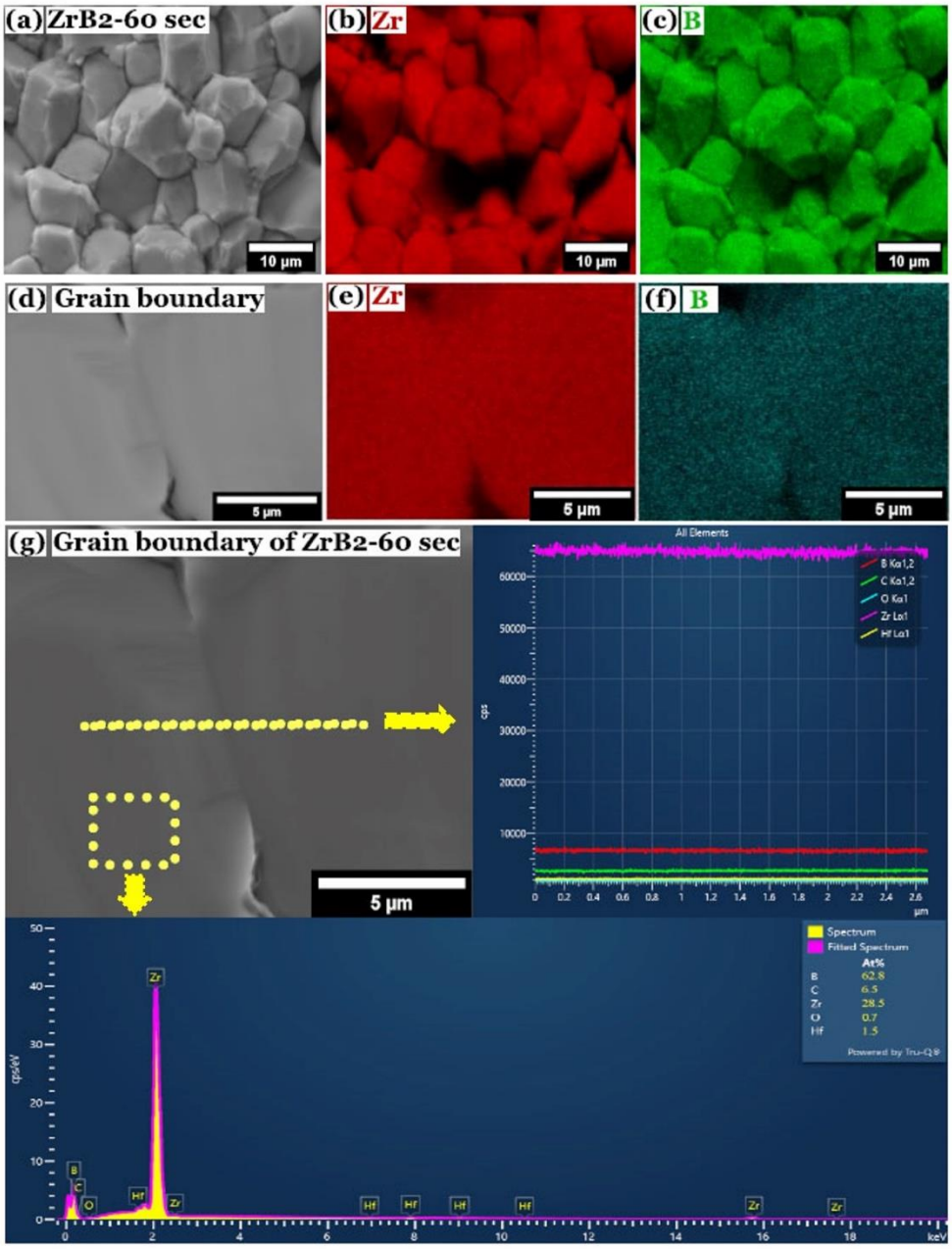

Figure 3.5. EDS analysis of 60 sec UHS ZrB_2 fracture surface SEM image. (a) SEM image, (b) Zr elemental scan, and (c) B elemental scan. EDS elemental mapping on grain boundary: (d) secondary electron image, (e) Zr elemental scan, and (f) B elemental scans show no indication of clustering of Zr and B on the grain boundary regions. (g) backscattered electron image and EDS line scanning on grain boundary show compositional uniformity, and EDS point scan shows compositional analysis of UHS sintered ZrB_2.

To further investigate the compositional homogeneity and elemental composition of UHS sintered ZrB_2, backscattered microscopy, EDS mapping, and line scanning analysis were performed on the grain boundary regions at higher magnification, as shown in Figure 3.5d-g. Both the SEM backscattered image and EDS maps of the grain boundary region showed no evidence of compositional nonuniformity. Additionally, the EDS line scan of the 9 μm length segment along grain boundaries revealed no compositional variations. Further, EDS point analysis indicated a low level of impurity oxygen (0.7 atom %) and carbon (6.5 atom %) present in the sintered body. This impurity might have resulted from material processing, residue from the carbon elements used in sintering steps, and/or sample mounting for SEM analysis. Overall, these findings conclusively show that UHS sintering does not result in compositional changes or nonuniformity for the selected composition studied; neither are there any significant changes between grains or along grain boundaries.

3.2.5. Ultra-fast high temperature sintering mechanism

Sintering is a complex mass transfer phenomenon, which involves different concurrent diffusion mechanisms, such as surface (grain boundary) and bulk (lattice) diffusion. In the initial and intermediate stages of sintering, surface diffusion is favorable at low temperature as it has a lower activation energy, and it causes particle coarsening and reduces the driving force of densification [34]. On the other hand, bulk diffusion enhances densification, and it is favored by sintering at higher temperatures, because it has a high activation energy. A slow heating rate is thus favorable for surface diffusion and, accordingly, particle coarsening.

Thus, to achieve a higher density, it is crucial to sinter a material at or above its transition temperature from surface to grain boundary diffusion, T_{GBD}. Prior studies summarized in Table 1.3 showed that densification did not significantly increase until reaching sintering temperatures

of about 2000-2200 °C. For example, Lonergan et al. [35] densified ZrB_2 to 99.7% density via reaction hot pressing at 2100 °C for 2 hours. They found between 1800-2000 °C, the density increased by 3% for every 100 °C increase in sintering temperature, and that between 2000-2050 °C, the density increased by 3% for every 50 °C increase. Lonergan et al. also noted that at 2100 °C, the bulk diffusion coefficient was higher than the analogous surface measurement. From these prior experimental studies, it can be inferred that T_{GBD} is about 2050-2100 °C.

For the UHS method reported in this manuscript, the sintering temperature was estimated to be significantly higher (2630^{o}C, see Figure 3.2b) than the T_{GBD} of ZrB_2, and closer to (but below) the melting temperature of ZrB_2 (T_m= 3425^{o}C) [5,51]. No evidence of melting and recrystallization, glassy phases, or decomposition was observed in the SEM images (Figure 4). Furthermore, the heat-up time to the estimated temperature of 2630 ^{o}C was only ~30 seconds, which is notably faster (10^3-10^4 ^{o}C/min) than reported in prior studies (300 ^{o}C/min) [41]. These results indicate that UHS sintering at temperatures significantly greater than T_{GBD}—and close to but below T_m for just seconds—may yield the best sintering conditions by which to favor lattice diffusion over surface diffusion, and without incurring any significant grain growth, melting or recrystallization. A detailed study will be conducted in the future to understand the densification mechanism in UHS.

3.2.6. Mechanical properties

Characteristic load-displacement curves of our UHS sintered ZrB_2 obtained by nano-indentation are shown in Figure 3.6. The load curves were found to be smooth, except that a few graphs exhibited strain bursts (pop-ins phenomenon) at 200 mN load between different loading and unloading cycles. The observed strain bursts are typical of polycrystalline ZrB_2, as previously reported [115-117]. The probable reason for the pop-in is when shear stress on the slip systems

results in a semi-plastic behavior of ZrB_2 on the nanoscale, specifically on the basal planes[115-117].

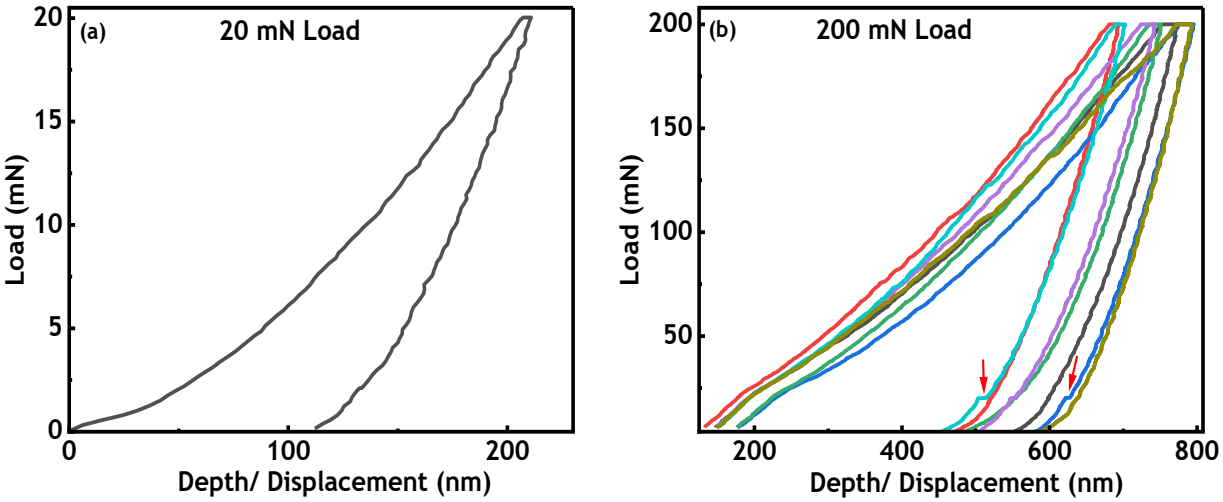

Figure 3.6: Load-displacement curves obtained by nanoindentation under a load of (a) 20 mN and (b) 200 mN. In, (b) multiple cycle represents the load-displacement behavior under 200 mN, where some of the curves exhibit pop-in behavior as marked with red arrow.

Hardness and elastic modulus data are provided in

Figure 3.7. The average hardness value was 19.1 GPa under a 200 mN load. The hardness value increased with lower indentation load of 20mN to about 30 GPa. The average elastic modulus was 373.3 GPa under 200 mN load, which increased to 412 GPa under 20 mN.

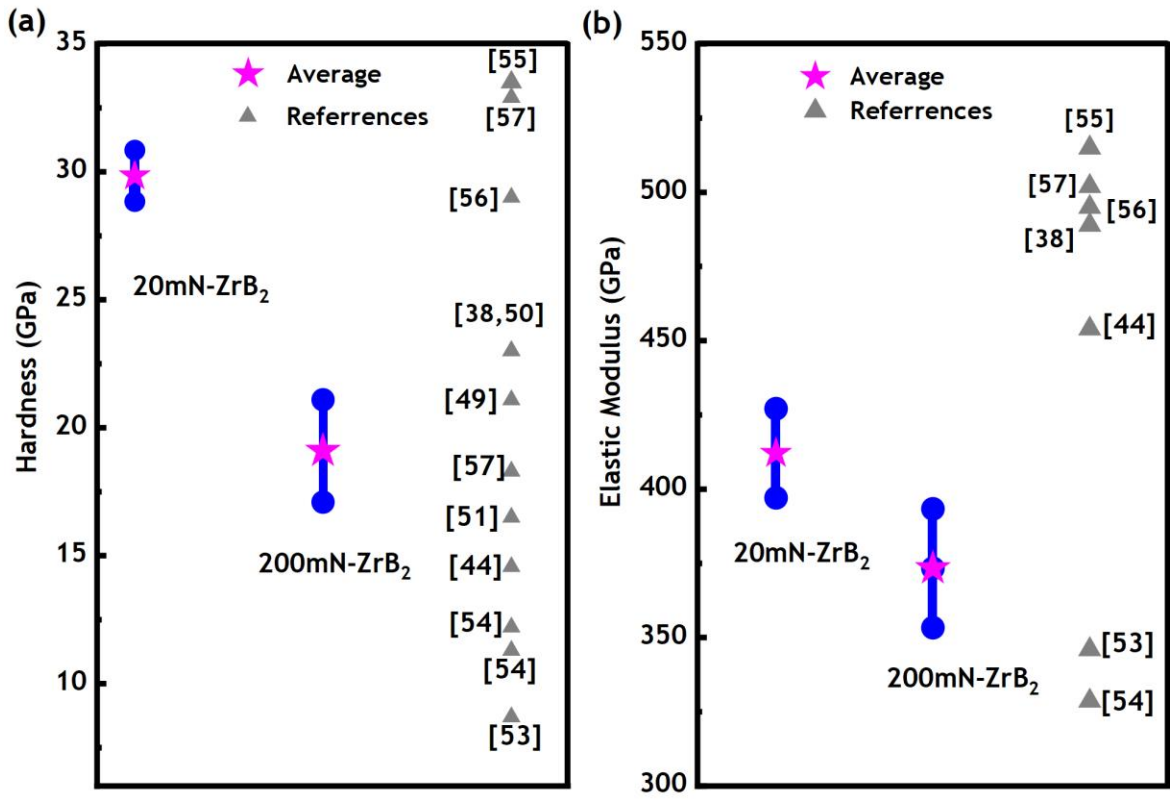

Figure 3.7. Comparison of hardness and elastic modulus of UHS ZrB_2 and previous literature results. All the UHS ZrB_2 samples were sintered in 60 sec.

The hardness and elastic modulus values of our UHS sintered ZrB_2 were found to be consistent with previously reported typical values of sintered ZrB_2 (with and without additives) of between 8 - 33 GPa (hardness) and 300 - 500 GPa (elastic modulus) at room temperature [51,57,118-128], as shown in Figure for comparison. A summary of previous hardness and elastic modulus studies are also shown in

Table 2.2. The wide scattering in the data can likely be attributed to differences in measurement parameters, processing routes, and dopants which causes different grain sizes, morphologies, and porosities in the final state. Typically, the strength of diborides increases with

decreasing grain size. Our findings show that the UHS method is not detrimental to the mechanical performance of ZrB_2.

Table 2.*2*: A summary of previous literature on ZrB_2 hardness and elastic modulus.

Hardness by Vickers' hardness (VH) / Nanoindentation (NI)	Load	Hardness (GPa)	Elastic modulus (GPa)	Reference
VH	1 N	14.57±2.6	454	[51]
VH	1 kg	23.0±0.9	489	[57]
NI	2.5 mN	32.9 ± 0.7	502 ± 17	[127]
VH	2 N	18.3 ± 1.2	-	[127]
NI	2.5 mN	32.9 ± 0.7	502 ± 17	[127]
NI	8 mN	29 ± 2	495 ± 43	[126]
NI	10 mN	33.5± 2.7	515± 38	[125]
NI	400 mN	12.21	328.7	[124]
VH	5 kg	11.3	-	[124]
VH	1 kg	8.7±0.4	346	[123]
VH	9.81 N	16.5 ± 0.9	-	[121]
VH	0.098 N	23 ± 2	-	[120]
VH	200 gf	21.09 ± 1.3	-	[119]

3.2.7. Oxidation testing

Oxidation testing (TGA) from room temperature to 1100 ^oC in air for 60 sec UHS ZrB_2 is given in Figure . The measured maximum weight gain during TGA in air after a one hour holding time at 1100 ^oC was found to be 1.41% for ZrB_2 (calculated weight gain should be ~9.18% on complete oxidation). During isothermal oxidation at 1100 ^oC for one hour, the weight gain was ~0.57%, which is similar to that previously reported [129]. Oxidation weight gain started on heating at 790 ^oC as shown in Figure a. Expected oxidation reactions for ZrB_2 are given in Eq-3.1 and 3.2.

$$ZrB_2 + 5/2\ O_2 = ZrO_2 + B_2O_3 \quad (3.1)$$

$$B_2O_3\ (l) = B_2O_3\ (g) \quad (3.22)$$

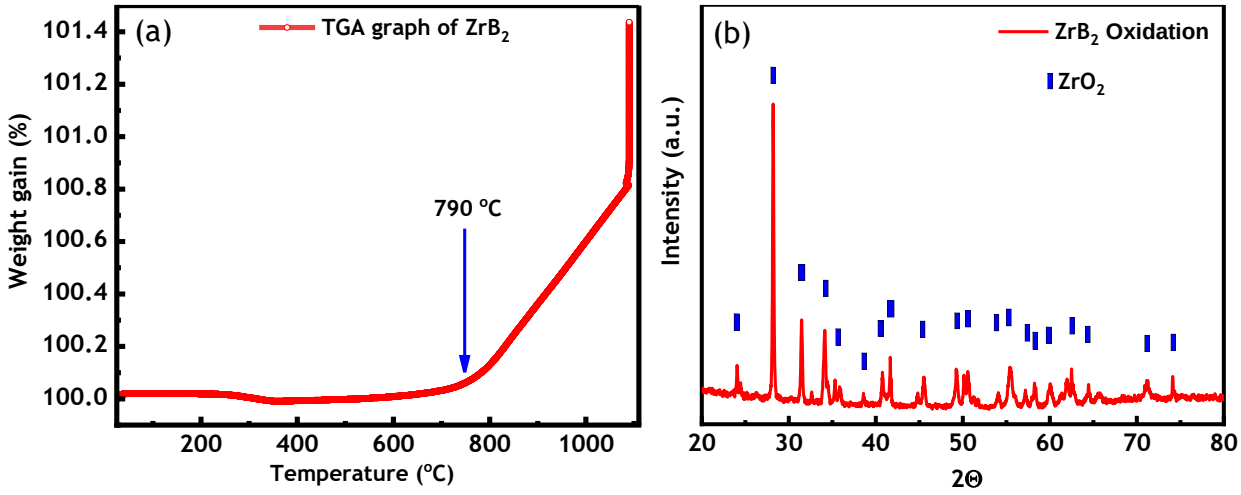

Figure 3.8. (a) Oxidation of 60 sec sintered UHS ZrB_2 in air on heating from room temperature to 1100 ^oC. (b) XRD analysis of all there UHS borides oxidation surfaces.

According to prior literature reports, mass gain and loss can occur simultaneously depending at the reaction temperature [130,131]. Mass gain can occur due to the formation of ZrO_2 and B_2O_3 from ZrB_2, a mass loss can occur due to the evaporation of the B_2O_3 liquid at and above 1100 ^oC. XRD analysis of the oxidation surface of UHS ZrB_2 is shown in Figure b. The oxidation product of ZrB_2 is ZrO_2 (COD database 9007485). The SEM image of the oxidation surface of ZrB_2 after oxidation testing revealed a small amount of very fine grain formation on the surface, as shown in Figure 3.9 a and b. Higher magnification of the surface revealed a fine thread-like morphology with some small pores. From XRD and SEM analysis, it can be inferred that the weight gain represents the combined effect of mass gain due to metal oxide formation and weight loss due to vaporization of the newly formed boron compounds, according to Eq-3.1 and 3.2. However, due to a very thin layer of ZrO_2, no evidence of B_2O_3 in the XRD scan was found (Figure

b). Overall, TGA analysis shows that our ZrB_2 displays good oxidation resistance. The oxidation curve and oxidation weight gain data were found to be consistent with previously reported results, indicating that the UHS sintering process is not detrimental to the performance of ZrB_2.

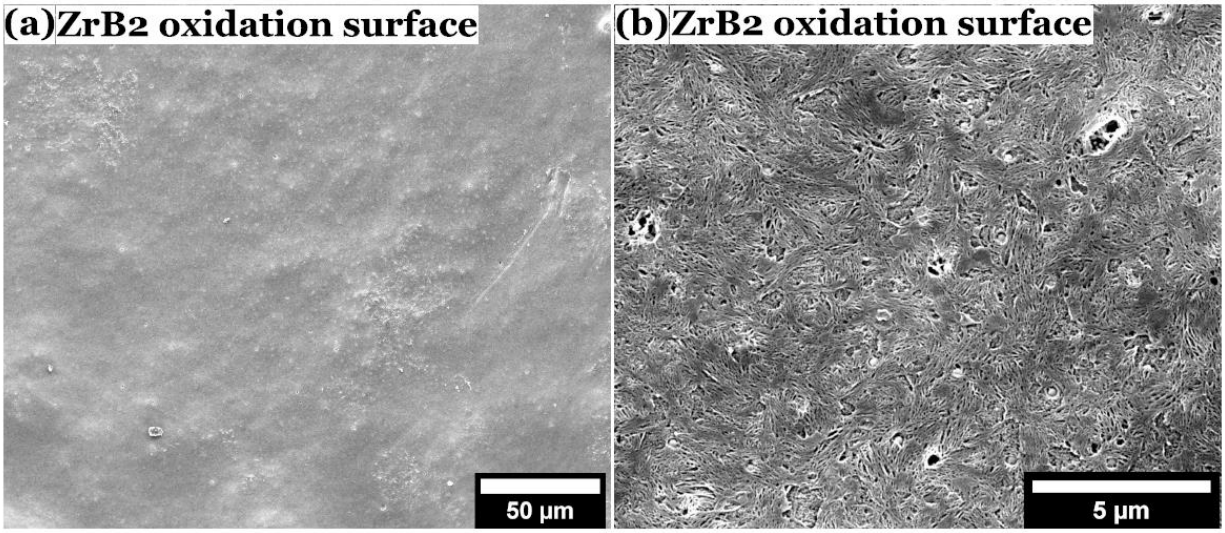

Figure 3.9: (a) SEM microstructure of the oxidized surface of ZrB_2 after 1 h holding at 1100 ^oC. (b) Enlarge image of a, which shows fine thread-like structures of an oxidation surface for ZrB_2.

3.3. Conclusion

In the present work, the sintering behavior of ZrB_2 was investigated via UHS. Electrical power was utilized to directly heat a green ZrB_2 pellet within carbon felt at a heating rate up to 10^4 ^oC/ min, densities of > 90% theoretical were obtained in 60 sec using a vacuum atmosphere. The time-dependent microstructural evolution was also studied. After 10 sec we observed the onset of inter-particle neck formation, after which particles began to agglomerate. With increasing sintering time to 30 sec, neck region growth continued, and the number of pores was reduced. After 60 sec, highly dense microstructures were found with a small volume fraction of ~1-2 µm sized pores. The relative sintered density and grain size increased with sintering time, from 75% and 2.7 ± 1.1µm

at 10sec to 93% and 19.0 ± 8.4 μm after 60sec. XRD analysis confirmed a crystallinity and phase stability of ZrB_2 after UHS sintering. The mechanism underlying UHS is based on the sudden increase of the temperature above T_{GBD} to a value closer to T_m. This process facilitates the attainment of high densities within seconds, and without 2^{nd} phase formation or melting-recrystallization. EDS elemental mapping and line scanning showed a homogeneous distribution of Zr and B within the grains and along the grain boundary regions. Hardness and elastic modulus by nanoindentation were measured, revealing good mechanical properties. Oxidation testing at 1100 ^oC in air showed a high oxidation resistance of ZrB_2. Our research has confirmed that high quality UHTC ceramics can be obtained by UHS.

CHAPTER İV. MULTICOMPONENT HEXABORIDES WITH LOW WORK FUNCTIONS BY ULTRA-FAST HIGH TEMPERATURE SINTERING

This research was published in Open Ceramics in 2023. Reference: Santanu Mondal, Advaith V. Rau, Kathy Lu, Jie-Fang Li, Dwight Viehland. (2023). "Multicomponent hexaborides with low work functions by ultra-fast high temperature sintering." Open Ceramics. https://doi.org/10.1016/j.oceram.2023.100479.

A reduction of the work function (W_f) in multicomponent hexaborides was achieved by doping with highly electropositive Ba, which enhances electron emission. Single-phase bulk multicomponent polycrystalline hexaborides of $La_{0.5}Ba_{0.5}B_6$, $Ce_{0.5}Ba_{0.5}B_6$, and BaB_6 powders were first synthesized and then densified by ultra-fast high temperature sintering. Using a total reaction and densification time of 6 min, a density of ~90% theoretical was reached.

W_f can be measured by photoelectron spectroscopy (PES), electron beam induced current (EBIC), thermionic emission (TE), and Kelvin probe force microscopy (KPFM). In particular, the KPFM method has higher spatial resolution and energy sensitivity in comparison to the others. KPFM was used to measure the contact potential difference (CPD) between the sample surface and the AFM tip. First, the topography was determined in a tapping mode, after which the surface potential (V_{CPD}) was measured by keeping a fixed distance between the sample and AFM tip in a non-contact mode. When an AFM tip approaches the sample surface, an electrical force is formed between the tip (ϕ_{tip}) and sample (ϕ_{sample}) surface due to their Fermi energy difference. The work function (W_f) can be given as [132],

$$V_{CPD} = \frac{\phi_{tip} - \phi_{sample}}{-q}; \quad (4.2)$$

where, q = 1. 602 × 10^{-19}C is the fundamental electric charge.

Here, $Ce_{(1-X)}Ba_XB_6$ and $La_{(1-X)}Ba_XB_6$ metal hexaboride solid solutions were synthesized by solid state reaction and densified in 6 minutes using UHS. The UHS approach makes it easier to produce dense bulk hexaboride ceramics quickly and efficiently while reducing the impact of barium's high volatility [133]. W_f measurements were obtained by KMPF, yielding values of W_f = 2.05±0.1 and 2.0±0.1 for $La_{0.5}Ba_{0.5}B_6$ and $Ce_{0.5}Ba_{0.5}B_6$ respectively. These W_f values were found to be similar to those predicted by first-principles calculations. Ba-substitution was confirmed to be an effective approach for reducing W_f (~25%) in various multicomponent hexaborides.

4.1. Experimental

4.1.1. The starting materials and process parameters

BaB_6 was prepared by reacting $BaCO_3$ (Alfa Aesar, 99 wt% purity), B_4C (Alfa Aesar, 99+% purity, particle size <10μm), and graphite powder (Thermo Scientific, 99 % purity, particle size 7-11 μm) in a 2:3:1 molar ratio. $La_{0.5}Ba_{0.5}B_6$ and $Ce_{0.5}Ba_{0.5}B_6$ were produced by reacting equimolar portions of BaB_6 and LaB_6 (Stanford Advanced Materials, 99% purity), and BaB_6 and CeB_6 (Stanford Advanced Materials, 99% purity), respectively. Stoichiometric amounts of these starting ingredients were weighed (in a 10 g batch) and ball milled (planetary ball mill) for 3 hour in a stainless-steel jar with zirconia media in ethanol. After milling, 0.2 wt% polyvinyl alcohol (Acros organics, 88% hydrolyzed, average M.W. 88000) and 0.2 wt% citric acid (Alfa Aesar, 99+% purity) were added to the powder mixture slurry and stirred for 5 min at 300 rpm. The slurry was then dried at 80 °C. The dried powder was ground in a mortar pestle and pelletized using a uniaxial press under 135 MPa. The pellet size was 5mm in diameter and 1-2mm in thickness. The resulting green pellets were then sintered by UHS in vacuum for a 3 min dwell time at multiple reaction temperatures depending on the compositions mentioned (see Table 4.1).

4.1.2. Densification of $Ce_{0.5}Ba_{0.5}B_6$, $La_{0.5}Ba_{0.5}B_6$, and BaB_6, via UHS

The synthesized powder was ground in an alumina mortar for 5 min and then re-pelletized using a uniaxial press under 135 MPa pressure. The pellet size was 5mm diameter and 1-2mm in thickness. The resulting pellets were then densified by UHS in vacuum for a 3 min dwell time at multiple reaction temperatures, again as summarized in Table 4.1.

Table 4.1. Summary of compositions and process parameters

		Composition		
		A: BaB_6	B: $La_{0.5}Ba_{0.5}B_6$	C: $Ce_{0.5}Ba_{0.5}B_6$
Firing temperature (°C)	Synthesis (1st sintering)	1300	1700	1700
		1400	1800	1800
		1500	2100	2100
		1600	-	-
	Densification (2nd sintering)	**1900**	**2200**	**2200**
Time (sec)	Synthesis	180	180	180
	Densification	180	180	180

4.1.3. UHS

Figure 4.1a depicts a typical layout of our UHS setup. The pressed precursor pellets were sandwiched between a carbon felt that served as a resistive heating source. A cavity was made on the side of the carbon felt so that the green pellet could be inserted into it for sintering, as shown in Figure 4.1a. The detail UHS setup is provided in Section 2.1.1.

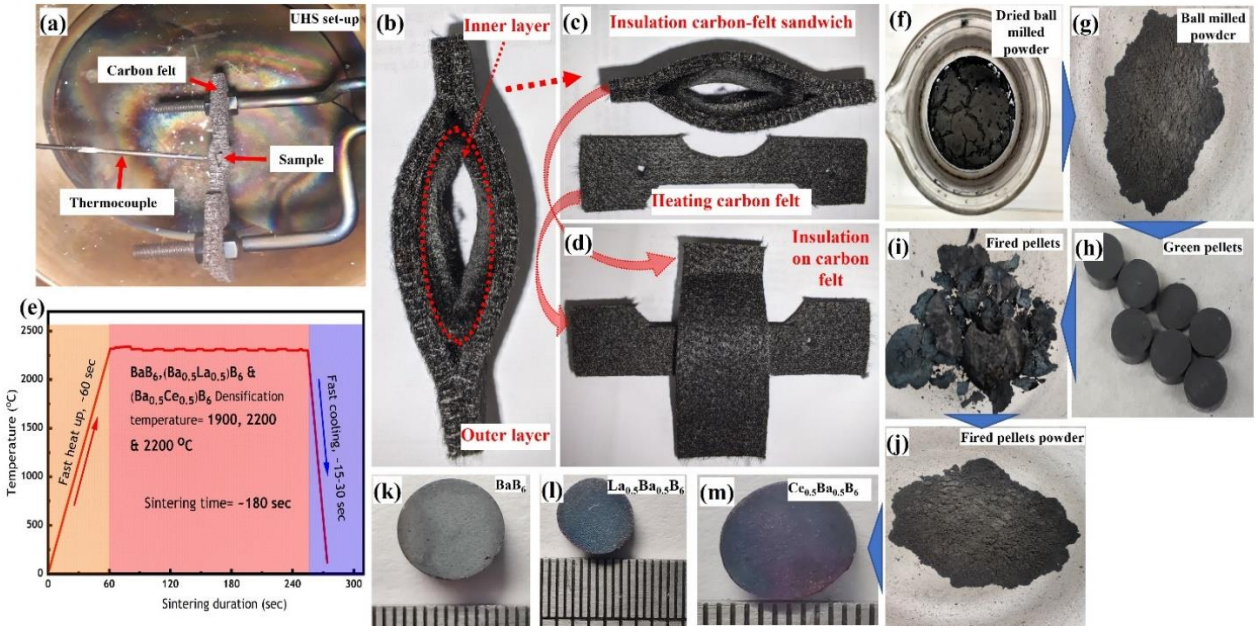

Figure 4.1. UHS system used (a) UHS setup, carbon felt, and thermocouple; (b-d) insulation layer of carbon felt sandwich assemble; (e) typical UHS sintering cycle; (f) dried ball-milled powder in a beaker; (g) grounded ball-milled powder; (h) pressed green pellet; (i) heat treated before UHS (synthesized pellet); (j) grounded powder of sintered pellet; UHS sintered (k) BaB_6, (l) $La_{0.5}Ba_{0.5}B_6$, and (m) $Ce_{0.5}Ba_{0.5}B_6$ pellet.

A significant percentage of the heat generated in the carbon felt during UHS sintering was lost through radiation toward the surroundings and not utilized. As a result, the entire sintering process became less energy efficient. Some previously reported UHS and other sintering techniques have also indicated a similar issue, which can be mitigated by utilizing appropriate thermal insulation [70,103]. Thus, for this investigation, a second layer of carbon felt serving as thermal insulation was placed on the center portion of the main heating carbon felt and sample assembly, as shown in Figures 4.1b-d.

Using a programmable DC electrical power supply, a ramp-up current was used to heat the carbon felt to the reaction and sintering temperature range of 1300 to 2200 °C (0 - 35V, 0 - 61 A, Agilent 6673). For hexaboride synthesis and sintering, an ultra-high heating rate of ~10^3 –10^4 ^oC/min was used. A sintering times of 3 min was selected. The phase formation, densification, work function, and microstructural evolution were studied for the synthesized hexaboride materials.

4.2. Results and Discussion

4.2.1. XRD

Figure 4.2 shows XRD scans of BaB_6, $Ce_{0.5}Ba_{0.5}B_6$, and $La_{0.5}Ba_{0.5}B_6$ synthesized via UHS in 3 min at 1500, 2100, and 2100 °C respectively. The XRD patterns reveal highly crystalline (sharp) peaks and lack of any secondary impurity phases. Analysis of the peaks yielded a single cubic phase with a lattice parameter of a_c= 4.2621(4), 4.1945(4), and 4.2119(7) Å for BaB_6, $Ce_{0.5}Ba_{0.5}B_6$, and $La_{0.5}Ba_{0.5}B_6$, respectively. The X-ray peak position and lattice parameters were found to be similar to powder diffraction file (PDF) cards for BaB_6 (00-034-0367) and $La_{0.5}Ba_{0.5}B_6$ (01-087-7551). Since barium, cerium, and lanthanum hexaborides have a cubic crystal structure (CsCl-type unit cell) and similar lattice parameter (4.261, 4.1569, and 4.1407Å for BaB_6, LaB_6, and CeB_6 respectively), they can form a complete solid solution. Based on the lattice parameters of the individual hexaborides, the calculated lattice parameter values for $Ce_{0.5}Ba_{0.5}B_6$ and $La_{0.5}Ba_{0.5}B_6$ (by Vegard's law [134-136]) should be 4.201 and 4.209, respectively; in contrast, the measured values were found to be 4.1945(4) and 4.2119(7) Å for $Ce_{0.5}Ba_{0.5}B_6$ and $La_{0.5}Ba_{0.5}B_6$, respectively. Assuming the theory of Vegard's law, the results indicate that the actual compositions are about $Ce_{0.55}Ba_{0.45}B_6$ and $La_{0.48}Ba_{0.52}B_6$. Thus, for the remainder of this paper, we refer to the compositions as $Ce_{0.5}Ba_{0.5}B_6$ and $La_{0.5}Ba_{0.5}B_6$ (rather than $Ce_{0.55}Ba_{0.45}B_6$ and $La_{0.48}Ba_{0.52}B_6$).

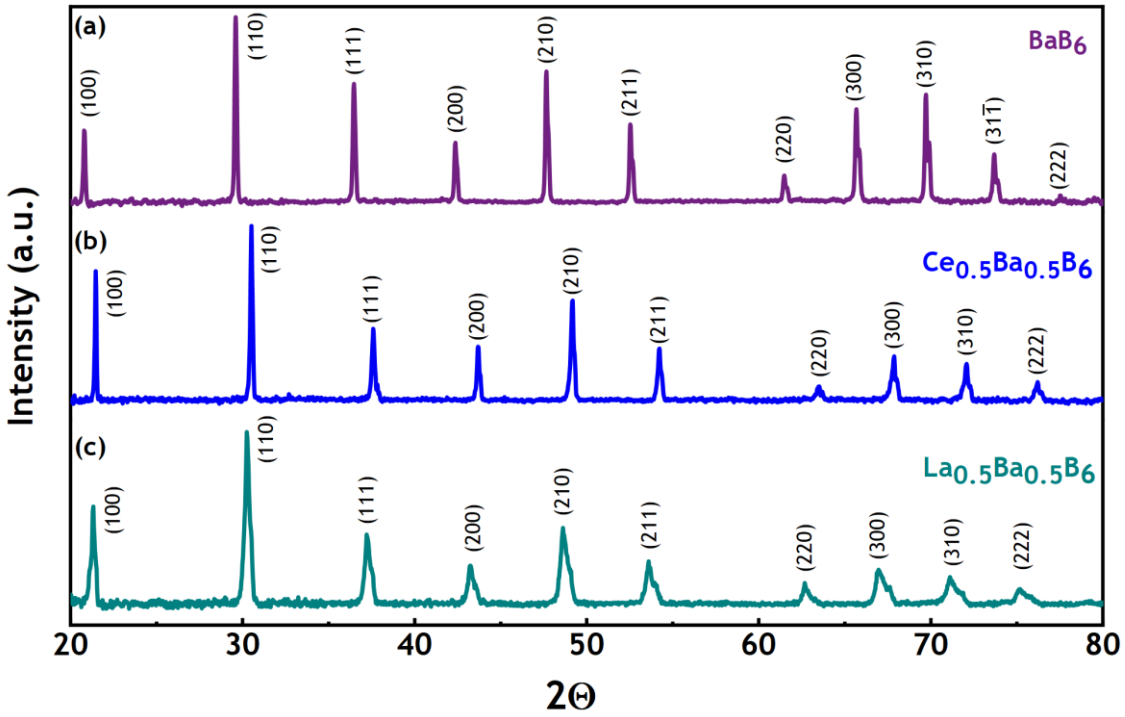

Figure 4.2. XRD scans of UHS sintered BaB_6, $Ce_{0.5}Ba_{0.5}B_6$, and $La_{0.5}Ba_{0.5}B_6$. All three synthesized hexaboride compositions were found to be crystalline and single phase**.**

The formation of a solid solution via reaction synthesis depends on two crucial experimental parameters: milling time and reaction temperature. To determine optimum reaction temperatures, pellets of ball milled powders were sintered (i.e., synthesized/ 1st sintering) at different temperatures, as summarized in Table 4.1. Phase pure BaB_6 was formed at /above a synthesis temperature of 1500 °C (Figure 4.3a). Lower temperatures (1300 and 1400 °C) resulted in additional peaks (marked with blue arrows), indicating incomplete reaction and secondary minor phases. An enlarged scan around a single peak ($29.4<2\theta<29.8°$) reveals the presence of peak splitting and skewing, as shown in the inset of Figure 4.3a. Previous synthesis studies of BaB_6 reported an optimal reaction temperature of 1400 °C using a 2 hour reaction time, via both vacuum sintering and hot-pressing methods [137,138]. Here, using UHS, a 100 °C higher temperature was found to reduce the reaction time to 3 minutes.

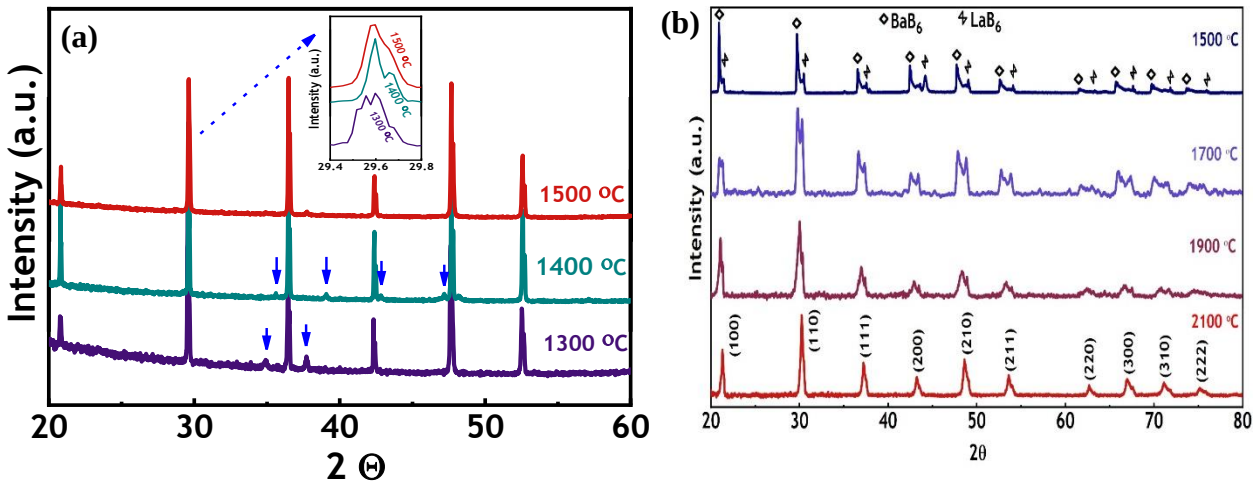

Figure 4.3. XRD scans of UHS sintered (a) BaB_6, and (b) $La_{0.5}Ba_{0.5}B_6$ at different temperatures. The effect of reduction temperature on phase formation of BaB_6 and on solid solution formation of $La_{0.5}Ba_{0.5}B_6$ can be seen.

Complete solid solution formation of BaB_6-LaB_6 and BaB_6-CeB_6 was found to occur at a reaction temperature of 2100 °C, as can be seen in the XRD scans in Figure 4.3b. At low reaction temperatures, separate peaks for BaB_6 and LaB_6 were clearly distinguishable (as marked in Figure 4.3b). Single phase formation occurred at a higher reaction temperature of 2100 °C. Previous synthesis studies reported a reaction temperature of 1950 °C and reaction time of one hour, via multiple step SPS sintering cycle (that had a time of > 1 day) [29]. Again, a single-step reaction at 2100 °C via UHS required a reaction time of only 3 minutes.

4.4.2. Density

The density of BaB_6, $La_{0.5}Ba_{0.5}B_6$, and $Ce_{0.5}Ba_{0.5}B_6$ sintered at 1900, 2200 and 2200 °C were approximately 82, 89, and 94% of the theoretical value, respectively. Further increases in the sintering time did not reveal any enhanced effect on densification, but rather showed increased Ba

volatilization. A prior report of LaB_6-BaB_6 densified by SPS method yielded a density of 59% [29]. There are no prior reports of the densification of BaB_6 and $Ce_{0.5}Ba_{0.5}B_6$ by UHS.

4.4.3. SEM

SEM images of all the various hexaborides synthesized at their optimum UHS reaction temperatures are shown in Figure 4.4. The SEM images for BaB_6 (1500 °C), $La_{0.5}Ba_{0.5}B_6$ (2100 °C), and $Ce_{0.5}Ba_{0.5}B_6$ (2100 °C) are shown in Figures 4.4a-c, respectively. Comparing these data to XRD scans (see Figure 4.3) demonstrate the formation of well-faceted grains that have a single cubic phase.

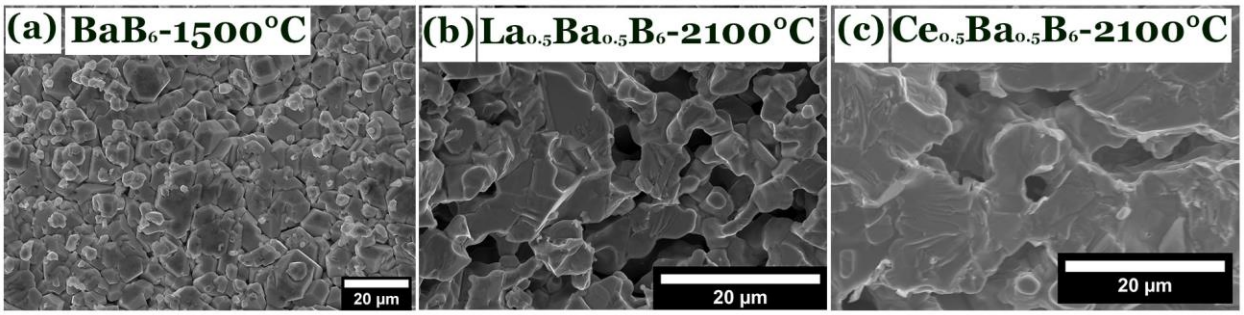

Figure 4.4. SEM images after reaction synthesis (1st firing) of BaB_6 (1500 °C), $La_{0.5}Ba_{0.5}B_6$ (2100 °C), and $Ce_{0.5}Ba_{0.5}B_6$ (2100 °C) at the optimum UHS reaction temperature.

Additionally, a series of reactions was conducted at various temperatures to identify the optimum reaction temperature; a selection of the resulting data is provided in Figure 4.5 for BaB_6, and in Figure 4.6 for $La_{0.5}Ba_{0.5}B_6$ and $Ce_{0.5}Ba_{0.5}B_6$. Specifically, Figure 4.5 shows the SEM images of various BaB_6 samples synthesized at four different reaction temperatures: 1300, 1400, 1500, and 1600 ^oC. Both low and high magnification (inset) images are provided to show the morphology of a larger area and detailed grain information. Note that the sample synthesized at 1300 ^oC was porous and consisted of fine grains (~3 - 5 µm), without forming grain facets (Figure 4.5a and e). Increasing the synthesis temperature to 1400 ^oC (Figure 4.5b) resulted in an increase of grain size

to 5 - 7 µm, and the development of distinct cubic shaped grains (Figure 4.5f). Some clusters of smaller grains can be also seen among the cubic-shaped grains (Figure 4.5g). A short synthesis duration (3 minutes) and faster cooling time (15 seconds) were inadequate to achieve uniform grain size during the reaction synthesis process at this temperature. At a reaction temperature of 1500 ^{o}C, well-faceted polygonal grains of an average size of 9 – 12 µm can be seen (Figure 4.5c and h). A reaction temperature of 1600 ^{o}C resulted in a tightly packed matrix of 15 – 30 µm sized grains with a cubic shape (Figure 4.5d).

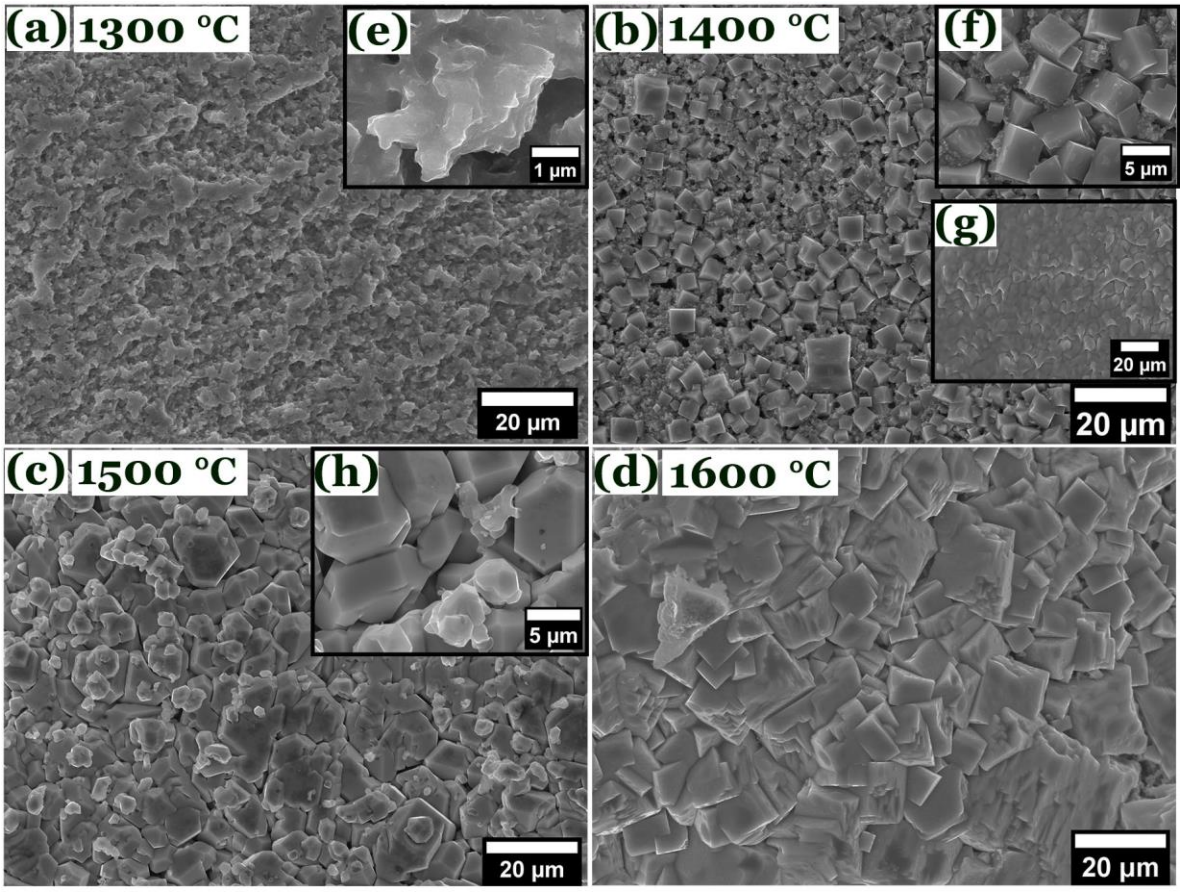

Figure 4.5: SEM micrograph of UHS BaB_6 synthesized at (a & e) 1300, (b, f, & g) 1400, (c & h) 1500, (d) 1600 °C.

Similarly, a series of investigations was performed at various temperatures to identify the optimum reaction temperature for $La_{0.5}Ba_{0.5}B_6$ and $Ce_{0.5}Ba_{0.5}B_6$, as shown in Figure 4.6. Figure 4.6a-f shows SEM images of $La_{0.5}Ba_{0.5}B_6$ and $Ce_{0.5}Ba_{0.5}B_6$, synthesized at three distinct reaction temperatures: 1700, 1900, and 2100 ^oC. At low reaction temperatures (1700 and 1900 ^oC), loosely bonded and cubic-shaped grains of size 1 - 4 µm can be seen. Note that they are poorly bonded together into a very porous matrix (Figure 4.6a-b and 4.6d-e). At a higher reaction temperature of 2100 ^oC, the grains can be seen to be sintered together more tightly (Figures 4.6c and 4.6f).

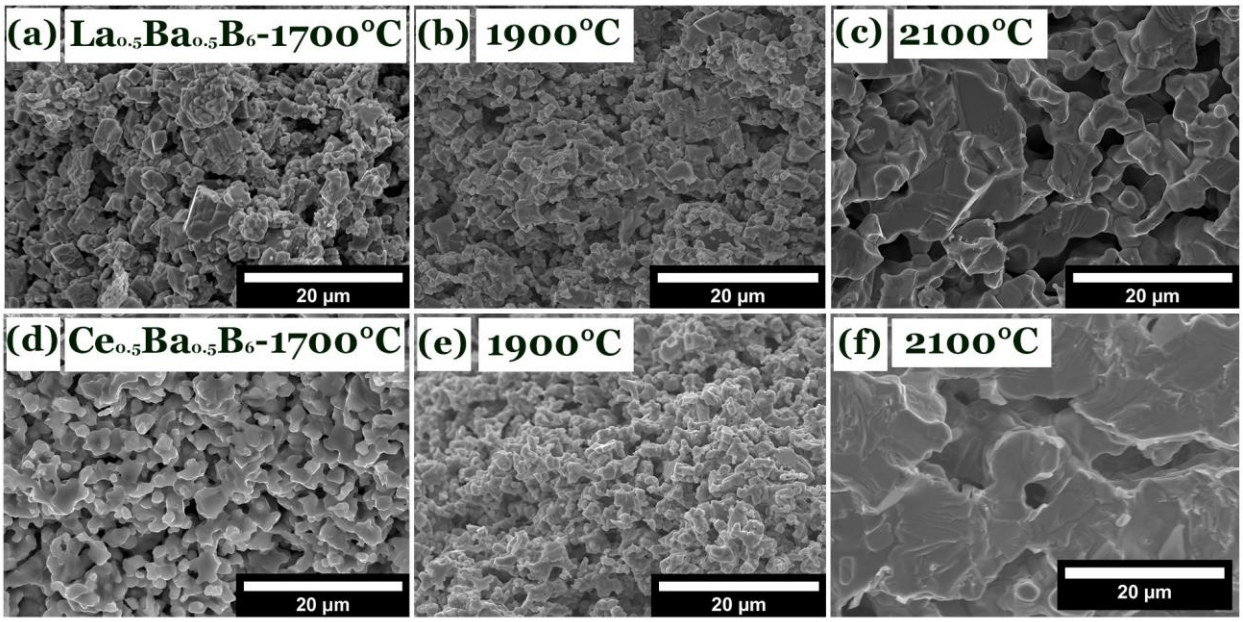

Figure 4.6: SEM micrograph of UHS $La_{0.5}Ba_{0.5}B_6$ synthesized at (a) 1700, (b) 1900, (c) 2100 °C. And $Ce_{0.5}Ba_{0.5}B_6$ synthesized at (d) 1700, (e) 1900, and (f) 2100 °C.

A summary of the different reaction temperatures, grain size, grain morphology, and phase stability are given in Table 4.2. Three key observations must be noted. First, a significant amount of porosity and loosely bond grains were present after synthesis at different reaction temperatures

(see Figures 4.5 and 4.6). Second, the grain size increased substantially with increasing temperature. For example, as shown in Figure 4.5, the grain size increased from about 3-5μm at 1300 °C to 15-30μm at 1600 °C. Third, the grain shape evolved from randomly shaped (see insert of Figure 4.5a) to more cubic (see Figure 4.5d).

Table 4.2. A summary of reaction temperature, grain size, grain morphology, and phase of synthesized BaB_6, $La_{0.5}Ba_{0.5}B_6$, and $Ce_{0.5}Ba_{0.5}B_6$

Composition	Temperature (°C)	Grain size (μm)	grain morphology	Phase (XRD)
BaB_6	1300	3 - 5	random shaped	multi
	1400	5 - 7	cubic	multi
	1500	9 - 12	polygonal	single
	1600	15 - 30	large cubic	single
$La_{0.5}Ba_{0.5}B_6$	1700	1.7 - 3.5	cubic	multi
	1900	2 - 4.5	cubic	multi
	2100	3.0-7.5	random shaped	single
$Ce_{0.5}Ba_{0.5}B_6$	1700	1.5-3.5	cubic	multi
	1900	1.5-3	cubic	multi
	2100	7.1-15	random shaped	single

In the second step, BaB_6, $La_{0.5}Ba_{0.5}B_6$, and $Ce_{0.6}Ba_{0.5}B_6$ pellets were densified by UHS at 1900, 2200, and 2200 °C for 3 minutes, respectively. Resulting SEM images reveal that the microstructures tended to be uniform over a significant area after UHS sintering, as shown in Figures 4.7a-c, respectively. Higher magnification SEM images revealed a dense microstructure with larger grains and low porosity (see Figs. 4.7d-f). The final grain sizes were on the order of 35-40μm for BaB_6, 12-17μm for $Ba_{0.5}La_{0.5}B_6$, and 15-20μm for $Ce_{0.5}Ba_{0.5}B_6$.

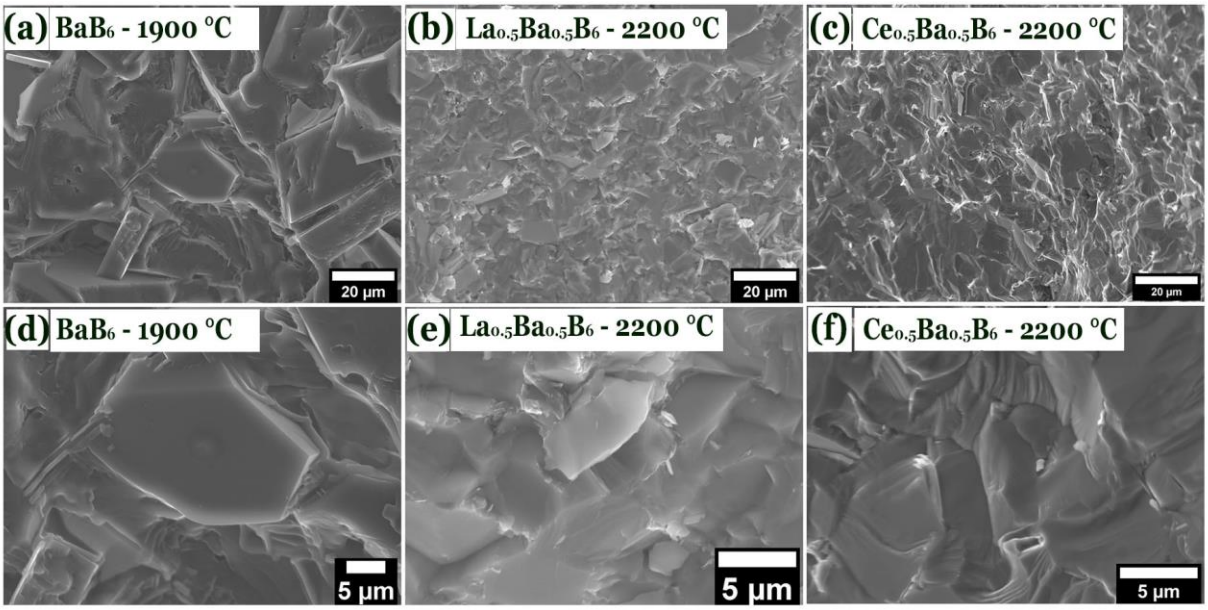

Figure 4.7. SEM images after UHS sintering (2nd firing) for BaB_6, $La_{0.5}Ba_{0.5}B_6$ and $Ce_{0.5}Ba_{0.5}B_6$ that were sintered at (a) 1900, (b) 2200, and (c) 2200 °C, respectively.

4.2.4. EDS

Figures 4.8a-f provide the EDS compositional analysis of UHS sintered (a, d) BaB_6, (b, e) $La_{0.5}Ba_{0.5}B_6$, and (c, f) $Ce_{0.5}Ba_{0.5}B_6$. Analysis revealed ratios of Ba:B=1:5.8 (14.3:85.2 mole%) for BaB_6, La:Ba:B=1:1:11.6 (7.3:6.9:85.6 mole%) for $La_{0.5}Ba_{0.5}B_6$, and Ce:Ba:B=1:0.95:12 (7.5:6.7:85.7 mole%) for $Ce_{0.5}Ba_{0.5}B_6$. The analysis of the boron-to-metal proportion were close to the calculated stoichiometries of BaB_6, $La_{0.5}Ba_{0.5}B_6$, and $Ce_{0.5}Ba_{0.5}B_6$. In each sample, carbon was detected (≤0.7 mol%); in contrast, oxygen was not found. The source of the carbon was from the graphite and polyvinyl alcohol used in pellet formation.

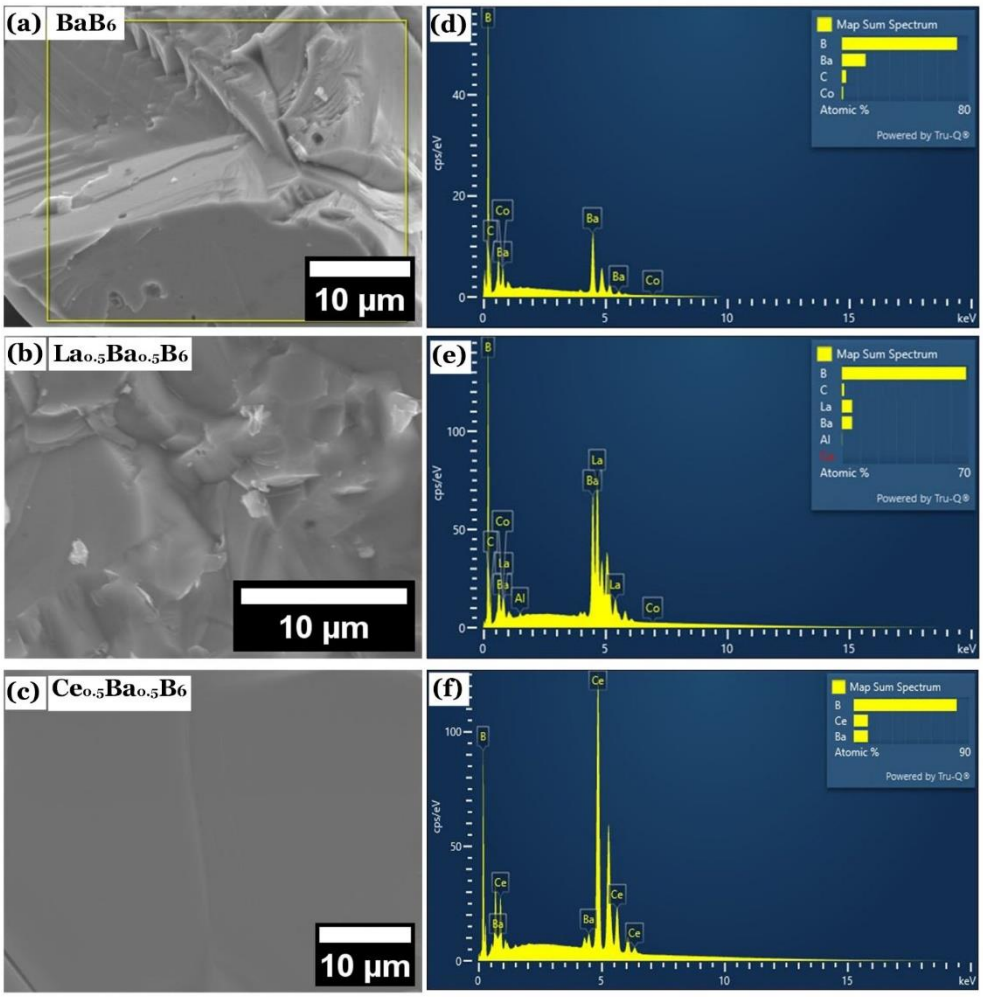

Figure 4.8. EDS compositional analysis of UHS sintered (a,d) BaB_6, (b,e) $La_{0.5}Ba_{0.5}B_6$, and (c,f) $Ca_{0.5}Ba_{0.5}B_6$.

Figures 4.9a-k shows EDS elemental mapping of UHS sintered (a-c) BaB_6, (d-g) $La_{0.5}Ba_{0.5}B_6$, and (h-k) $Ce_{0.5}Ba_{0.5}B_6$. The distribution of boron and the metal cations (Ba, La, and Ce) was found to be uniform. This finding demonstrates that the boron carbide reduction technique used in UHS sintering did not resulting in elemental clustering and/or phase separation. Indeed, the samples evidenced dense microstructures (SEM), single phase formation (XRD) and uniform compositional profiles (with stoichiometries close to the expected).

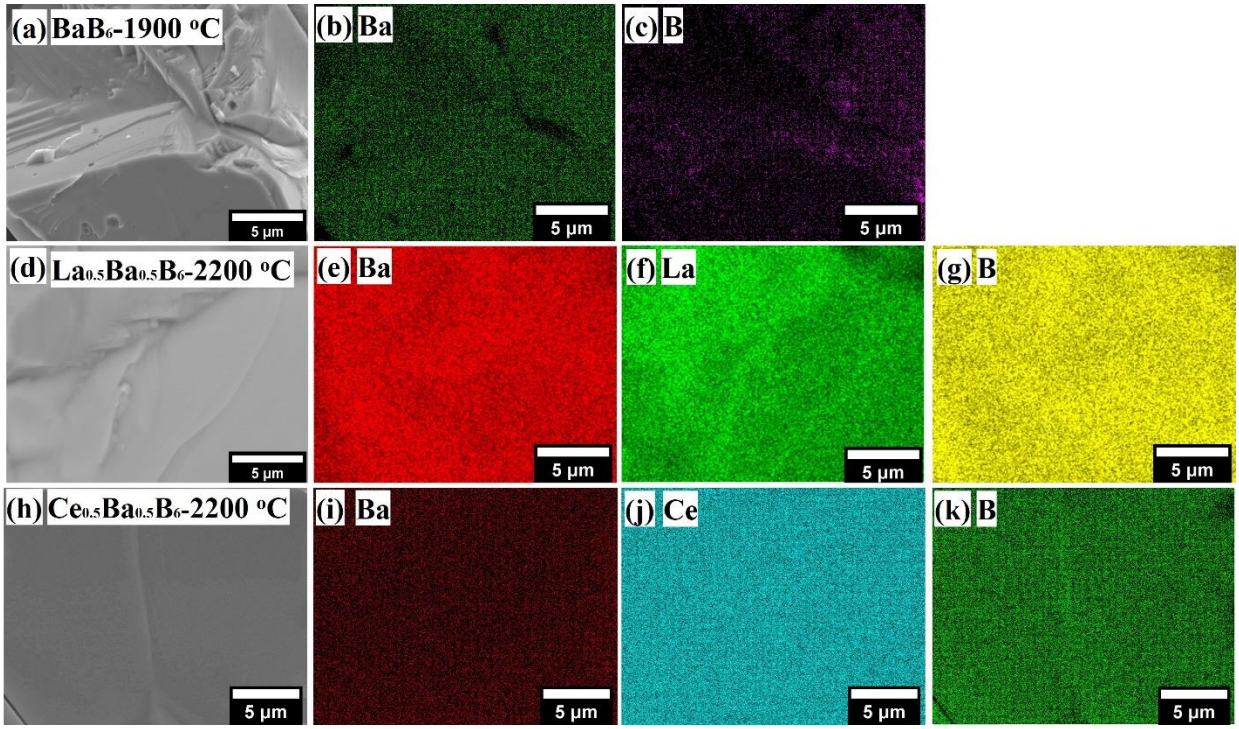

Figure 4.9. EDS elemental mapping of UHS sintered (a-b) BaB_6, (d-g) $La_{0.5}Ba_{0.5}B_6$, and (h-k) $Ce_{0.5}Ba_{0.5}B_6$.

4.2.5. KPFM

The work functions of UHS sintered BaB_6, $La_{0.5}Ba_{0.5}B_6$, and $Ce_{0.5}Ba_{0.5}B_6$ were measured by KPFM. First, calibration results were obtained using multiple samples with known values of W_f: gold (Au) and sintered LaB_6 and CeB_6 ceramics. Second, the sample was polished to provide a smooth scan. Height retrace scans showed a surface roughness of ±11, ±18, and ±20 nm over a 1 µm scan area for sputtered gold, LaB_6, and CeB_6, respectively (see Figure 4.10a-c). The contact potential difference values for sputtered gold, LaB_6, and CeB_6 were 0.235±0.085, 2.2±0.1, and 2.225±0.075 eV, respectively, as shown in the potential trace map in Figure 4.10a-c. The W_f values for sputtered gold, LaB_6, and CeB_6 were then calculated to be 5.1±0.09, 2.7±0.1, and 2.68±0.08

eV, respectively. These values were found to be close to previously reported W_f data [30,63,108,109,139].

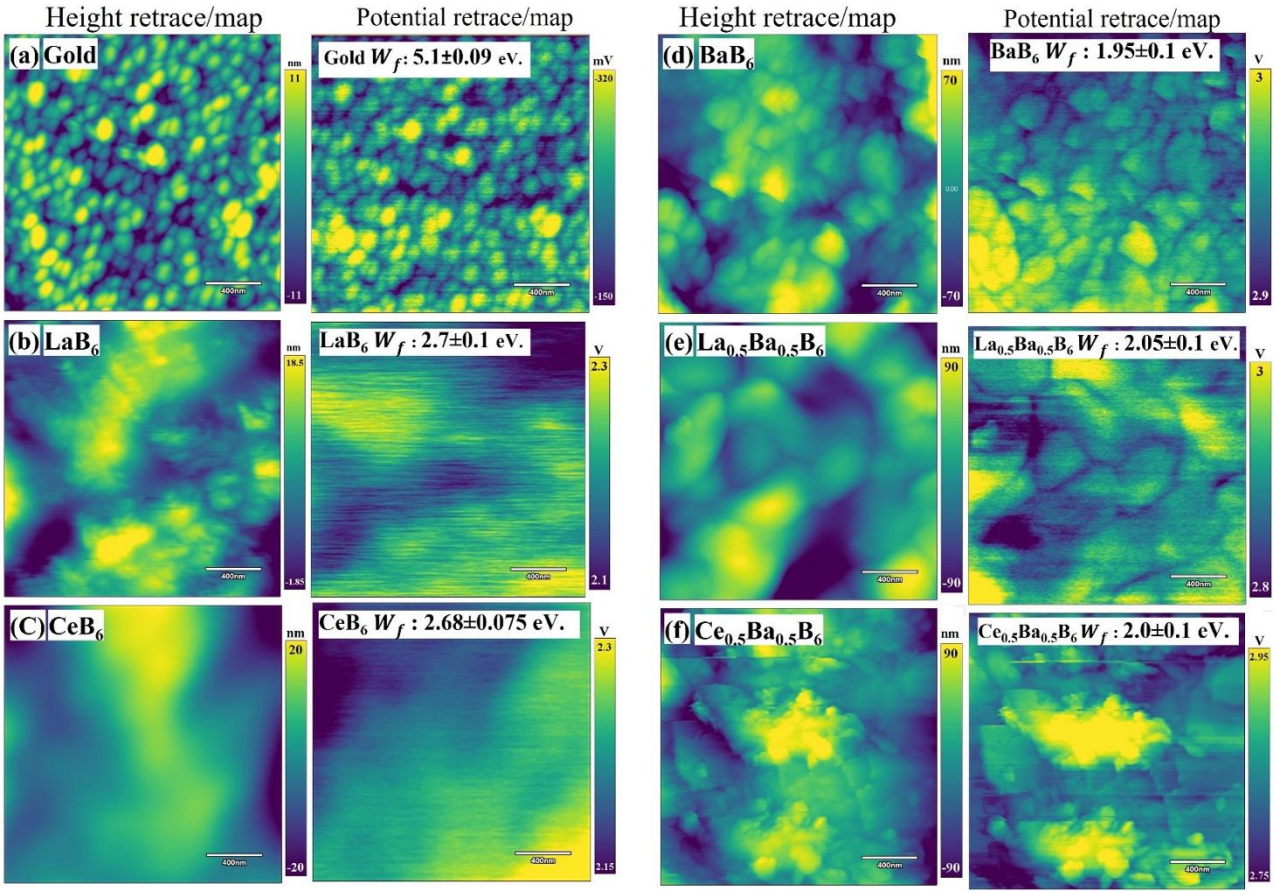

Figure 4.10. KPFM topography (height retrace/map) and CPD (potential retrace/map) images on (a) sputtered gold, (b) LaB_6, (c) CeB_6, UHS (d) BaB_6, (e) $La_{0.5}Ba_{0.5}B_6$, and (f) $Ce_{0.5}Ba_{0.5}B_6$.

After calibration, KPFM measurements were obtained for the polished surfaces of UHS sintered BaB_6, $La_{0.5}Ba_{0.5}B_6$, and $Ce_{0.5}Ba_{0.5}B_6$, as shown in Figures 4.10d-f. The height retrace scans showed roughness values of ±70, ±90, and ±90 nm over a 1 μm^2 scan area for the respective samples. The CPD values for BaB_6, $La_{0.5}Ba_{0.5}B_6$, and $Ce_{0.5}Ba_{0.5}B_6$ were found to be 2.05±0.15, 2.00±0.1, and 2.05±0.1 eV, respectively. The W_f results for BaB_6, $La_{0.5}Ba_{0.5}B_6$, and $Ce_{0.5}Ba_{0.5}B_6$

were then determined to be 1.95±0.1, 2.05±0.1, and 2.0±0.1 eV, respectively. The W_f values for BaB_6 and $La_{0.5}Ba_{0.5}B_6$ were found to be close to previously reported W_f data [23,30,140].

Figure 4.11 provides summary W_f data for the various samples and calibrations, as well as findings from prior studies. The results clearly show that the addition of BaB_6 in $La_{0.5}Ba_{0.5}B_6$ and $Ce_{0.5}Ba_{0.5}B_6$ resulted in about a 25% decrease in W_f. Note that the value for LaB_6 decreased from 2.7±0.1 to 2.05±0.1 eV; similarly, the value of W_f for CeB_6 decreased from 2.68±0.08 to 2.0±0.1 eV. These results are clear and unambiguous that electropositive Ba substitution results in a decrease in W_f. Following the Richardson equation, a 25% reduction in W_f will result in an increase of the emission current densities of LaB_6 and CeB_6, by a factor of ~120 times (12,000%).

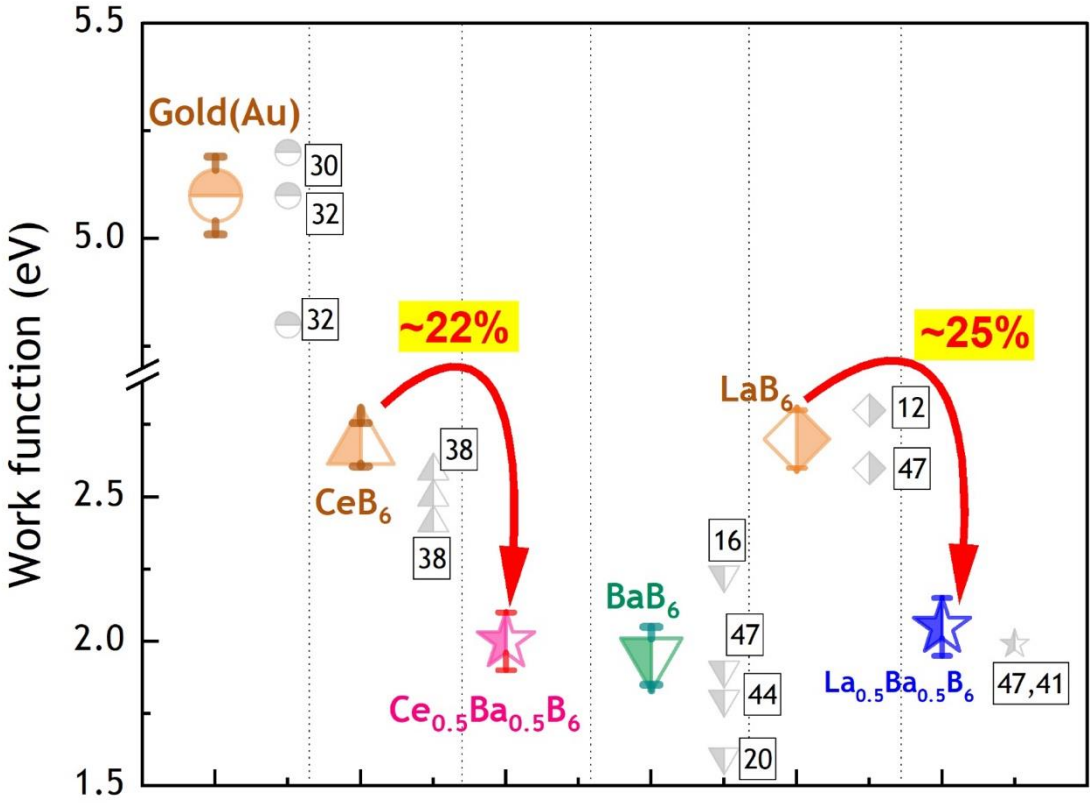

Figure 4.11. Comparison of our measured KPFM data with previously reported work function values.

The decrease in W_f with Ba substitution into LaB_6 and CeB_6 can reasonably be explained as follows. W_f depends on the surface dipole energy and electro-chemical potential [141]. The surface dipole energy (E_{DP}) is the energy barrier for extracting an electron from the surface of a solid. BaB_6 has a higher electro-positivity, and longer B-B and Ba-B bond lengths, compared to LaB_6 and CeB_6 [28]. During solid-solution formation of a multi-component hexaboride, a large size cation Ba (2.15A) replaces Ce (1.85A) and/or La (1.95A). This switch results in the outer electrons being more loosely bound, reducing E_{DP} energy (52). Previously reported ab-initio calculations confirm that the charge transfer between cations (La/Ba) and anions (B) in $La_xBa_{1-x}B_6$ is stronger than that in LaB_6, resulting in a more electro-positive surface [23]. Together, these effects (longer bond length, higher electro-positivity, and more loosely bonded outer electrons, result in a reduction of W_f by Ba-substitution for La and/or Ce in the $(La_{0.5}Ba_{0.5})B_6$ and $(Ce_{0.5}Ba_{0.5})B_6$ solid solutions.

4.3. Conclusion

Ultra-fast high temperature sintering was utilized to synthesize and densify single-phase bulk polycrystalline hexaborides. First, green pellets were heated during the reaction synthesis (B_4C reduction technique) and then sintered at a rate of up to 10^3-10^4 ^oC/min. Using a vacuum atmosphere, densities ~ 90% theoretical were obtained in 180 seconds. After UHS sintering, XRD analysis confirmed the presence of phase pure cubic BaB_6, $La_{0.5}Ba_{0.5}B_6$, and $Ce_{0.5}Ba_{0.5}B_6$. EDS compositional analysis and elemental mapping revealed a stoichiometric reaction product with homogeneous metal cation and boron distributions. The W_f of BaB_6, $La_{0.5}Ba_{0.5}B_6$, and $Ce_{0.5}Ba_{0.5}B_6$ were determined to be 1.95±0.1, 2.05±0.1 and 2.0±0.1 eV, respectively, by KPFM. The addition of BaB_6 in $La_{0.5}Ba_{0.5}B_6$ and $Ce_{0.5}Ba_{0.5}B_6$ resulted in a 25% decrease in W_f for LaB_6 from 2.7±0.1 to 2.00±0.1 eV, and a 23% decrease in W_f for CeB_6 from 2.68±0.08 to 2.05±0.1 eV. Ba-

substitution was thus confirmed to be an effective method for lowering W_f in a variety of multicomponent hexaborides.

CHAPTER V. THIN FILM DEPOSITION OF ELECTRONIC EMITTING THIN FILMS ON HIGH TEMPERATURE STRUCTURAL AND DIELECTRIC SUBSTRATES

This work is going to be submitted for future publication.

This chapter discusses the deposition of thin films of electron-emitting materials on high-melting temperature substrates. Specifically, our efforts focused on depositing CeB_6 on ZrB_2, which will be shown to be polycrystalline. Non-epitaxial CeB_6 thin films were sputtered on UHS sintered ZrB_2. The materials share a common boron chemistry, but have notably different structures, making epitaxy difficult. Dense high-quality films were fabricated, as shown by microstructural analysis, and their properties were studied. The findings from this investigation reveal the potential for developing integrated heterostructures of electron-emitting films on UHTC ceramics. Importantly, this is the first report of a hexaboride films on a UHTC substrate.

Prior published studies have reported the use of (100) and (111) Si single crystalline substrates, which cannot withstand the ultra-high temperature range of UHTCs [80,81], given that its melting temperature is 1414 ^{o}C. Alternatively, $SrTiO_3$ (STO) or $SrZrO_3$ (SZO) have melting points of 2100 ^{o}C and 2600 ^{o}C, respectively. The melting temperature range of SZO is close to that of the electron emitting LaB_6, which has the highest of temperatures of the hexaborides. Since STO is commonly available, and its isomorphous and crystal structure are similar to SRO, STO would make a good candidate substrate. Films incorporating the dielectric material $SrHfO_3$ (SHO) have the potential to emit ballistic electrons with energy greater than the W_f. This is because the bandgap (E_g) of SHO is high, but its W_f relatively low. Furthermore, SHO has a melting point of 2900 ^{o}C and it is isostructural with STO.

For this study, epitaxial thin films of $SrHfO_3$ (SHO) were grown on (100), (110) and (111) $SrTiO_3$ (STO) substrates at 600°C using RF sputtering. Subsequent X-ray diffraction (XRD) confirmed the formation of an epitaxial layer, and reciprocal space mapping (RSM) was used to characterize the film's mosaicity/ texture on the different substrates. XRD and RSM data demonstrated that the most favorable film growth direction was (110), while the least favorable was (111). Scanning electron microscopy (SEM) images revealed that ~150 nm thin films could be grown in 6 hours (h). Heterostructures of SHO/STO thus offer a potential model system for study of epitaxial single crystals and anisotropy.

5.1. CeB_6 films on ZrB_2

5.1.1. Experimental

5.1.1.1. Substrate preparation: To prepare the surface of the sintered ZrB_2 substrates, the substrate was initially ground with 120 to 1200 grit SiC papers, then polished with 15 to 0.5 µm diamond paste, and finally polished with an alumina and colloidal SiO_2 suspension to create a smooth and flat surface substrate for thin-film deposition. An automatic sample polisher was used for the grinding and polishing operations. After final polishing, the substrates were cleaned in the following sequence: sonicated in acetone for 5 min, then in ethanol for 10 min, and finally in di-water for 10 min. The cleaned substrates were air dried before use in the deposition process.

5.1.1.2. Deposition: The CeB_6 (CB) and $SrHfO_3$ (SHO) thin-film deposition was accomplished with an RF sputtering unit (ACT Orion, A300 series, A3CV & CTM magnetron sputtering, AJA International, Inc, Massachusetts, USA). Ar (99.99%) was used as a sputtering agent to create a glow discharge that bombarded the CB and SHO target. Cleaned and dried substrates were attached to the substrate holder with the help of clips. During sputtering, Ar (10 standard cubic centimeter per minute or sccm) with a fixed pressure of 5 and 10 mTorr was used.

A fixed deposition temperature of 600 °C was maintained during sputtering for all films. Each substrate was held for 30 min in Ar gas at 600 °C before and after the deposition process, and subsequently cooled to room temperature at a rate of 10 °C/ min. A total deposition time of 6 hours (h) was maintained for all experimental cycles. A distance of about 10 cm was maintained between the target and substrate, and the films were deposited using a RF power of 50 and 100 W. Table 5.1 summarizes the experimental parameters for the deposited CeB_6 thin films.

Table 5.1.: All experimental details of the deposited CeB_6 thin films**.**

Film composition	**Substrate**	**Deposition temperature (°C)**	**Deposition Power**	**Gas pressure (mTorr)**	**Gas mixture (sccm) (Ar/O)**
CeB_6	ZrB_2	600	50	5	(10/0)
SHO	ZrB_2	600	100	10	(8/2)
CeB_6	SHO on ZrB_2	600	50	5	(10/0)

5.1.1.3. XRD: Structural analysis and phase identification were carried out using a powder diffraction X-ray measurements (Bruker D8) on the substrate and as-prepared films. Rietveld analysis was performed on the collected XRD data to evaluate the tentative composition of the deposited phase with the help of Maud software.

5.1.2. Results and Discussion

5.1.2.1. XRD: The XRD results for the CeB_6 thin films deposited on ZrB_2 are provided in Figure 5.1a, which shows highly crystalline CeB_6 along with substrate ZrB_2 peaks,. Both the CeB_6 and ZrB_2 peaks match well with the standard diffraction pattern (PDF 00-038-1455) and (PDF 00-034-0423), respectively. The calculated lattice parameters based on the XRD plot were found to

be (a_C)=4.082 Å (2θ=31.042) with a primitive cubic crystal structure and space group of Pm−3m for CeB_6. The ZrB_2 evidenced a hexagonal crystal structure with lattice parameter (a_H, c_H) = 3.136, c:3.500 Å. To better estimate the composition of the XRD data, Rietveld analysis was performed; the resulting data corresponded well with standard PDF card with experimental data, as shown in Figure 5.1b. The lattice parameter of the CeB_6 thin film was found to be slight smaller (1.142%) than the standard PDF card (a_C)=4.141 Å, which might be due to compressive stress from the smaller lattice parameter of ZrB_2.

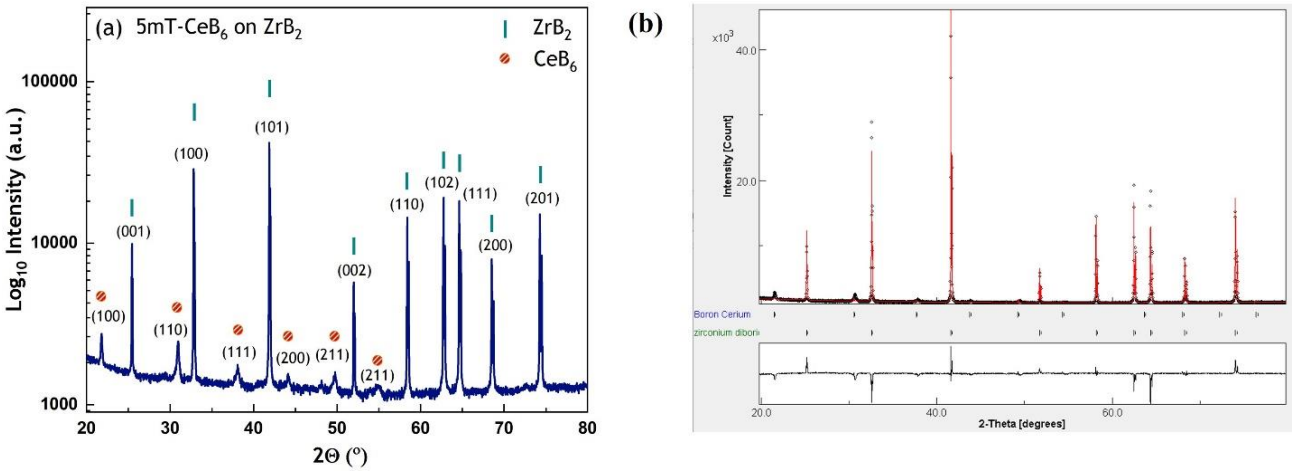

Figure 5.1. XRD graphs of as-deposited (a) CeB_6 on ZrB_2 deposited at 5mTorr, (b) Rietveld analysis.

Additionally, the effect of an additional SHO buffer layer on ZrB_2 for CeB_6 thin films was studied. For this experiment, an SHO thin film was first deposited at 10 mTorr pressure in the presence of a gas mixture of Ar/O_2: 8/2 sccm at 600 °C for 6 hours, after which the CeB_6 thin film was deposited on the SHO layer deposited earlier. XRD data for the CeB_6 thin film on SHO on ZrB_2 is shown in Figure 5.2. The CeB_6, SHO, and ZrB_2 peaks matches with the standard diffraction

pattern (PDF 00-038-1455), (PDF 01-089-9026), and (PDF 00-034-0423), respectively. The CeB_6 and SHO peaks can be superimposed with good agreement due to their similar lattice parameters; the calculated lattice parameters based on the XRD plot were found to be (a_C)=4.110 Å (2θ=30.83), with a primitive cubic crystal structure and space group of Pm−3m. The lattice parameter of the CeB_6/SHO film was found to reduce the lattice parameter difference (of CeB_6/ZrB_2) by 0.748% in comparison to the standard PDF card (a_C)=4.141 Å, which might be due to similar lattice parameters for SHO (4.113 Å) and CeB_6 (4.141 Å) than ZrB_2 ((a_H, c_H) = 3.136, c:3.500 Å). In addition to the CeB_6 and SHO peaks, some additional peaks at 2θ = ~ 29.679, and 34.518 were found, which might be due to the formation of mix-oxide SrO, HfO_2, and ZrO_2, as shown with violet color triangle marked in Figure 5.2a.

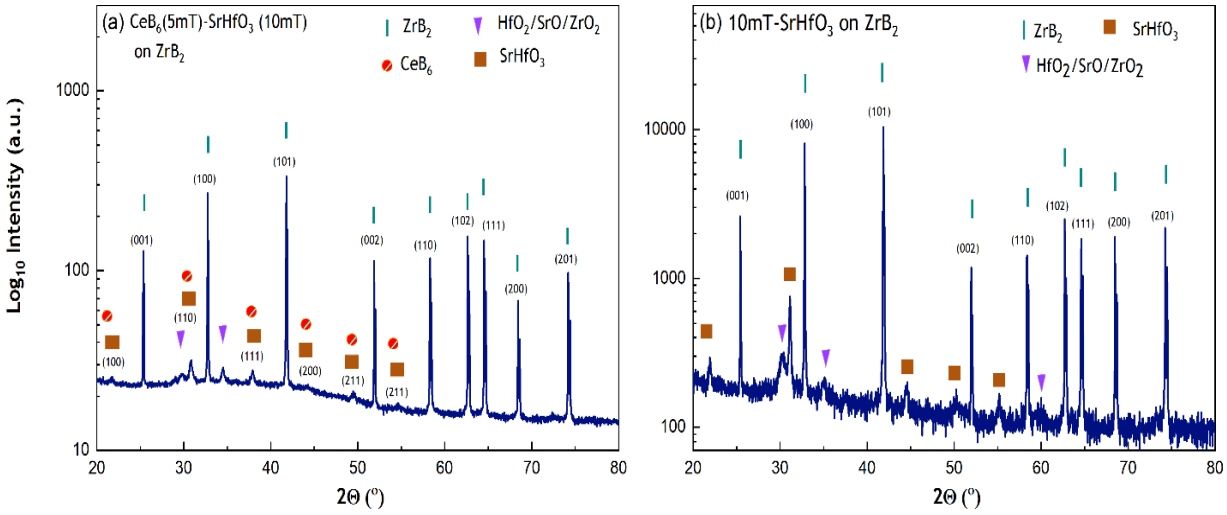

Figure 5.2. XRD graphs of as-deposited (a) CeB_6 on SHO on ZrB_2, (b) SHO on ZrB_2 deposited at 10mTorr.

To further investigate the source of the mix-oxide SrO, HfO_2, and ZrO_2, only SHO films were deposited on ZrB_2 at 10mTorr at 600 °C (same deposition condition as prior SHO films). The

resulting XRD data for the deposited film are shown in Figure 5.2b. Both SHO and ZrB_2 peaks were identified, which matched well with standard diffraction patterns (PDF 01-089-9026) and (PDF 00-034-0423), respectively. The calculated lattice parameters based on the XRD plot were found to be (a_C)=4.0726 Å (2θ=31.12), with a primitive cubic crystal structure and space group of Pm−3m. The lattice parameter of the SHO was found to be slightly smaller than the standard PDF card (a_C)=4.113 Å, which might be due to compressive stress from the smaller lattice parameter of ZrB_2. In addition to the ZrB_2 and SHO peaks, additional peaks at 2θ = ~ 29.679, 34.518, and 60.28 were observed (same as the buffer SHO film), which might be due to the formation of mixed-oxide SrO, HfO_2, and ZrO_2, as indicated by the violet-colored triangles in Figure 5.2b. Therefore, it can be concluded that mixed-oxide SrO, HfO_2, and ZrO_2 formed during SHO deposition; we attribute this finding to the presence of oxygen in the sputtered gas mixture and oxide from SHO at 600 °C deposition temperature and prolong deposition time.

5.1.1.2. SEM: Cross-sectional SEM images obtained for the CeB_6, SHO, and CeB_6/SHO heterostructure revealed a uniform coverage of the film on the ZrB_2 substrate with very smooth appearance, as shown in Figure 5.3. The thickness of the CeB_6, SHO, and CeB_6/SHO films deposited for 6 hours were ~ 350, 700 (6+6 hours), and 350 nm, respectively. By comparing the thickness values for the 6- and 12-hour films, it can be concluded that the growth rate for all three films was nearly linear with time.

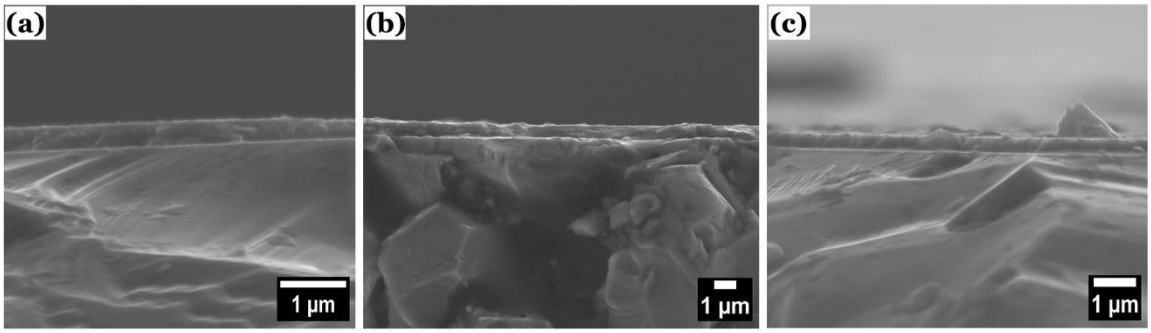

Figure 5.3. SEM micrograph of the cross-sectional of (a) CeB_6/ZrB_2, (b) SHO/ZrB_2, and (c) $CeB_6/SHO/ZrB_2$ heterostructure.

5.1.1.3. AFM: The surface roughness of the as-deposited CeB_6 thin films was measured by AFM (Figure 5.4). The images showed a smooth and fine-grained surface morphology for CeB_6/ZrB_2. surface roughness profile for the CeB_6 film displayed a root mean square or R_{ms} of 4.041±0.649 nm over a 2 × 2 μm^2 area and a skewness of 0.119.

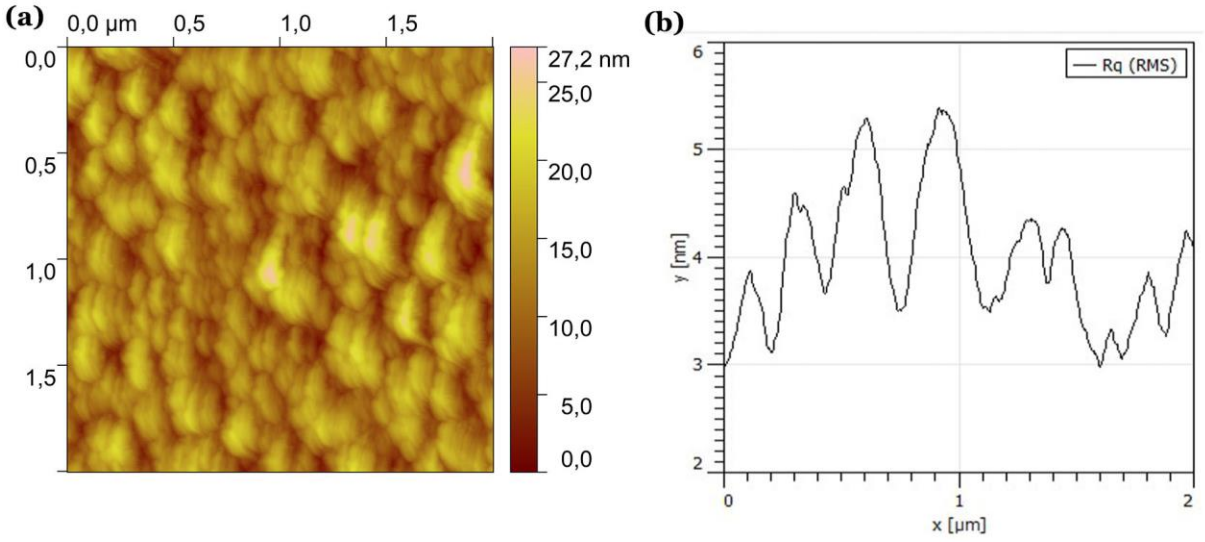

Figure 5.4. AFM image of the (a) CeB_6/ZrB_2 and (b) root mean square or R_{ms} map over the surface.

5.2. SHO on STO

5.2.1 Experimental

Substrates of (100), (110) and (111) STO were procured from CrysTec, GmbH (Germany). A sintered $SrHfO_3$ (SHO) sputtering target (99.95% purity, 2-inch diameter) was purchased from Kurt J. Lesker Company (USA). The SHO thin films were deposited by a RF sputtering unit (ACT Orion, A300 series, A3CV & CTM magnetron sputtering, AJA International, Inc, Massachusetts, USA). As a sputtering agent, Ar (99.99%) was used to create a glow discharge that bombarded the SHO target**.** Before deposition, all STO substrates **(**10×5 mm^2) were sonicated in ethanol for 10 minutes in two separate cycles to remove dirt and oil. The cleaned and dried substrates were then attached to the substrate holder with the help of silver paste.

XRD reciprocal space mapping (RSM) was performed (PANalytical X'Pert MRD Pro) to evaluate the epitaxial / textural characteristics of the thin films. RSM scans were obtained via a CuK_α radiation ($\lambda = 0.1542$ nm, operated at 45 kV and 40 mA). Each scan was performed about a substrate main 2θ peak at a 2θ increment of 0.02 °. For example, the SHO/STO(110) film was scanned between 2θ = 29.071 to 34.071 °; likewise, the SHO/STO(100) and (111) films were scanned between 2θ = 42.582 to 47.582 ° and 37.431 to 42.431 °, respectively. Atomic force microscopy (AFM) images were obtained (Dimension 3100, Vecco) in tapping mode. Scanning electron microscopy (SEM) images were obtained (JEOL IT500 SEM and LEO FESEM) from the fractured / cleaved surface to view both the film-substrate interface and top surface.

5.2.2. Results and Discussion

5.2.2.1. X-ray diffraction

XRD line scans (θ-2θ scan) of different SHO/STO heterostructures revealed highly crystalline (100)[001], (110)[011], and (111)[111] oriented SHO thin films on (100)[001], (110)[011] and

(111)[111] STO substrates respectively. These findings are shown in Figure 5.5. All of the θ-2θ line scans displayed well-distinguishable SHO peaks that was distinct from the STO peaks. This outcome demonstrates the good epitaxial alignment of each thin film with its substrate (as illustrative by a pink arrow). No secondary phases were observed in the line scans. The lattice parameters (out-of-plane (OP) direction) for all the three SHO films were calculated using Bragg's law from the θ-2θ scan, as summarized in Table 5.2. The SHO (100)[001] film had a peak at 2θ = 21.68 ° and a lattice parameter of 4.09 ± 0.005 Å. The SHO (110)[011] film had a peak at 2θ = 30.82 ° and a lattice parameter of 4.09 ± 0.005 Å. And the SHO (111)[111] film had a peak at 2θ = 38.05 ° and a lattice parameter of 4.09 ± 0.005 Å. The XRD intensity of the SHO(111) film was low in comparison to the SHO(100) and SHO(110) films. The low intensity for the SHO(111) peak might be due to poor peak coherency during film growth and reduced thickness due to a slow growth rate for SHO(111).

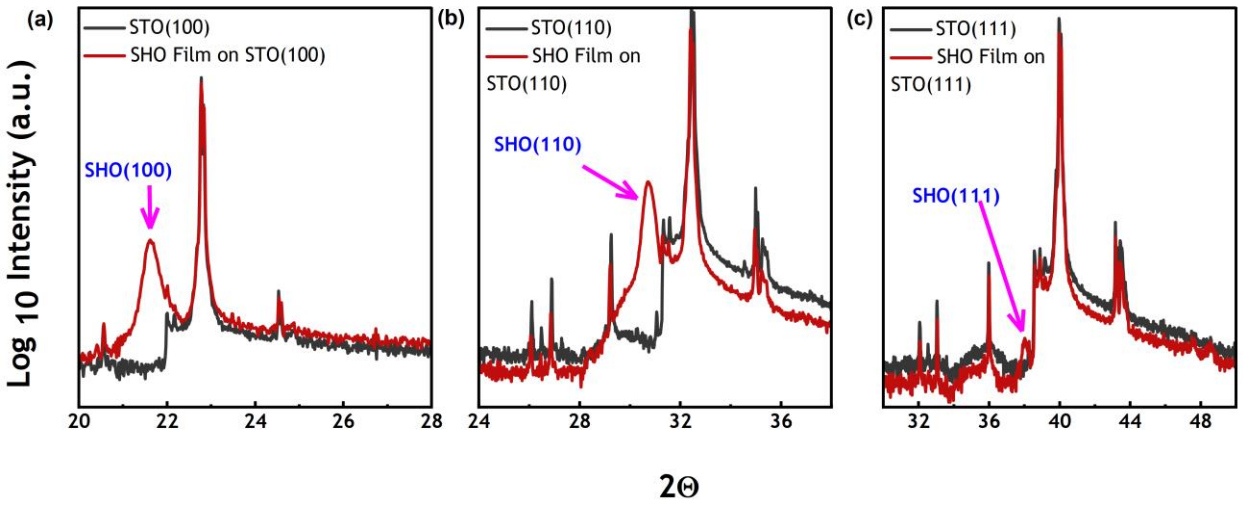

Figure 5.5. θ-2θ XRD scan of SHO/STO (100), (110) and (111) films. The SHO (001) and (011) films (large peaks) grew well beside STO (001) and (011) substrate peaks, as marked with a pink arrow. In contrast, the SHO (111) film did not grow well on STO (111) within the deposition duration.

Table 5.2. SHO (100), (110) and (111) films' θ-2θ XRD scan results

Film direction	**(100)**	**(110)**	**(111)**	**Cubic and pseudo-cubic SHO**
θ-2θ				
	21.68 ± 0.001	30.82 ± 0.004	38.05 ± 008	-
FWHM (°)	0.35 ± 0.009	0.425 ±0.011	0.48 ± 0.029	-
Lattice parameter (Å)	4.09 ± 0.005	4.09 ± 0.005	4.09 ± 0.005	4.06 - 4.15 Å [84,86,92]
Peak height (a. u.)	2987.6 ±14.628	9807 ± 56.285	222 ± 4.367	-
Rocking Curve (ω-2θ)				
Diffraction condition (200) [002]	4.09 ± 0.005	4.08 ± 0.005	4.08 ± 0.005	
Diffraction condition (220) [022]	4.09 ± 0.005	4.09 ± 0.005	4.09 ± 0.005	

Previously reported lattice parameters for various $SrHfO_3$ bulk and thin film samples are summarized in Table 5.3. For reference, the lattice parameter of cubic $SrTiO_3$ crystals is a_c = 3.905 Å [92,142]. Recent literature reports describe a cubic phase of SHO with a_c = 4.114 Å and a pseudo cubic one with a_c = ~4.087Å [92,142]. Our deposited SHO featured a single lattice parameter of 4.08-4.09 Å, indicating that the crystal structure of SHO film is cubic / pseudocubic. Other polymorphic forms of SHO displayed different lattice parameters, as summarized in Table 5.3: (a_o, b_o, c_o) = (5.787, 5.774, 8.15) Å for orthorhombic, and (a_t, c_t) = (5.79, 8.21) Å for tetragonal. The crystal structure of a substrate beneath the epitaxial layer is intended to remain within the thin film. Thus. SHO (a_c = 4.114 Å) films on STO (a_c = 3.905 Å) offer a reasonable lattice match by which to maintain epitaxy.

Table 5.3: List of lattice parameters crystal structure, and temperature of phase transition for various polymorphic phases of bulk and thin film $SrHfO_3$.

		Lattice parameter (Å)						
		(a) (Å)	α (°)	(b) (Å)	β (°)	(c) (Å)	γ (°)	Phase transitions temperature (°C)
SHO	Orthorhombic (*Pbnm*)	5.787	90	5.774	90	8.177	90	
	Orthorhombic (*Cmcm*)	8.174	90	8.197	90	8.179	90	400-600
	Tetragonal (*I4/mcm*)	5.790	90	5.790	90	8.212	90	600-750
	Cubic ($Pm\bar{3}m$)	4.114	90	4.114	90	4.114	90	1130
	Pseudo-cubic	4.087		4.077		4.087		
STO	(Cubic)	3.905 - 3.92	90	-	90	-	90	

To investigate the possibility of peak splitting, which is indicative of lower symmetry structure from orthorhombic / tetragonal structure, rocking curves (RC) were measured, as given in Figure 5.2. RC scans along different axes of (002), (022), and (222) were obtained for (011) SHO films, and the peaks were analyzed (i.e., peak deconvolution) to identify the feasibility of the peak splitting and peak flatness as summarized in Figure 5.6 and Table 5.4. We considered the possibility of the peak presence of one and two peaks in fitting, yielding R^2 values of 0.99529 and 0.9984, respectively. This result demonstrates that whether we used a single peak or multiple peaks, we would end up with the same statistical confidence in the analysis. Therefore, the peaks need to be considered as a single unsplit one, yielding a cubic or pseudocubic structure. Although the peaks were broad, statistically there is no evidence that can be inferred from the analysis that supports the presence of a lower local symmetry structure.

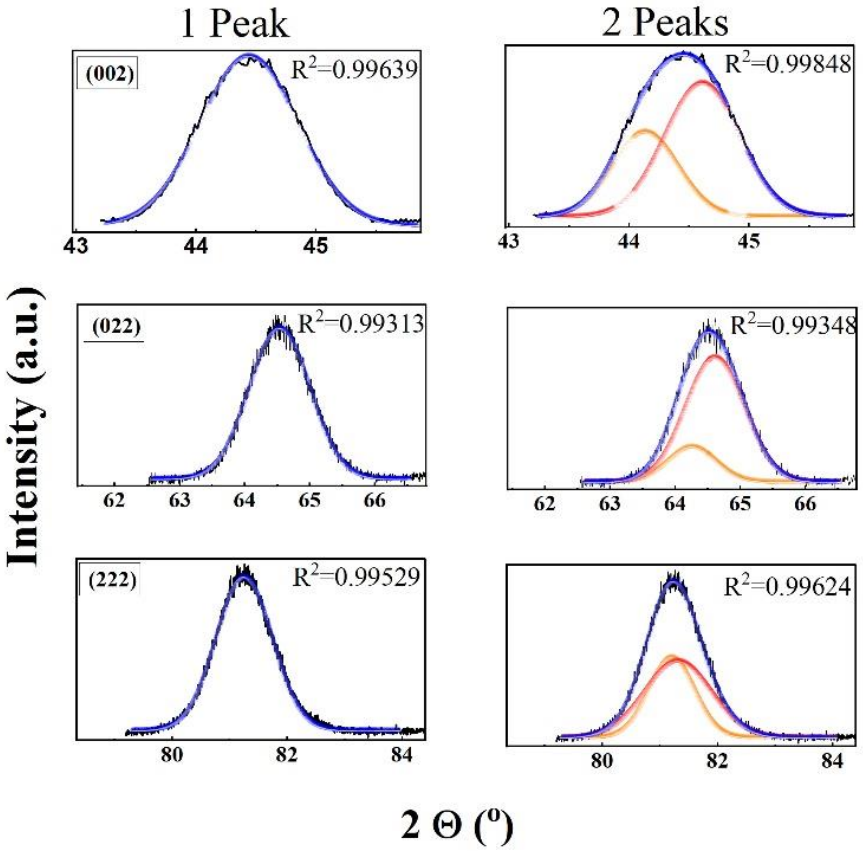

Figure 5.6. Peak fitting analysis (Gaussian function) of rocking curve (RC) of SHO/STO (110) at [002], [022], and [222] diffraction condition.

Table 5.4: Peak fitting analysis (peak deconvolution) of multiple RC peaks at different diffraction condition (such as (002), (022), and (222)) for (011) SHO thin films based on number of peaks 1 to 2.

	Number of peaks	**Peak number**	**2θ**	**FWHM**	**R-Square (COD)**
022	1	1	64.54 ± 0.001	1.10 ± 0.004	0.99313
	2	1	64.25 ± 0.135	0.87 ± 0.288	0.99348
		2	64.61 ± 0.214	1.07 ± 0.113	
002	1	1	44.36 ± 0.002	0.97 ± 0.007	0.99639
	2	1	44.13 ± 0.029	0.65 ± 0.024	0.99848
		2	44.61 ± 0.027	0.75 ± 0.026	
222	1	1	81.25 ± 0.001	1.15 ± 0.003	0.99529
	2	1	81.20 ± 0.009	0.95 ± 0.035	0.99624
		2	81.31 ± 0.014	1.38 ± 0.044	

Next, reciprocal space maps (RSM) were obtained, as shown in Figure 5.7. Scans were measured around the (001), (011) and (111) peak positions of STO substrates, which enabled us to study the (001), (011) and (111) SHO films. This approach was undertaken to establish the epitaxial relationship between the crystalline structure and coherency of the SHO film on STO substrates. Careful calibrations and zone alignment were conducted first. The SHO films were coherent on both (011) and (001) STO substrates, but not for (111) STO. The results indicate a preferential crystal orientation for SHO of (011)> (001)> (111). We note that all the films were deposited at 25 mTorr and thus had a similar thickness.

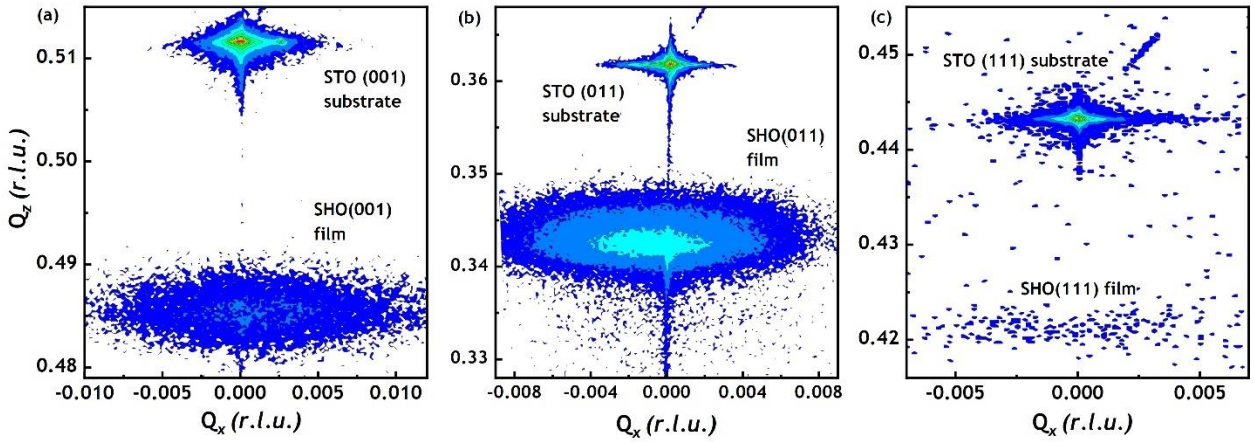

Figure 5.7. RSM scan of (110), (100) and (111) films.

5.2.2.2. Film thickness and surface coverage

SEM images obtained for a SHO/STO (110) heterostructure revealed the uniform and complete coverage of the film on the substrate with very fine granular features (nanometer sized) over an area of 6 μm^2, as shown in Figure 5.8a. The thickness values for the (110) and (100) SHO films deposited for 3 h were ~ 75 and 47 nm, respectively, as shown in Figure 5.8b and c. Correspondingly, a 6 h deposition resulted in a 150 nm thickness for the (110) film, see Figure 5.8d. By comparing the thickness values of 3h and 6h SHO (110) films, it can be concluded that the growth rate along the (110) was nearly linear with time. Also, by comparing the thickness values of 3h SHO (110) (75nm) and 3h SHO (100) (47 nm), it can be inferred that the growth rate along the (110) direction was notably faster than along the (100).

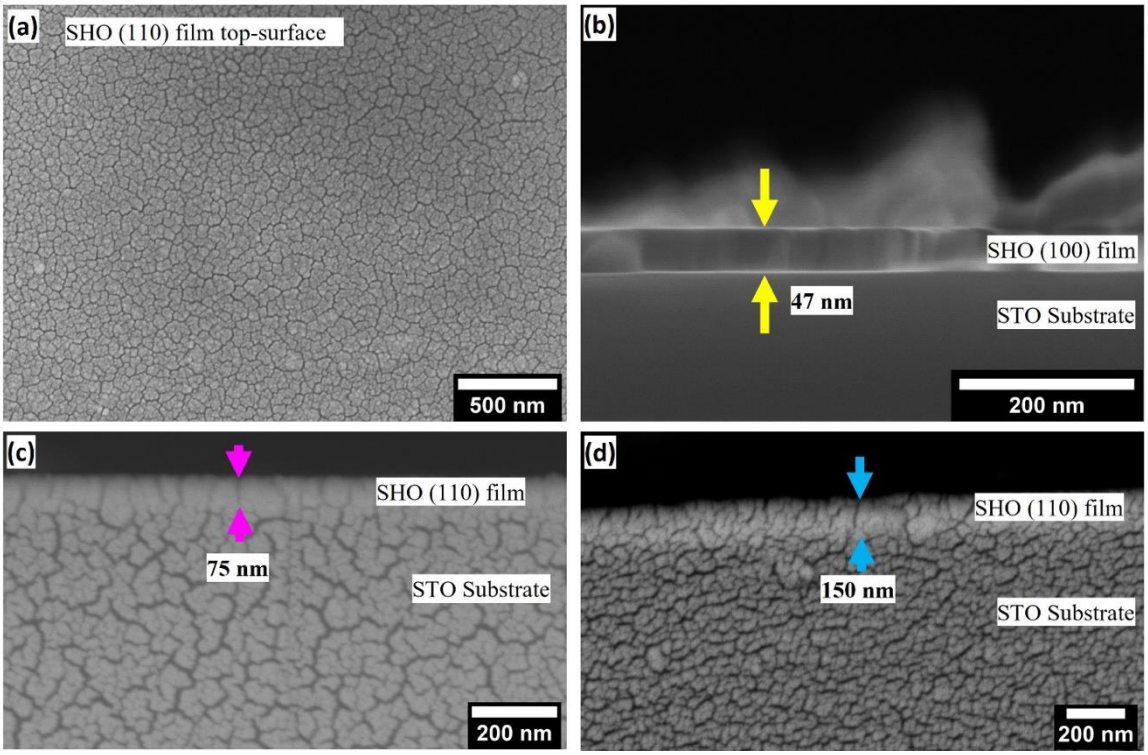

Figure 5.8. (a) SEM image of SHO (110) film's top surface. (b) Cross-section image of SHO (100) film grown for 3 h. (c) Cross-section image of SHO (110) film grown for 3 h. (d) Cross-section image of SHO (110) film grown for 6 h**.**

5.2.2.3 Surface roughness:

The surface roughness of the deposited films was measured by AFM (Figure 5.9), which revealed smooth and fine-grained surface morphologies for SHO/STO(110), (100), and (111). The SHO/STO(110) film had a roughness root mean square or R_{ms} of 0.45 nm over a 2 × 2 μm^2 area and a skewness of 0.334. The SHO/STO(100) film had a R_{ms} of 0.493 nm and a skewness of 0.517. And the SHO/STO(111) film had a R_{ms} of 0.632 nm and a skewness of 1.38. Our RF sputtered SHO thin films were found to have similar roughness values at higher thicknesses compared to the prior reports that used other deposition methods. [84,92]

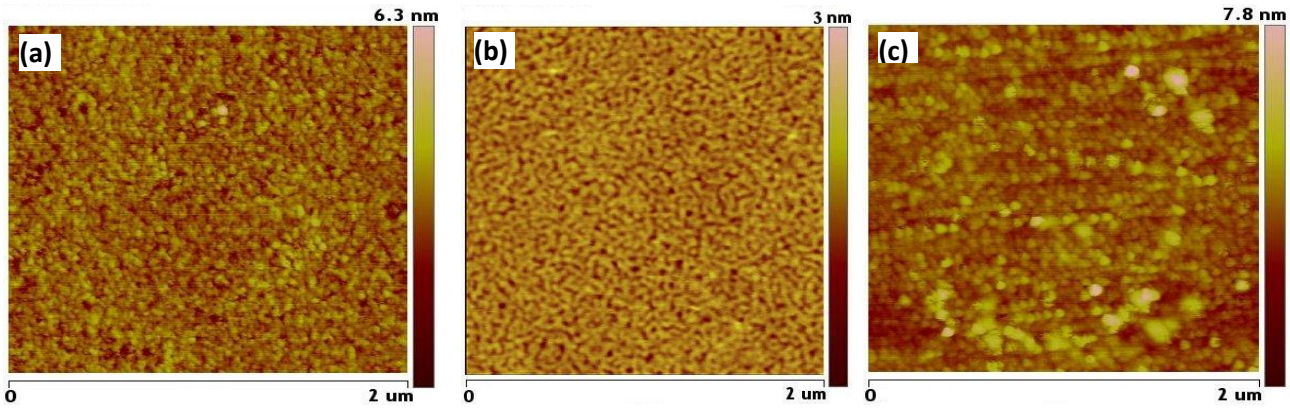

Figure 5.9. AFM surface topography of (a)SHO (110), (b) (100) and (c) (111) film.

5.2.2.4. Orientation-dependent growth

Based on our XRD and RSM results (and using the same deposition conditions), the SHO epitaxial film growth rate along (110) was found to be the highest, followed by (100) and (111). Generally, STO (110) substrates have atomic arrangements in zigzag patterns on the surface, where each atom stays bonded to the two adjacent ones. Each surface atom contains two unsatisfied bonds, which assist in creating bonds with the two new deposited atoms, although the number of unsatisfied bonds stays unaltered. Therefore, the growth along the (110) direction continues smoothly in a planer manner. For the (100) substrates, each surface atom has two bond (with two bulk atoms) and two unsatisfied dangling bonds. These dangling bonds create bonds with two new deposited atoms, and the number of unsatisfied bonds remains the same. Therefore, growth along the (100) direction continues smoothly in a planer manner. In the case of both the (110) and (100) films, when newly deposited atoms bond to the unsatisfied / dangling bonds of the surface atoms, the surface energy does not increase, which is favorable to growth [143]. In comparison to the (100) surface, the (110) surface evidenced a higher number of dangling bonds, which might be responsible for the faster film growth rate along that direction.

For the (111) substrates, two closed pack atomic planes configure on the (111) surface, where each atom stays bonded with neighboring atoms with no dangling bonds. Thus, the surface energy of the (111) is low. Also, the addition of new atoms creates dangling bonds, which is favorable for two-dimensional growth (nucleation) on the (111) surface, rather than planer growth. Accordingly, the (111) film growth rate is slow, requiring higher deposition temperatures; additionally, the resulting surface will be characterized by larger grains compared to the (110) and (100) films [143]. In comparing the AFM and XRD data, it can be concluded that the substrate's orientation has a key impact on the growth rate, mosaicity, and surface roughness of epitaxial SHO films.

5.3. Conclusion

Polycrystalline CeB_6 thin films were deposited on ZrB_2 substrates via RF sputtering. Highly crystalline CeB_6 films were deposited, as observed by XRD measurements, whose crystal structure was cubic. The surface roughness (R_{ms}) of the CeB_6 film was of 4.041±0.649 nm over a 2×2 μm^2 area. SEM imaging confirmed that a ~350 nm thick film was deposited over the course of 6 hours. The addition of an SHO buffer layer on ZrB_2 reduced the compressive stress (of CeB_6) generated due the lattice mismatch (small lattice parameter) of ZrB_2. However, the SHO buffer layer also resulted in the formation of mixed-oxide phases as observed by XRD.

We then deposited epitaxial SHO thin films on STO (100), (110), and (111) substrates by RF sputtering. The substrate orientation was found to influence film growth and mosaicity as follows: (110) films displayed a higher growth rate and lower mosaicity, followed by (100), and then (111). Moreover, the epitaxial film growth was shown to be linearly proportional to deposition time. SEM images showed good film coverage on the substrate. AFM data showed that very smooth film has formed and the (surface roughness root mean square) R_{ms} value of 0.45 nm.

CHAPTER vi. CONCLUSION and ONGOING / FUTURE WORK

6.1. Conclusion

To conclude, this doctoral research achieved three significant outcomes: I developed a process to (a) synthesize and densify low W_f material and UHTCs, (b) reduce the W_f of different common electron emitters, and (c) produce epitaxial and non-epitaxial thin films of low W_f materials on high temperature materials and UHTCs. These materials are potential candidates for ETC-enabled applications. Going forward, subsequent studies will be designed to evaluate the ETC potential of those newly developed materials.

6.2. ETC measurements of UHS sintered dense ZrB_2, LaB_6, CeB_6, $CeBaB_6$, and $LaBaB_6$

The potential applications of the UHTC and low work function are in the leading edges of hypersonic vehicles, thermionic emission of electron [9], field emission electron cathodes in electron microscopes [10], electron transpiration colling, high temperature thermionic energy generators, photo-induced electron emission [11], and solar energy applications [12]. In the case of low W_f materials, electrons can easily overcome the surface potential energy with increasing temperature. The electron transpiration cooling (ETC) is a phenomenon where electrons are used to remove heat and reduce surface temperature of a heated object. The amount of energy/heat carried away by emitted electrons is determined by the potential barrier for the electrons and the kinetic energy associated with the emitted electrons, as shown in Richardson et al.'s Equation 6.1 [144]. This equation contains two terms: the first refers to the direct contribution from the materials work function (W_f), and second corresponds to the kinetic energy ($2k_BT_w$) of the emitted electrons.

$$Q_{ETC} = J_e(W_f + \frac{2k_B T_w}{e}) \quad (6.1)$$

where J_e is the emission current density (Amp $*$ cm^{-2}), T_w is the temperature, K_b is the Boltzmann constant, and A_r is Richardson's constant. Therefore, materials featuring a low W_f and high temperature withstanding materials are potential candidates for ETC.

The thermionic cooling mechanism (such as ETC) is expected to work well with passive thermal protection system (TMS) in enhancing overall heat load reduction. The base material used in the heat protection systems of the supersonic and hypersonic vehicles are ultrahigh temperature ceramics (UHTCs), which have a very high melting point (≥ 3000 °C), mechanical strength, thermal-shock and oxidation resistance. The borides, carbides, and nitrides of the early transition metals have melting points greater than 3000 °C, making them good candidates for extreme environment applications [145]. However, the 3000 °C melting point, although high, is not high enough to withstand long duration flight. To minimize the intense heat load of those UHTCs, a passive heat reduction/cooling mechanism must involve a composite bulk material and/or heterostructure of low W_f material and UHTCs, which are capable of enabling the full potential of ETC at low temperature. Most importantly, different simulation studies showed ETC system in the leading edge will have a locational advantage, as the leading edge is exposed to extremely high temperatures. Despite the availability of an ample number of simulation research studies pertaining to the implementation and effectiveness of ETC, there are no analogous experimental published results that specifically target the leading edges of hypersonic vehicles. In the future it will be interesting to see effectiveness ETC cooling of my synthesized bulk material and/or heterostructure of low W_f material and UHTCs.

6.3. UHS sintering of other UHTCs and low W_f materials

UHS, an excellent sintering process for UHTCs and other high temperature materials, was developed in this present study. However, only a few compositions were experimented in this research work. Different other single, multicomponent, and high entropy UHTCs and low W_f materials can be sintered by utilizing UHS technique as a continuation of present work.

6.4. Epitaxial and polycrystalline thin film by RF sputtering

In this research, limited composition of thin films of low W_f materials were synthesized by sputtering technique. A future work based on this part can be synthesizing different composition thin film of low W_f materials under different deposition parameter (different temperature, pressure, deposition rate, and gas mixture) by sputtering technique.

REFERENCES

[1] E. Wuchina, E. Opila, M. Opeka, B. Fahrenholtz and I. Talmy, 'UHTCs: Ultra-High Temperature Ceramic Materials for Extreme Environment Applications,' *The Electrochemical Society interface*, 16 [4] 30-36 (2007).

[2] W. G. Fahrenholtz, E. J. Wuchina, W. E. Lee and Y. Zhou, 'Ultra-High Temperature Ceramics : Materials for Extreme Environment Applications'. John Wiley & Sons, Inc 2014.

[3] T. J. Harrington, J. Gild, P. Sarker, C. Toher, C. M. Rost, O. F. Dippo, C. McElfresh, K. Kaufmann, E. Marin, L. Borowski, P. E. Hopkins, J. Luo, S. Curtarolo, D. W. Brenner and K. S. Vecchio, 'Phase stability and mechanical properties of novel high entropy transition metal carbides,' *Acta Materialia*, 166 [C] 271-280 (2019).

[4] A. B. Mei, B. M. Howe, C. Zhang, M. Sardela, J. N. Eckstein, L. Hultman, A. Rockett, I. Petrov and J. E. Greene, 'Physical properties of epitaxial ZrN/MgO(001) layers grown by reactive magnetron sputtering,' *Journal of vacuum science & technology. A, Vacuum, surfaces, and films*, 31 [6] 61516 (2013).

[5] W. G. Fahrenholtz, G. E. Hilmas, I. G. Talmy and J. A. Zaykoski, 'Refractory Diborides of Zirconium and Hafnium,' *J Am Ceram Soc*, 90 [5] 1347-1364 (2007).

[6] A. Paul, D. D. Jayaseelan, S. Venugopal, E. Zapata-Solvas, J. Binner, B. Vaidhyanathan, A. Heaton, P. Brown and W. E. Lee, 'UHTC composites for hypersonic applications,' *American Ceramic Society Bulletin*, 91 [1] 22-29 (2012).

[7] A. Kahn, 'Fermi level, work function and vacuum level,' *Materials horizons*, 3 [1] 7-1 (2016).

[8] S. Mondal, A. V. Rau, K. Lu, J. Li and D. Viehland, 'Multicomponent hexaborides with low work functions by ultra-fast high temperature sintering,' *Open ceramics*, 16 100479 (2023).

[9] D. M. Goebel, J. T. Crow and A. T. Forrester, 'Lanthanum hexaboride hollow cathode for dense plasma production,' *Rev. Sci. Instrum.; (United States)*, 49 [4] 469-472 (1978).

[10] C. Fu, J. Xu, Y. Chang, Q. Wang, Y. Wang, B. Yu, P. Guo, J. Xu, H. Sun, Y. Luo and J. Liu, 'Flexible three-dimensional CeB6 nanowire arrays and excellent field emission emitters,' *J. Alloys Compd.*, 729 997-1003 (2017).

[11] S. Morgen and R. Reifenberger, 'Thermionic and threshold photoemission energy distributions from LaB6(110),' *Surf. Sci.*, 186 [1-2] 232-246 (1987).

[12] E. Sani, L. Mercatelli, M. Meucci, L. Zoli and D. Sciti, 'Lanthanum hexaboride for solar energy applications,' *Sci. Rep.*, 7 [1] 718 (2017).

[13] X. Zhang, P. Hu, J. Han, L. Xu and S. Meng, 'The addition of lanthanum hexaboride to zirconium diboride for improved oxidation resistance,' *Scr. Mater.*, 57 [11] 1036-1039 (2007).

[14] E. Eakins, D. Jayaseelan and W. Lee, 'Toward Oxidation-Resistant ZrB2-SiC Ultra High Temperature Ceramics,' *Metall Mater Trans A*, 42 [4] 878-887 (2011).

[15] S. S. Ordanyan, O. V. Yurchenko and S. V. Vikhman, 'Phase Relations in the SiC-LaB6 System,' *Inorg. Mater.*, 40 [6] 600-603 (2004).

[16] J. K. Sonber, K. Sairam, Murthy, T. S. R. Ch, A. Nagaraj, C. Subramanian and R. C. Hubli, 'Synthesis, densification and oxidation study of lanthanum hexaboride,' *J. Eur. Ceram. Soc.*, 34 [5] 1155-1160 (2014).

[17] M. M. Hasan, E. Kisi and H. Sugo, 'Single-step low-temperature synthesis routes for (Ba, Ce, Gd) hexaborides and their thermionic emission properties,' *J. Alloys Compd.*, 916 165474 (2022).

[18] V. S. Fomenko, 'Handbook of Thermionic Properties'. Springer, Boston, MA, 1966.

[19] L. W. Swanson and D. R. McNeely, 'Work functions of the (001) face of the hexaborides of Ba, La, Ce and Sm,' *Surf Sci.*, 83 [1] 11-28 (1979).

[20] C. P. Wang, Y. Shi, D. Wang, Y. Lu, D. L. Zhao and X. J. Liu, 'Thermodynamic assessment of the B–Ce and B–Pr systems,' *Calphad*, 41 150-155 (2013).

[21] D. R. Lide, 'CRC Handbook of Chemistry and Physics, 82nd Edition'. CRC Press, Boca Raton, FL., 2001.

[22] S. Otani and Y. Ishizawa, 'Thermionic emission properties of boron-rich LaB6 and CeB6 crystal cathodes,' *J. Alloys Compd.*, 245 [1-2] L18-L20 (1996).

[23] T. Ma, R. Jacobs, J. Booske and D. Morgan, 'Work Function Trends and New Low-Work-Function Boride and Nitride Materials for Electron Emission Applications,' *J. Phys. Chem. C* ., 125 [31] 17400-17410 (2021).

[24] J. Wang, C. Zhu, F. Meng, G. Liu, Y. Gu, H. Wang, S. Gao and K. Wang, 'Work functions of metal hexaborides: Density functional study,' *Mod Phys Lett B*, 32 [2] 1850007 (2018).

[25] M. Yoshitake, 'Work function and band alignment of electrode materials : the art of interface potential for electronic devices, solar cells, and batteries'. Springer, Tokyo, 2021.

[26] K. L. Jensen, 'Introduction to the physics of electron emission'. John Wiley & Sons, Inc, Hoboken, NJ, 2018.

[27] J. Etourneau, J. P. Mercurio and P. Hagenmuller, 'Compounds Based on Octahedral B6 Units: Hexaborides and Tetraborides'; pp. 115-138 in Boron and Refractory Borides. Springer Berlin Heidelberg, Berlin, Heidelberg,.

[28] J. T. Cahill and O. A. Graeve, 'Hexaborides: a review of structure, synthesis and processing,' *J. Mater. Res. Technol.J. Mater. Res. Technol.*, 8 [6] 6321-6335 (2019).

[29] M. M. Hasan, D. Cuskelly, H. Sugo and E. H. Kisi, 'Low temperature synthesis of low thermionic work function (LaxBa1−x)B6,' *J. Alloys Compd.*, 636 67-72 (2015).

[30] S. L. Zhou, J. X. Zhang, L. H. Bao, X. G. Yu, Q. L. Hu and D. Q. Hu, 'Enhanced thermionic emission properties in textured two-phase LaB6–BaB6 system prepared by spark plasma sintering,' *J. Alloys Compd.*, 611 130-134 (2014).

[31] C. Tantardini and A. R. Oganov, 'Thermochemical electronegativities of the elements,' *Nat. Commun.*, 12 [1] 2087 (2021).

[32] M. N. Rahaman, 'Ceramic processing and sintering'. Marcel Dekker 2003.

[33] R. M. German, 'Powder metallurgy and particulate materials processing'. Metal Powder Industries Fed, Princeton, NJ, 2005.

[34] I. -. Chen and X. -. Wang, 'Sintering dense nanocrystalline ceramics without final-stage grain growth,' *Nature*, 404 168 (2000).

[35] J. M. Lonergan, W. G. Fahrenholtz and G. E. Hilmas, 'Sintering Mechanisms and Kinetics for Reaction Hot-Pressed ZrB 2,' *Journal of the American Ceramic Society*, 98 [8] 2344-2351 (2015).

[36] M. Chu, M. N. Rahaman, L. C. De Jonghe and R. J. Brook, 'Effect of Heating Rate on Sintering and Coarsening,' *J Am Ceram Soc*, 74 [6] 1217-1225 (1991).

[37] G. Xu, I. K. Lloyd, Y. Carmel, T. Olorunyolemi and O. C. Wilson, 'Microwave sintering of ZnO at ultra high heating rates,' *Journal of materials research*, 16 [10] 2850-2858 (2001).

[38] R. L. Coble, 'Sintering Crystalline Solids. II. Experimental Test of Diffusion Models in Powder Compacts,' *Journal of applied physics*, 32 [5] 793-799 (1961).

[39] C. GRESKOVICH and K. W. LAY, 'Grain Growth in Very Porous Al2O3 Compacts,' *Journal of the American Ceramic Society*, 55 [3] 142-146 (1972).

[40] D. E. García, J. Seidel, R. Janssen and N. Claussen, 'Fast firing of alumina,' *Journal of the European Ceramic Society*, 15 [10] 935-938 (1995).

[41] E. W. Neuman, M. J. Thompson, W. G. Fahrenholtz and G. E. Hilmas, 'Heating rate effects on the thermal and mechanical properties of ZrB2,' *Journal of the American Ceramic Society*, 105 [1] 169-180 (2022).

[42] M. Thompson, W. G. Fahrenholtz and G. Hilmas, 'Effect of Starting Particle Size and Oxygen Content on Densification of ZrB2,' *Journal of the American Ceramic Society*, 94 [2] 429-435 (2011).

[43] D. KALISH and E. V. CLOUGHERTY, 'Densification Mechanisms in High-pressure Hot-Pressing of HfB2,' *J Am Ceram Soc*, 52 [1] 26-30 (1969).

[44] E. W. Neuman, G. E. Hilmas and W. G. Fahrenholtz, 'Strength of Zirconium Diboride to 2300°C,' *Journal of the American Ceramic Society*, 96 [1] 47-50 (2013).

[45] S. Mondal, A. Durygin, V. Drozd, J. Belisario and Z. Cheng, 'Multicomponent bulk metal nitride (Nb1/3Ta1/3Ti1/3)N1−δ synthesis via reaction flash sintering and characterizations,' *Journal of the American Ceramic Society*, 103 [9] 4876-4893 (2020).

[46] S. Sun, G. Zhang, W. Wu, J. Liu, T. Suzuki and Y. Sakka, 'Reactive spark plasma sintering of ZrC and HfC ceramics with fine microstructures,' *Scripta materialia*, 69 [2] 139-142 (2013).

[47] J. Gild, K. Kaufmann, K. Vecchio and J. Luo, 'Reactive flash spark plasma sintering of high-entropy ultrahigh temperature ceramics,' *Scripta materialia*, 170 106-110 (2019).

[48] J. Zou, G. Zhang, Z. Shen and J. Binner, 'Ultra-low temperature reactive spark plasma sintering of ZrB2-hBN ceramics,' *Journal of the European Ceramic Society*, 36 [15] 3637-3645 (2016).

[49] J. Belisario, S. Mondal, I. Khakpour, A. Franco Hernandez, A. Durygin and Z. Cheng, 'Synthesis and flash sintering of (Hf1-xZrx)B2 solid solution powders,' *Journal of the European Ceramic Society*, 41 [4] 2215-2225 (2021).

[50] M. Biesuz and V. M. Sglavo, 'Flash sintering of ceramics,' *Journal of the European Ceramic Society*, 39 [2-3] 115-143 (2019).

[51] A. L. Chamberlain, W. G. Fahrenholtz and G. E. Hilmas, 'Pressureless Sintering of Zirconium Diboride,' *J Am Ceram Soc*, 89 [2] 450-456 (2006).

[52] R. M. d. Rocha, F. F. Sene, M. d. O. Juliani and C. O. Davi, 'Effect of ZrB2 Particle Size on Pressureless Sintering of ZrB2 - ß-Sic Composites,' *Journal of aerospace technology and management*, 11 [1] 2819 (2019).

[53] S. Leo and C. Tallon, 'Pressureless Sintering of ZrB2 Prepared by Colloidal Processing: Particle Packing, Sintering Conditions, and Additives,' *Journal of the American Ceramic Society*, 99 [12] 3883-3892 (2016).

[54] V. Zamora, A. L. Ortiz, F. Guiberteau and M. Nygren, 'Spark-plasma sintering of ZrB2 ultra-high-temperature ceramics at lower temperature via nanoscale crystal refinement,' *Journal of the European Ceramic Society*, 32 [10] 2529-2536 (2012).

[55] V. Zamora, A. L. Ortiz, F. Guiberteau and M. Nygren, 'Crystal-size dependence of the spark-plasma-sintering kinetics of ZrB2 ultra-high-temperature ceramics,' *Journal of the European Ceramic Society*, 32 [2] 271-276 (2012).

[56] M. Shahedi Asl, Y. Azizian-Kalandaragh, Z. Ahmadi, A. Sabahi Namini and A. Motallebzadeh, 'Spark plasma sintering of ZrB2-based composites co-reinforced with SiC whiskers and pulverized carbon fibers,' *International journal of refractory metals & hard materials*, 83 104989 (2019).

[57] A. L. Chamberlain, W. G. Fahrenholtz, G. E. Hilmas and D. T. Ellerby, 'High-Strength Zirconium Diboride-Based Ceramics,' *J Am Ceram Soc*, 87 [6] 1170-1172 (2004).

[58] E. W. Neuman, G. E. Hilmas and W. G. Fahrenholtz, 'Processing, microstructure, and mechanical properties of large-grained zirconium diboride ceramics,' *Materials science & engineering. A, Structural materials : properties, microstructure and processing*, 670 196-204 (2016).

[59] K. Amalajyothi and L. J. Berchmans, 'Combustion synthesis of nanocrystalline cerium hexaboride using citric acid as a fuel,' *Int. J Self-Propag. High-Temp. Synth*, 18 [3] 151-153 (2009).

[60] Z. Dou, T. Zhang, Z. Zhang, H. Zhang and J. He, 'Preparation and characterization of LaB6 ultra fine powder by combustion synthesis,' *Trans. Nonferrous Met. Soc.*, 21 [8] 1790-1794 (2011).

[61] Z. H. Dou, J. C. He and T. A. Zhang, 'Preparation and Characterization of Cerium Hexaboride Nanometer Powders by Combustion Synthesis,' *Adv Mat Res*, 236-238 1670-1674 (2011).

[62] C. Y. Zou, Y. M. Zhao and J. Q. Xu, 'Synthesis of single-crystalline CeB6 nanowires,' *J. Cryst. Growth*, 291 [1] 112-116 (2006).

[63] T. Tanaka, R. Nishitani, C. Oshima, E. Bannai and S. Kawai, 'The Preparation and Properties of CeB6, SmB6 and GdB6,' *J. Appl. Phys.*, 51 [7] 3877-3883 (1980).

[64] G. H. Olsen and A. V. Cafiero, 'Single-crystal growth of mixed (La, Eu, Y, Ce, Ba, Cs) hexaborides for thermionic emission,' *J. Cryst. Growth*, 44 [3] 287-290 (1978).

[65] R. K. Selvan, I. Genish, I. Perelshtein, J. M. Calderon Moreno and A. Gedanken, 'Single Step, Low-Temperature Synthesis of Submicron-Sized Rare Earth Hexaborides,' *J. Phys. Chem. C* ., 112 [6] 1795-1802 (2008).

[66] Menaka, R. Patra, S. Ghosh and A. K. Ganguli, 'Novel borothermal route for the synthesis of lanthanum cerium hexaborides and their field emission properties,' *J. Solid State Chem.*, 194 173-178 (2012).

[67] C. Wang, W. Ping, Q. Bai, H. Cui, R. Hensleigh, R. Wang, A. H. Brozena, Z. Xu, J. Dai, Y. Pei, C. Zheng, G. Pastel, J. Gao, X. Wang, H. Wang, J. Zhao, B. Yang, X. R. Zheng, J. Luo, Y. Mo, B. Dunn and L. Hu, 'A general method to synthesize and sinter bulk ceramics in seconds,' *Science*, 368 [6490] 521-526 (2020).

[68] M. Kermani, D. Zhu, J. Li, J. Wu, Y. Lin, Z. Dai, C. Hu and S. Grasso, 'Ultra-fast High-temperature Sintering (UHS) of translucent alumina,' *Open Ceramics*, 9 100202 (2022).

[69] M. Kermani, J. Dong, M. Biesuz, Y. Linx, H. Deng, V. M. Sglavo, M. J. Reece, C. Hu and S. Grasso, 'Ultrafast high-temperature sintering (UHS) of fine grained α-Al2O3,' *J. Eur. Ceram. Soc.*, 41 [13] 6626-6633 (2021).

[70] J. Dong, V. Pouchly, M. Biesuz, V. Tyrpekl, M. Vilémová, M. Kermani, M. Reece, C. Hu and S. Grasso, 'Thermally-insulated ultra-fast high temperature sintering (UHS) of zirconia: A master sintering curve analysis,' *Scr. Mater.*, 203 114076 (2021).

[71] M. J. Reavley, H. Guo, J. Yuan, A. Y. R. Ng, T. Y. K. Ho, H. T. Tan, Z. Du and C. L. Gan, 'Ultrafast high-temperature sintering of barium titanate ceramics with colossal dielectric constants,' *J. Eur. Ceram. Soc.*, 42 [12] 4934 (2022).

[72] H. Mao, E. Dong, S. Jin, X. Qiu and P. Shen, 'Ultrafast high-temperature synthesis and densification of high-entropy carbides,' *J. Eur. Ceram. Soc.*, 42 [10] 4053-4065 (2022).

[73] T. P. Mishra, S. Wang, C. Lenser, D. Jennings, M. Kindelmann, W. Rheinheimer, C. Broeckmann, M. Bram and O. Guillon, 'Ultra-fast high-temperature sintering of strontium titanate,' *Acta Mater.*, 231 (2022).

[74] R. Luo, M. Kermani, Z. Guo, J. Dong, C. Hu, F. Zuo, S. Grasso, B. Jiang, G. Nie, Z. Yan, Q. Wang, Y. Gan, F. He and H. Lin, 'Ultrafast high-temperature sintering of silicon nitride: A comparison with the state-of-the-art techniques,' *J. Eur. Ceram. Soc.*, 41 [13] 6338-6345 (2021).

[75] C. Wang, W. Zhong, W. Ping, Z. Lin, R. Wang, J. Dai, M. Guo, W. Xiong, J. Zhao and L. Hu, 'Rapid Synthesis and Sintering of Metals from Powders,' *Adv. Sci.*, 8 [12] 2004229-n/a (2021).

[76] V. CRACIUN and D. CRACIUN, 'Pulsed laser deposition of crystalline LaB6 thin films,' *Applied surface science*, 247 [1-4] 384-389 (Jul 15, 2005).10.1016/j.apsusc.2005.01.071.

[77] D. J. Late, M. A. More, D. S. Joag, P. Misra, B. N. Singh and L. M. Kukreja, 'Field emission studies on well adhered pulsed laser deposited LaB6 on W tip,' *Applied physics letters*, 89 [12] (2006).

[78] A. Mezzi, P. Soltani, S. Kaciulis, A. Bellucci, M. Girolami, M. Mastellone and D. M. Trucchi, 'Investigation of work function and chemical composition of thin films of borides and nitrides,' *Surface and interface analysis*, 50 [11] 1138-1144 (2018).

[79] W. Waldhauser, C. Mitterer, J. Laimer and H. Störi, 'Sputtered thermionic hexaboride coatings,' *Surface & coatings technology*, 98 [1] 1315-1323 (1998).

[80] A. Bellucci, M. Mastellone, M. Girolami, V. Serpente, A. Generosi, B. Paci, A. Mezzi, S. Kaciulis, R. Carducci, R. Polini, S. Orlando, A. Santagata, A. De Bonis, M. Meucci, L. Mercatelli, E. Sani and D. M. Trucchi, 'Nanocrystalline lanthanum boride thin films by femtosecond pulsed laser deposition as efficient emitters in hybrid thermionic-photovoltaic energy converters,' *Applied surface science*, 513 145829 (2020).

[81] A. YUTANI, A. KOBAYASHI and A. KINBARA, 'Work functions of thin LaB6 films,' *Applied surface science*, 70-71 [1-4] 737-741 (Jun 2, 1993).10.1016/0169-4332(93)90612-F.

[82] Thomas Sabu and Thankappan Aparna, 'Low-Dimensional Perovskites'; pp. 1 in Perovskite Photovoltaics - Basic to Advanced Concepts and Implementation. Elsevier 2018.

[83] S. Royer, D. Duprez, F. Can, X. Courtois, C. Batiot-Dupeyrat, S. Laassiri and H. Alamdari, 'Perovskites as Substitutes of Noble Metals for Heterogeneous Catalysis: Dream or Reality,' *Chemical reviews*, 114 [20] 10292-10368 (2014).

[84] M. Sousa, C. Rossel, C. Marchiori, H. Siegwart, D. Caimi, J. -. Locquet, D. J. Webb, R. Germann, J. Fompeyrine, K. Babich, J. W. Seo and C. Dieker, 'Optical properties of epitaxial SrHfO3 thin films grown on Si,' *Journal of applied physics*, 102 [10] 104103 (2007).

[85] D. McDaniel Martin, Hu Chengqing, Lu Sirong, Q. Ngo Thong, Posadas Agham, Jiang Aiting, J. Smith David, T. Yu Edward, A. Demkov Alexander and G. Ekerdt John, 'Atomic layer deposition of crystalline SrHfO3 directly on Ge (001) for high-k dielectric applications,' *Journal of applied physics*, 117 [5] (2015).

[86] K. Black, M. Werner, R. Rowlands–Jones, P. R. Chalker and M. J. Rosseinsky, 'SrHfO3 Films Grown on Si(100) by Plasma-Assisted Atomic Layer Deposition,' *Chemistry of materials*, 23 [10] 2518-2520 (2011).

[87] R. E. Cohen, 'Origin of ferroelectricity in perovskite oxides,' *Nature (London)*, 358 [6382] 136-138 (1992).

[88] H. Park, C. Ha and J. Lee, 'Advances in piezoelectric halide perovskites for energy harvesting applications,' *Journal of materials chemistry. A, Materials for energy and sustainability*, 8 [46] 24353-24367 (2020).

[89] F. Liu, S. Sidhik, M. A. Hoffbauer, S. Lewis, A. J. Neukirch, V. Pavlenko, H. Tsai, W. Nie, J. Even, S. Tretiak, P. M. Ajayan, M. G. Kanatzidis, J. J. Crochet, N. A. Moody, J. Blancon and A. D. Mohite, 'Highly efficient photoelectric effect in halide perovskites for regenerative electron sources,' *Nature communications*, 12 [1] 673 (2021).

[90] Wei Yingfen, Gui Hong, Zhao Zhenjie, Li Junrui, Liu Yong, Xin Shengwei, Li Xiaohong and Xie Wenhui, 'Structure and magnetic properties of the perovskite YCo0.5Fe0.5O3,' *AIP Advances*, 4 [12] 127134-9 (2014).

[91] A. Chilvery, S. Das, P. Guggilla, C. Brantley and A. Sunda-Meya, 'A perspective on the recent progress in solution-processed methods for highly efficient perovskite solar cells,' *Science and Technology of Advanced Materials*, 17 [1] 650-658 (2016).

[92] C. Rossel, B. Mereu, C. Marchiori, D. Caimi, M. Sousa, A. Guiller, H. Siegwart, R. Germann, J. -. Locquet, J. Fompeyrine, D. J. Webb, C. Dieker and J. W. Seo, 'Field-effect transistors with SrHfO3 as gate oxide,' *Applied physics letters*, 89 [5] 53506 (2006).

[93] V. Hien-Hoang, T. M. Nhung-Nguyen and H. Kim, 'Synthesis and electrical transport of SrHfO3 thin films grown on a SrTiO3 (001) substrate using a pulsed laser deposition,' *Current applied physics*, 20 [9] 1031-1035 (2020).

[94] G. Lupina, G. Kozłowski, J. Dabrowski, P. Dudek, G. Lippert and H. -. Müssig, 'Dielectric and structural properties of thin SrHfO3 layers on TiN,' *Applied physics letters*, 93 [25] 252907 (2008).

[95] C. ROSSEL, M. SOUSA, R. GERMANN, A. TAPPONNIER, K. BABICH, C. MARCHIORI, J. FOMPEYRINE, D. WEBB, D. CAIMI, B. MEREU, A. ISPAS, J. P. LOCQUET and H. SIEGWART, 'SrHfO3 as gate dielectric for future CMOS technology,' *Microelectronic engineering*, 84 [9-10] 1869-1873 (2007).10.1016/j.mee.2007.04.029.

[96] S. Yamanaka, T. Maekawa, H. Muta, T. Matsuda, S. Kobayashi and K. Kurosaki, 'Thermophysical properties of SrHfO3 and SrRuO3,' *Journal of solid state chemistry*, 177 [10] 3484-3489 (2004).

[97] S. Cuffini, J. Guevara, Y. Mascarenhas, P. de la Presa, A. Ayala and A. Lopez Garcia, 'HIGH TEMPERATURE STUDIES OF PEROVSKITE OXIDES: X-RAY DIFFRACTION AND PAC SPECTROSCOPY,' *Ceramica (Sao Paulo). Vol. 43, no. 280, pp. 91-94. 1997*, 43 [280] 91-94 (1997).

[98] B. J. Kennedy, C. J. Howard and B. C. Chakoumakos, 'High-Temperature Phase Transititons in SrHfO3,' *Physical review. B, Condensed matter*, 60 [5] (1999).

[99] M. K. Singh, G. Singh, T. H. Kim, S. Kojima, R. S. Katiyar and J. F. Scott, 'High-temperature phase transitions in SrHfO3: A Raman scattering study,' *EPL*, 107 [2] (2014).

[100] R. Ma, M. Liu, J. Wang and H. Wang, 'The room temperature deposition of high-quality epitaxial yttrium iron garnet thin film via RF sputtering,' *Journal of alloys and compounds*, 708 213-219 (2017).

[101] Q. Abbas, H. Liang, J. Shi, Y. Chen, X. Xia, A. u. Ahmad, J. Liu and G. Du, 'Growth and characterization of amorphous boron nitride dielectric films on Si via RF sputtering at room temperature,' *Materials letters*, 227 284-288 (2018).

[102] A. K. Saikumar, S. D. Nehate and K. B. Sundaram, 'Review-RF Sputtered Films of Ga2O3,' *ECS journal of solid state science and technology*, 8 [7] Q3064-Q3078 (2019).

[103] M. Biesuz, J. Dong, S. Fu, Y. Liu, H. Zhang, D. Zhu, C. Hu and S. Grasso, 'Thermally-insulated flash sintering,' *Scr. Mater.*, 162 99-102 (2019).

[104] R. Guo, H. Mao, Z. Zhao and P. Shen, 'Ultrafast high-temperature sintering of bulk oxides,' *Scripta materialia*, 193 103-107 (2021).

[105] Hidetoshi Kotera, edited by Kiyotaka Wasa and Isaku Kanno, 'Handbook of sputter deposition technology : fundamentals and applications for functional thin films, nano-materials, and MEMS'. William Andrew, Waltham [MA], 2012.

[106] M. Ohring, 'Materials Science of Thin Films - Deposition and Structure (2nd Edition)'. Elsevier 2002.

[107] S. C. Zhang, G. E. Hilmas and W. G. Fahrenholtz, 'Pressureless Sintering of ZrB2-SiC Ceramics,' *Journal of the American Ceramic Society*, 91 [1] 26-32 (2008).

[108] J. C. Rivière, 'The work function of gold,' *Appl. Phys. Lett.*, 8 [7] 172 (1966).

[109] V. Panchal, R. Pearce, R. Yakimova, A. Tzalenchuk and O. Kazakova, 'Standardization of surface potential measurements of graphene domains,' *Sci. Rep.*, 3 [1] 2597 (2013).

[110] W. C. Oliver and G. M. Pharr, 'An improved technique for determining hardness and elastic modulus using load and displacement sensing indentation experiments,' *Journal of materials research*, 7 [6] 1564-1583 (1992).

[111] Y. Zhang, J. Nie, J. M. Chan and J. Luo, 'Probing the densification mechanisms during flash sintering of ZnO,' *Acta Materialia*, 125 465-475 (2017).

[112] W. Ji, B. Parker, S. Falco, J. Y. Zhang, Z. Y. Fu and R. I. Todd, 'Ultra-fast firing: Effect of heating rate on sintering of 3YSZ, with and without an electric field,' *Journal of the European Ceramic Society*, 37 [6] 2547-2551 (2017).

[113] A. Sharafi, C. G. Haslam, R. D. Kerns, J. Wolfenstine and J. Sakamoto, 'Controlling and correlating the effect of grain size with the mechanical and electrochemical properties of Li 7 La 3 Zr 2 O 12 solid-state electrolyte,' *Journal of Materials Chemistry A*, 5 [40] 21491-21504 (2017).

[114] D. Pham, J. H. Dycus, J. M. LeBeau, V. R. Manga, K. Muralidharan and E. L. Corral, 'Thermochemical model on the carbothermal reduction of oxides during spark plasma sintering of zirconium diboride,' *Journal of the American Ceramic Society*, 102 [2] 757-767 (2019).

[115] M. Shahedi Asl, B. Nayebi, A. Motallebzadeh and M. Shokouhimehr, 'Nanoindentation and nanostructural characterization of ZrB2–SiC composite doped with graphite nano-flakes,' *Composites. Part B, Engineering*, 175 107153 (2019).

[116] T. Csanádi, A. Naughton-Duszová and J. Dusza, 'Anisotropic slip activation via homogeneous dislocation nucleation in ZrB2 ceramic grains during nanoindentation,' *Scripta materialia*, 152 89-93 (2018).

[117] S. Guicciardi, C. Melandri and F. T. Monteverde, 'Characterization of pop-in phenomena and indentation modulus in a polycrystalline ZrB2 ceramic,' *Journal of the European Ceramic Society*, 30 [4] 1027-1034 (2010).

[118] N. P. Bansal, 'Handbook of Ceramic Composites'. Kluwer Academic Publishers 2005.

[119] S. Chakraborty, A. R. Mallick, D. Debnath and P. K. Das, 'Densification, mechanical and tribological properties of ZrB2 by SPS: Effect of pulsed current,' *International journal of refractory metals & hard materials*, 48 150-156 (2015).

[120] F. Nakamori, Y. Ohishi, H. Muta, K. Kurosaki, K. Fukumoto and S. Yamanaka, 'Mechanical and thermal properties of bulk ZrB2,' *Journal of nuclear materials*, 467 612-617 (2015).

[121] E. Zapata-Solvas, D. D. Jayaseelan, H. T. Lin, P. Brown and W. E. Lee, 'Mechanical properties of ZrB2- and HfB2-based ultra-high temperature ceramics fabricated by spark plasma sintering,' *Journal of the European Ceramic Society*, 33 [7] 1373-1386 (2013).

[122] R. Riedel, 'Handbook of ceramic hard materials'. Wiley-VCH, Weinheim [u.a.],.

[123] J. J. Meléndez-Martínez, A. Domínguez-Rodríguez, F. Monteverde, C. Melandri and G. de Portu, 'Characterisation and high temperature mechanical properties of zirconium boride-based materials,' *Journal of the European Ceramic Society*, 22 [14] 2543-2549 (2002).

[124] B. Nayebi, N. Parvin, M. Shahedi Asl, A. Motallebzadeh and M. Shokouhimehr, 'Nanostructural and nanoindentation characterization of ZrB2 ceramics toughened with in-situ synthesized ZrC,' *International journal of refractory metals & hard materials*, 94 1 (2021).

[125] S. Vorotilo, K. Sidnov, V. V. Kurbatkina, P. A. Loginov, E. I. Patsera, T. A. Sviridova, T. A. Lobova, E. A. Levashov and V. V. Klechkovskaya, 'Super-hardening and localized plastic deformation behaviors in ZrB2 –TaB2 ceramics,' *Journal of alloys and compounds*, 901 163368 (2022).

[126] K. S. and S. Bakshi, 'Reactive Spark Plasma Sintering and Mechanical Properties of Zirconium Diboride–Titanium Diboride Ultrahigh Temperature Ceramic Solid Solutions,' *Technologies*, 4 [3] 30 (2016).

[127] E. J. Cheng, Y. Li, J. Sakamoto, S. Han, H. Sun, J. Noble, H. Katsui and T. Goto, 'Mechanical properties of individual phases of ZrB2-ZrC eutectic composite measured by nanoindentation,' *Journal of the European Ceramic Society*, 37 [13] 4223-4227 (2017).

[128] M. J. Gasch, D. T. Ellerby and S. M. Johnson, 'Ultra High Temperature Ceramic Composites'; pp. 197-224 in Handbook of Ceramic Composites. Edited by N. P. Bansal (Ed.). Springer US, Boston, MA, 2005.

[129] J. Gild, Y. Zhang, T. Harrington, S. Jiang, T. Hu, M. C. Quinn, W. M. Mellor, N. Zhou, K. Vecchio and J. Luo, 'High-Entropy Metal Diborides: A New Class of High-Entropy Materials and a New Type of Ultrahigh Temperature Ceramics,' *Scientific reports*, 6 [1] 37946 (2016).

[130] 'Oxidation of ZrB2-Based Ceramics in Dry Air,'.

[131] R. Inoue, Y. Arai, Y. Kubota, Y. Kogo and K. Goto, 'Oxidation of ZrB2 and its composites: a review,' *J Mater Sci*, 53 [21] 14885-14906 (2018).

[132] W. Melitz, J. Shen, A. C. Kummel and S. Lee, 'Kelvin probe force microscopy and its application,' *Surf. Sci. Rep.*, 66 [1] 1-27 (2011).

[133] M. Trenary, 'Surface science studies of metal hexaborides,' *Sci Technol Adv Mater*, 13 [2] 023002 (2012).

[134] L. Vegard, 'The constitution of mixed crystal and the space occupied by atom,' *Z.Phys*, 5 17 (1921).

[135] X. ZHONG, Y. FENG, W. KNOLL and M. HAN, 'Alloyed ZnxCd1-xS Nanocrystals with Highly Narrow Luminescence Spectral Width,' *J. Am. Chem. Soc.*, 125 [44] 13559-13563 (2003).

[136] J. K. Furdyna, 'Diluted magnetic semiconductors,' *J. Appl. Phys.*, 64 [4] R29-R64 (1988).

[137] G. Min, S. Zheng, Z. Zou, H. Yu and J. Han, 'Reaction synthesis and formation mechanism of barium hexaboride,' *Mater. Lett.*, 57 [7] 1330-1333 (2003).

[138] G. V. Samsonov, Y. B. Paderno and V. S. Fomenko, 'Hexaborides of the rare-earth metals,' *Powder Metall Met Ceram*, 2 [6] 449-454 (1964).

[139] M. GESLEY and L. W. SWANSON, 'A determination of the low work function planes of LaB6,' *Surf. Sci.*, 146 [2/3] 583-599 (1984).

[140] J. Voss, A. Vojvodic, S. H. Chou, R. T. Howe and F. Abild-Pedersen, 'Inherent Enhancement of Electronic Emission from Hexaboride Heterostructure,' *Phys. Rev. Appl.*, 2 [2] (2014).

[141] M. T. Greiner, L. Chai, M. G. Helander, W. Tang and Z. Lu, 'Transition Metal Oxide Work Functions: The Influence of Cation Oxidation State and Oxygen Vacancies,' *Adv. Funct. Mater.*, 22 [21] 4557-4568 (2012).

[142] M. Acharya, E. Banyas, M. Ramesh, Y. Jiang, A. Fernandez, A. Dasgupta, H. Ling, B. Hanrahan, K. Persson, J. B. Neaton and L. W. Martin, 'Exploring the Pb1−xSrxHfO3 System and Potential for High Capacitive Energy Storage Density and Efficiency,' *Advanced materials (Weinheim)*, 34 [1] n/a (2022).

[143] P. Rai-Choudhury and D. K. Schroder, 'SELECTIVE SILICON EPITAXY AND ORIENTATION DEPENDENCE OF GROWTH,' *Journal of the Electrochemical Society*, 120 [5] 664 (1973).

[144] O. W. 1. Richardson, 'The emission of electricity from hot bodies'. Longmans, Green and co., 1921, No place, unknown, or undetermined, 1921.

[145] W. G. Fahrenholtz and G. E. Hilmas, 'Ultra-high temperature ceramics: Materials for extreme environments,' *Scripta Materialia*, 129 94-99 (2017).